To the Graduate Council:

I am submitting herewith a thesis written by Perry A. Gray entitled "Experimental Study of Convective Breakdown during Solidification of a Metal Model Material." I have examined the final copy for form and content and recommend that it be accepted in partial fulfillment of the requirements for the degree of Master of Science, with a major in Engineering Science and Mechanics.

Mary Helen McCay

Mary Helen McCay, Major Professor

We have read this Thesis
and recommend its acceptance:

Dwayne McCay

Roger A. Crawford

Accepted for the Council:

Vice Provost
and Dean of the Graduate School

STATEMENT OF PERMISSION TO USE

In presenting this thesis in partial fulfillment of the reguirements for a Master's degree at the University of Tennessee, Knoxville, I agree that the Library shall make it available to borrowers under rules of the Library. Brief quotations from this thesis are allowable without special permission, provided that accurate acknowledgment of the source is made.

Permission for extensive quotation from or reproduction of this thesis may be granted by my major professor, or in her absence, by the Head of Interlibrary Services when, in the opinion of either, the proposed use of the material is for scholarly purposes. Any copying or use of the material in this thesis for financial gain shall not be allowed without my written permission.

Signature Perry A. Gray

Date 12/15/88

EXPERIMENTAL STUDY OF CONVECTIVE BREAKDOWN DURING SOLIDIFICATION OF A METAL MODEL MATERIAL

A Thesis

Presented for the

Master of Science

Degree

The University of Tennessee, Knoxville

PERRY A. GRAY

May 1989

ABSTRACT

The research reported here examined the convective instabilities that lead to structural and compositional nonuniformities in finished metal castings by the use of the metal model material ammonium chloride - water. The density distribution in front of the semi-solid (mushy-zone) region in the solidifying system was studied using a confocal optical imaging system and the convective breakdown was studied using a particle side scattering technique. It was shown that the convective breakdown is a classic Rayleigh - Benard instability resulting from a density inversion in front of the mushy - zone. The convection was found to be of the three dimensional Benard cell type.

TABLE OF CONTENTS

SECTION	PAGE
I. INTRODUCTION	1
II. BACKGROUND	3
Casting	3
Metal Models	10
The NH_4Cl-H_2O Eutectic	11
Eutectics	11
Properties of NH_4Cl-H_2O	15
Diffusion coefficient	15
Index of refraction	15
Density	15
General properties of NH_4Cl	15
NH_4Cl structure	23
Optical Techniques	23
Visualization of density changes	23
Flow visualization	27
Fluid Instabilities During Solidification	29
Thermal instabilities	29
Solutal instabilities	30
Double diffusive instabilities	31
III. APPARATUS	33
Control System and Related Hardware	33
Optical System	38
IV. EXPERIMENTAL PROCEDURES	44

V. DATA REDUCTION 48
VI. RESULTS AND DISCUSSION 52
Cooling Rate Effects 52
Temperature Gradient Effects 80
Null Layer Behavior 80
Vortex Geometry and Relation to the Null Layer 84
VII. SUMMARY AND CONCLUSIONS 87
BIBLIOGRAPHY 91
VITA 93

LIST OF FIGURES

FIGURE		PAGE
II-1.	Typical ingot casting	4
II-2.	Typical two phase region in a binary system	6
II-3.	Typical solute diffusion profile during plane front solidification	7
II-4.	Schematic of directional solidification process	8
II-5.	Final solid composition distribution after solidification	9
II-6.	Typical eutectic phase diagram	12
II-7.	Ammonium chloride - water phase diagram	14
II-8.	Diffusion coefficient of NH_4Cl - H_2O as a function of composition	16
II-9.	Index of refraction of NH_4Cl - 72.93 wt% H_2O as a function of temperature (from reference 8)	17
II-10.	Index of refraction of NH_4Cl - H_2O at 22°C as a function of composition (from reference 8)	18
II-11.	Density of NH_4Cl - H_2O as a function of composition for selected temperatures	19
II-12.	Density of NH_4Cl - H_2O as a function of temperature for selected compositions	20
II-13.	NH_4Cl crystal structure	24
II-14.	Confocal optical imaging system	26
II-15.	Particle side scattering system	28
III-1.	Control system parts list	34
III-2.	Control system	35
III-3.	Scale drawing of cuvette assembly	36
III-4.	Schematic of cuvette solidification assembly	37

III-5. Schematic of optical system 39

III-6. Optical system parts list 40

IV-1. Scale drawing of cuvette (all dimensions in mm). 45

V-1. Sample photograph of confocal optical system data 49

V-2. Sample photograph of particle tracker data 50

VI-1. Photograph sequence of confocal system data for 1.0°C/min cooling rate and 15°C/cm temperature gradient and magnification 10.4 . . . 53

VI-2. Photograph sequence of confocal system data for 0.5°C/min cooling rate and 15°C/cm temperature gradient and magnification 19.8 . . . 55

VI-3. Photograph sequence of particle tracker data for 1.0°C/min cooling rate and 15°C/cm temperature gradient and magnification 10.4 57

VI-4. Photograph sequence of particle tracker data for 0.5°C/min cooling rate and 15°C/cm temperature gradient and magnification 19.8 59

VI-5. Null height (h_n) and thickness (t_n) as a function of time for 0.3°C/min cooling rate and 15°C/cm temperature gradient 61

VI-6. Null height (h_n) and thickness (t_n) as a function of time for 0.5°C/min cooling rate and 15°C/cm temperature gradient 62

VI-7. Null height (h_n) and thickness (t_n) as a function of time for 1.0°C/min cooling rate and 15°C/cm temperature gradient 63

VI-8. Null height (h_n) and thickness (t_n) as a function of time for 2.0°C/min cooling rate and 15°C/cm temperature gradient 64

VI-9. Null height (h_n) and thickness (t_n) as a function of time for 3.0°C/min cooling rate and 15°C/cm temperature gradient 65

VI-10. Null height (h_n) and thickness (t_n) as a function of time for 0.3°C/min cooling rate and 28°C/cm temperature gradient 66

VI-11. Null height (h_n) and thickness (t_n) as a function of time for 0.5°C/min cooling rate and 28°C/cm temperature gradient 67

VI-12. Null height (h_n) and thickness (t_n) as a function of time for 1.0°C/min cooling rate and 28°C/cm temperature gradient 68

VI-13. Null height (h_n) and thickness (t_n) as a function of time for 2.0°C/min cooling rate and 28°C/cm temperature gradient 69

VI-14. Null height (h_n) and thickness (t_n) as a function of time for 3.0°C/min cooling rate and 28°C/cm temperature gradient 70

VI-15. Vortex top height (h_t) as a function of time for 15°C/cm temperature gradient and five cooling rates (CR in °C/min) 71

VI-16. Vortex center height (h_c) as a function of time for 15°C/cm temperature gradient and five cooling rates (CR in °C/min) 72

VI-17. Vortex top height (h_t) as a function of time for 28°C/cm temperature gradient and five cooling rates (CR in °C/min) 73

VI-18. Vortex center height (h_c) as a function of time for 28°C/cm temperature gradient and five cooling rates (CR in °C/min) 74

VI-19. Aspect ratio (l_v/w_v) of vortices versus time for five cooling rates at 15°C/cm temperature gradient (CR in °C/min) 78

VI-20. Aspect ratio (l_v/w_v) of vortices versus time for five cooling rates at 28°C/cm temperature gradient (CR in °C/min) 79

VI-21. Comparison of null height and vortex top height versus time for 1.0°C/min cooling rate and 15°C/cm temperature gradient 81

VI-22. Schematic of density profile before and after breakdown in the diffusion layer 83

VI-23. Front view of convection at 1.0°C/min and 15°C/cm temperature gradient 85

VI-24. Side view of convection illustrating three dimensional structure, at 1.0°C/min cooling rate and 15°C/cm temperature gradient . . . 86

VII-1. Critical Rayleigh number variation with initial mushy-zone height (from reference 12) 88

NOMENCLATURE

α	denotes the A rich phase in a phase diagram
β	denotes the B rich phase in a phase diagram
β_s	solutal coefficient of expansion $((\text{wt}\%)^{-1})$
β_t	thermal coefficient of expansion $(^\circ\text{C}^{-1})$
C	composition (usually in weight percent wt%)
CR	cooling rate (°C/min)
C_{eu}	compositon at the eutectic point (wt%)
C_o	bulk composition (wt%)
D	solutal diffusion coefficient (cm^2/s)
δ	is the entropy of melting multiplied by the constant ξ (cal/gm)
f	focal length (mm)
g	acceleration of gravity (cm/s^2)
G	temperature gradient (°C/cm)
h	fluid height (mm)
h_c	vortex center height from inside bottom of cuvette (mm)
h_n	null center height from inside bottom of cuvette (mm)
h_{n1}	null height at breakdown (mm)
h_{n2}	null height after breakdown (mm)
h_t	vortex top height from inside bottom of cuvette (mm)
κ	thermal diffusivity (cm^2/s)
k	partition coefficient
λ_w	wave length of vortex (mm)
L	denotes liquid region in a phase diagram
l_v	vortex length (vertical dimension mm)

n	index of refraction
n_{conc}	index of refraction as a function of concentration
n_t	index of refraction as a function of temperature
P_r	Prandtl number
R_a	combined Rayleigh number
R_{as}	solutal Rayleigh number
R_{at}	thermal Rayleigh number
S_c	Schimdt number
T	temperature (°C)
T_{eu}	eutectic temperature (°C)
T_s	solidus temperature (°C)
t_n	null thickness (mm)
w_v	vortex width (horizontal dimension mm)
ξ	constant as defined by Jackson and Hunt that depends on the crystallography of the growth interface
ν	kinematic viscosity (cm^2/s)

I. INTRODUCTION

The objective of this work was to experimentally study the fluid instabilities that lead to structural and compositional nonuniformities in directionally solidified superalloys. This was done by using the metal model material, NH_4Cl-H_2O. This metal model solidifies dendritically while rejecting solute that is lighter than the bulk liquid, as many superalloys do. In addition, since the metal model is transparent, it allows the use of optical techniques for studying the density gradients and fluid convection that result from the solidification process.

Considerable experimental work has been done with the NH_4Cl-H_2O metal model material. Fundamental experiments into the formation of channels (freckling) in NH_4Cl-H_2O have been done by Copley and Giamei [1]. They studied the effects of interface curvature and mold orientation on the number and distribution of channels in the liquid plus solid region (mushy-zone) of NH_4Cl-H_2O by observing the mushy-zone from above. Similar work was conducted by Sample and Hellawell [2] which included the effect of mold precession on the formation of channels in the mushy-zone. More detailed experiments were carried out by McCay (Johnston) and Owen [3]. These were the first experiments to use laser optical techniques (shadowgraph, Schlieren, and interferometry) to study the temperature and concentration gradients in a solidifying NH_4Cl-H_2O system.

Although the optical techniques discussed in reference [3] are valuable in determining the density distribution and gross fluid movements in a solidifying system, they do not provide detailed information of complex convective flow geometries which can exist in such systems. The research reported here examined the convective breakdown of the growth front diffusion layer in a solidifying NH_4Cl solution by two methods.

The first used a confocal optical imaging system to visualize the density changes that generate the fluid instabilities and the second employed particle light scattering and tracking to examine the actual fluid motion that results from these fluid instabilities. The confocal system produces an image similar to that of an interferometer but the device is much simpler and more rugged. The side scattering system uses small tracer particles illuminated by an intense sheet beam of laser light so that their motion can be recorded photographically by a long time exposure.

Using these methods, it was discovered that the instability occurring in the diffusion layer was a classic Rayleigh - Benard solutal instability that resulted in an initial cellular convection above the growth interface. This is contrary to previous work [4] that concluded the instability was the result of double-diffusive effects rather than a static instability resulting from a density inversion.

II. BACKGROUND

Casting

In a typical casting the solid that forms at the chill face is a thin layer of randomly oriented crystals. The crystals that are favorably aligned with the heat flow direction grow more rapidly than the others forming long columnar grains perpendicular to the chill face and parallel to the heat flow direction. For high cooling rates (as is the case for most uncontrolled cooling situations), the bulk liquid can easily become undercooled. The reason for the undercooling is due to the fact that the growth in the columnar region is dependent on diffusion of solute and latent heat at the dendrite tips. Therefore, if the temperature of the interface is changing rapidly, the diffusion limited growth process will not be able to keep up with the temperature change. As a result, the fluid in front of the interface will become undercooled. If the bulk liquid in front of the columnar zone is slightly undercooled and there are sufficient nucleants in this region, small equiaxed grains will form. Most often these nucleants are pieces of broken dendrite arms that are carried into the bulk region by convection. The resulting solid [5] consists of a thin layer of randomly oriented crystals at the outer wall (chill zone), a columnar region perpendicular to the mold walls (columnar zone), and an equiaxed region in the center of the casting (equiaxed zone) as can be seen in Figure II-1.

There are two kinds of composition nonuniformities which occur during casting and which affect metal properties. The first is called macrosegregation which is a large difference in composition across the entire volume of the metal [5]. It is caused by convective motion due to thermal and solutal fluid instabilities as well as by contraction and expansion of solidifying species and also by settling

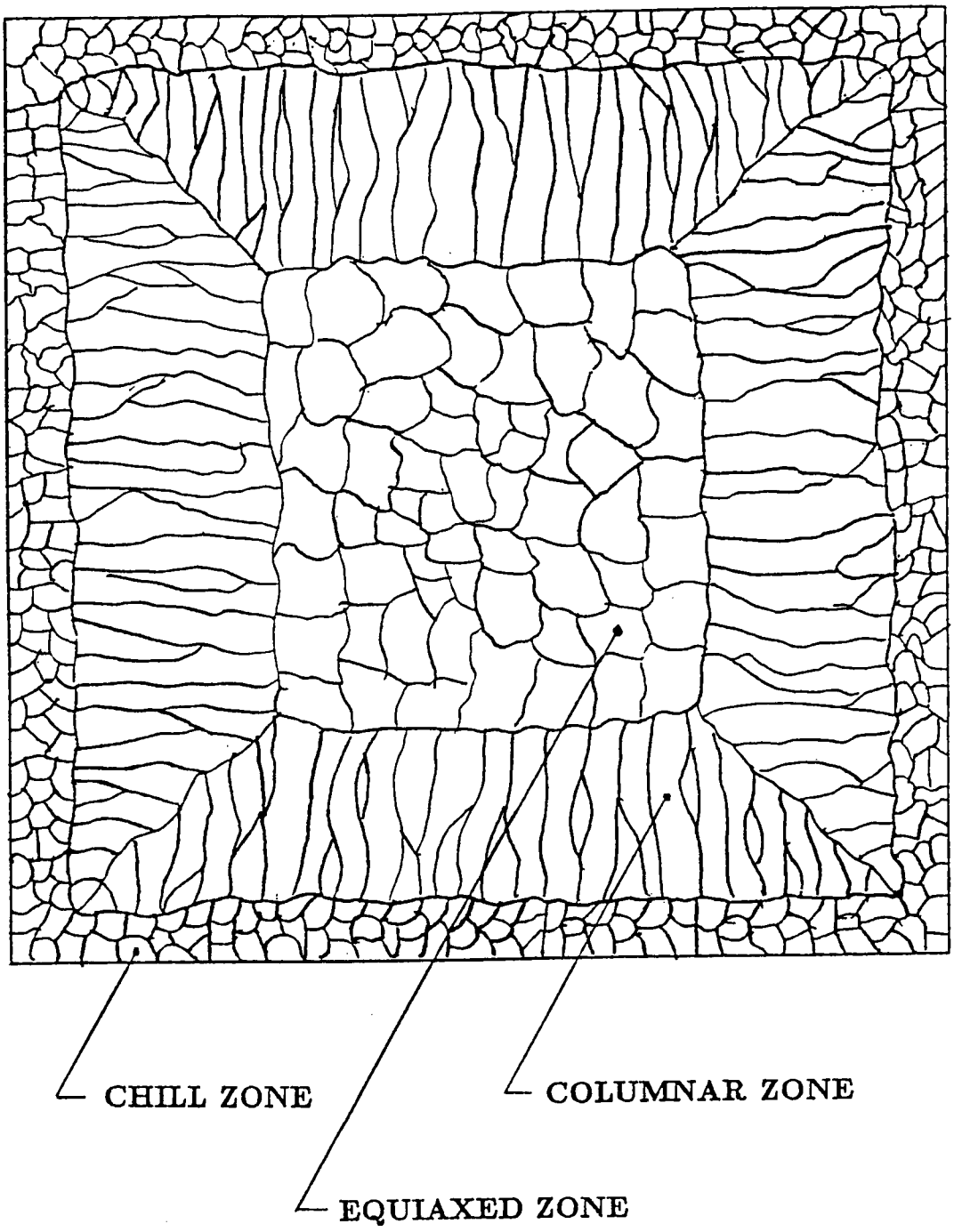


Figure II-1. Typical ingot casting.

due to gravity. Microsegregation, the second type of composition nonuniformity, is caused by the solidification process itself. It is due to the constant change of composition, as the temperature is lowered, of the solid composition along the solidus and the liquid composition along the liquidus (Fiqure II-2). For most metals, the solid and liquid diffusion rates are significantly slower than the solidification rate. As a result, the solid will have a cored or layered structure. Since the composition of liquid in contact with the solid has a different composition from that of the bulk liquid (Figure II-3), it is either lighter or heavier than the bulk liquid and can create fluid flows which generate macrosegregation.

Many materials are unidirectionally solidified in order to control the properties and uniformity of the finished structure. A schematic of the directional solidification process is shown in Figure II-4. Directional solidification is being accomplished by cooling one end of the mold and heating or insulating the opposite end so that the metal solidifies from one direction only. This is unlike conventional casting techniques where the metal is cooled by all of the mold wall surfaces.

During solidification, solute is rejected at the interface. This forms a diffusion boundary layer since this solute has a different concentration than the bulk liquid at the initial overall composition C_o. The composition of the rejected solute is dictated by the point on the phase diagram where the interface temperature intersects the liquidus (Figure II-2). Once the diffusion layer achieves equilibrium, solidification will reach a steady state where the solid approaches the overall composition C_o and the liquid composition at the interface approaches C_o/k, where k is the ratio between the liquidus and the solidus compositions at a constant temperature (Figure II-5). This creates a diffusion profile where the composition at the interface jumps from C_o in the solid to C_o/k in the liquid

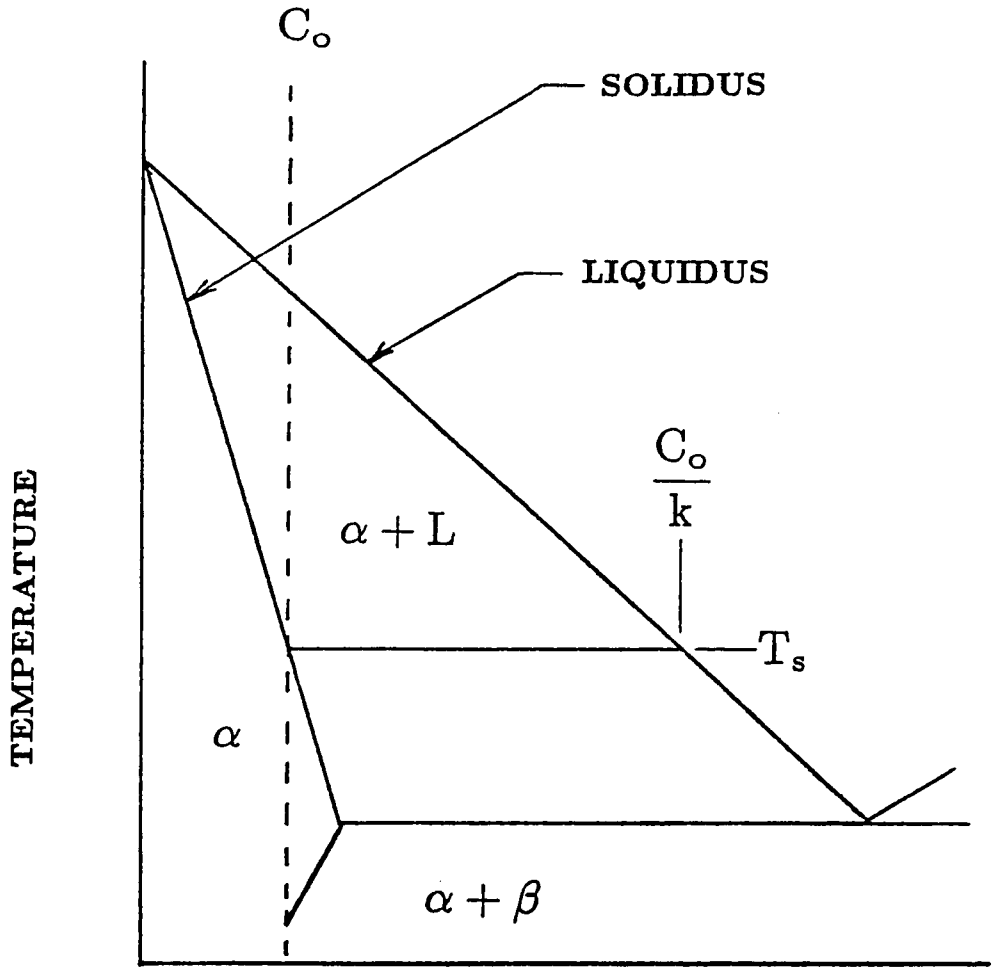


Figure II-2. Typical two phase region in a binary system.

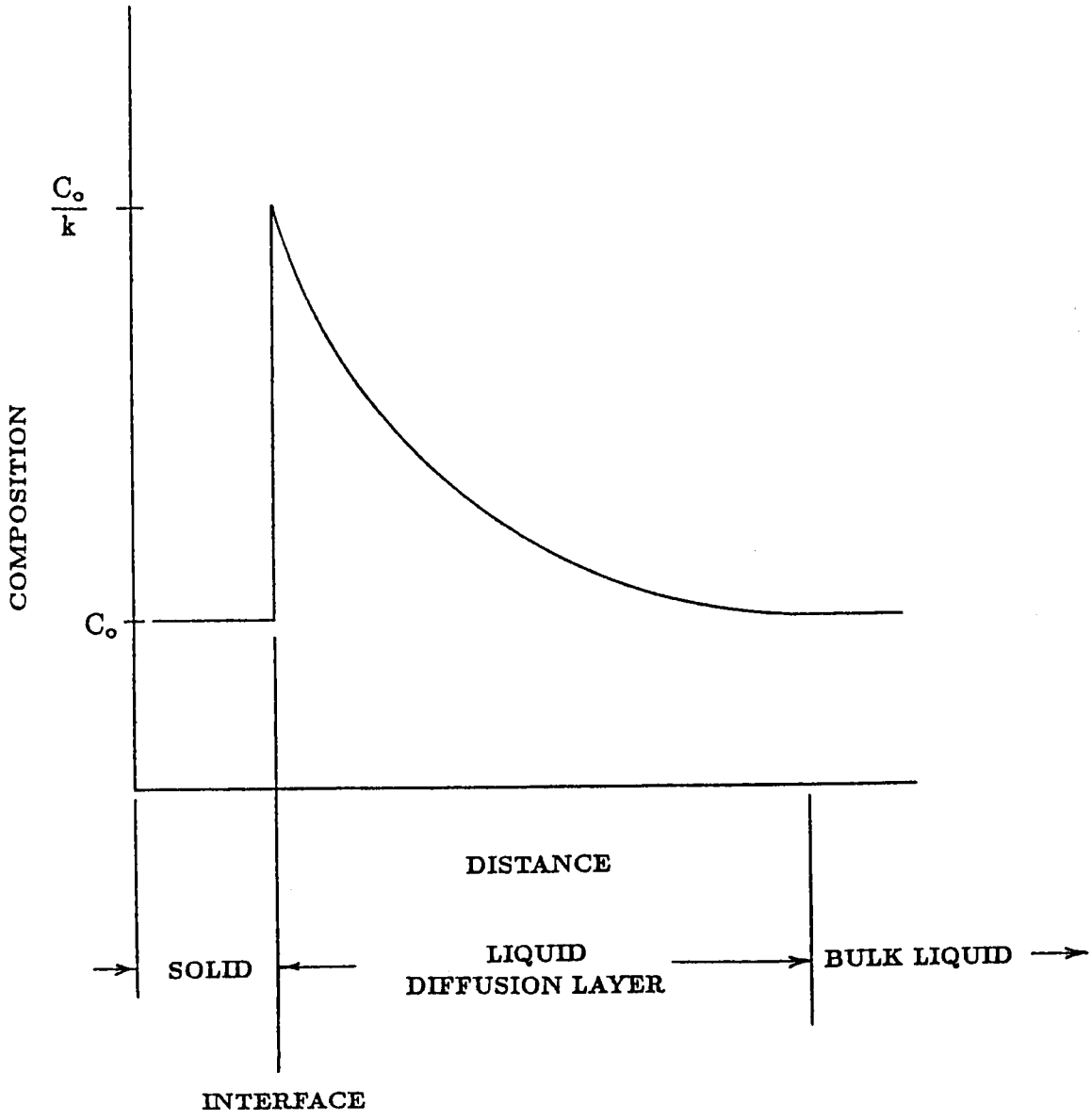


Figure II-3. Typical solute diffusion profile during plane front solidification.

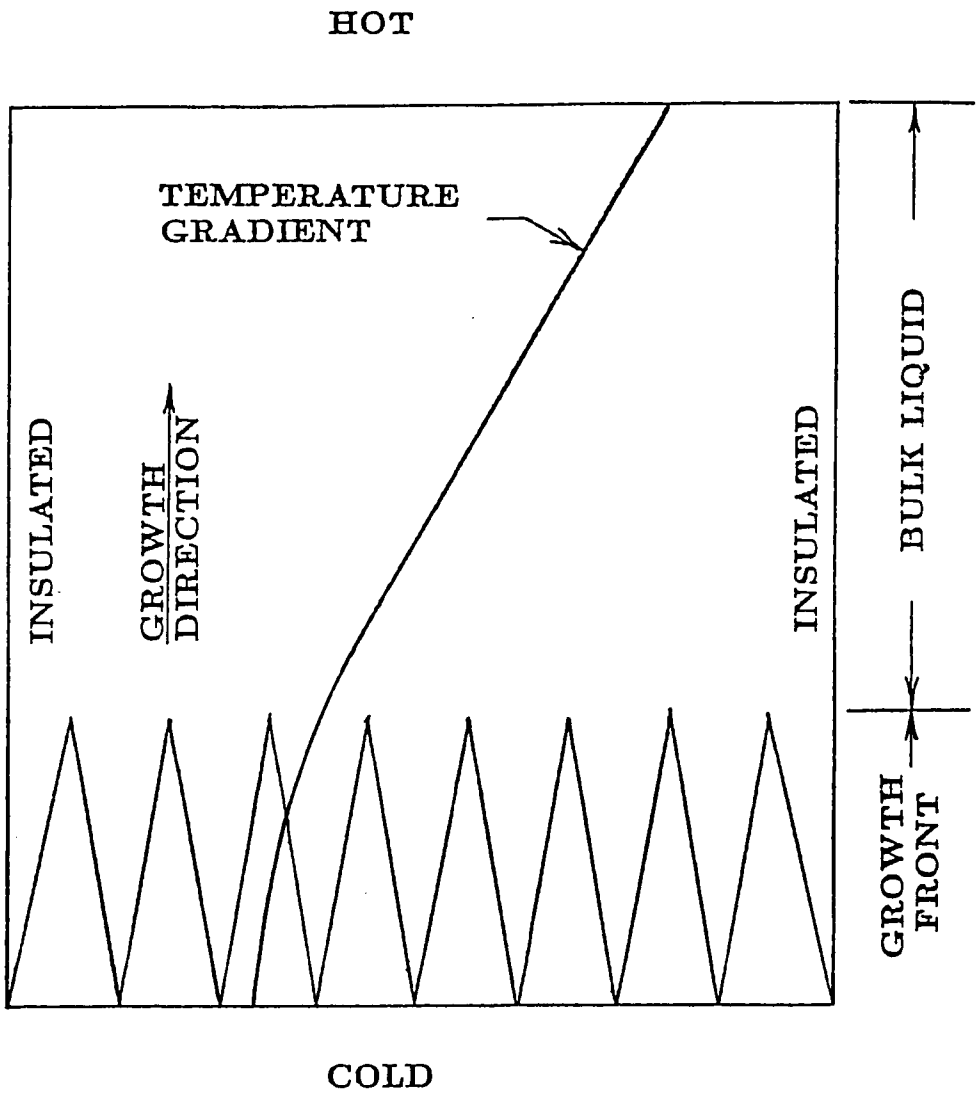


Figure II-4. Schematic of directional solidification process.

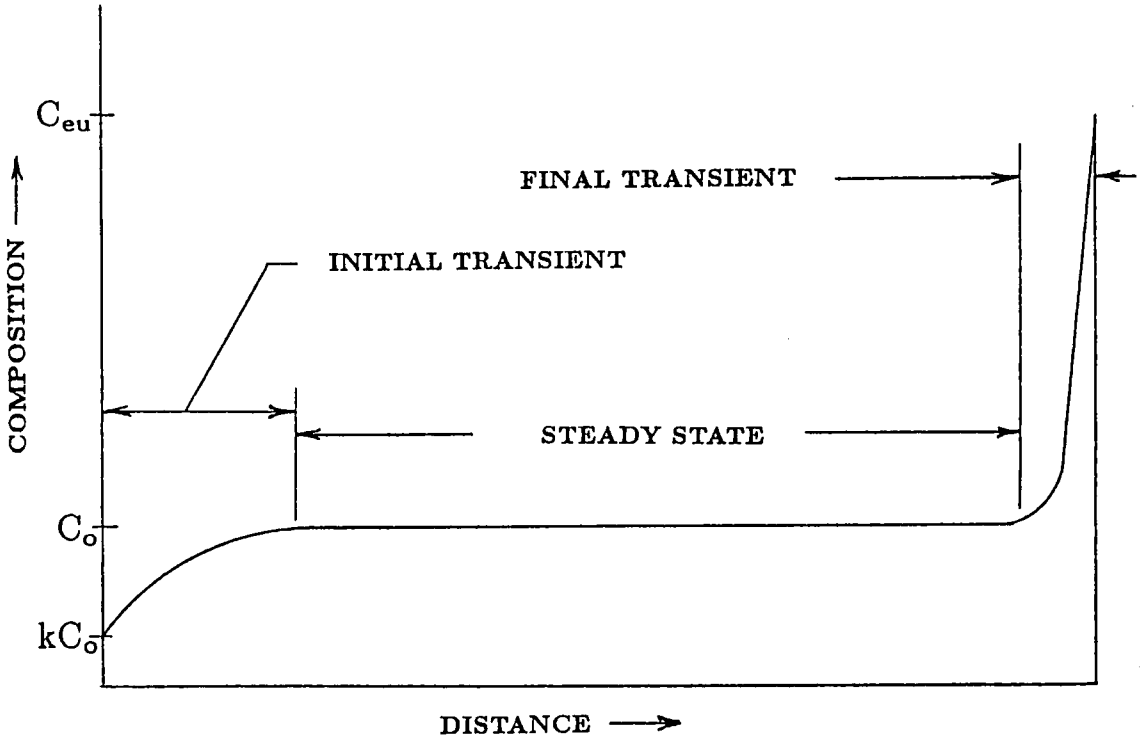


Figure II-5. Final solid composition distribution after solidification.

(Figure II-3). This liquid concentration then decreases asymptotically to C_o. Near the end of solidification, the diffusion layer meets the far wall of the mold; this generates a final concentration transient where the concentration of the solid and liquid must rise since there is no remaining bulk liquid region (Figure II-5) [5].

A directionally solidified casting structure consists of long columnar grains having the same crystallographic orientation. Macrosegregation is generally confined to the initial and final transients described above. Microsegregation, which is a product of the solidification process itself, still occurs across individual dendrites. Fortunately, its consistency and extent can be partially controlled by manipulation of the solidification process. This is accomplished by controlling parameters such as the cooling rate and temperature gradient. Usually these castings are cooled very slowly to reduce convection and lower microsegregation through diffusion. If the goal of structural uniformity is achieved, then the working properties are also uniform. In addition, inclusion size and distribution as well as microporosity are all generally favorable for directionally solidified materials [5]. The improved high temperature strength and creep properties of these structures make them very useful in applications where high stress and temperatures are encountered.

Metal Models

Metal models are simply transparent materials that freeze like metals [6] . Jackson and Hunt [6] have characterized the suitability of certain compounds for use as metal models by the use of a parameter δ which is the entropy of melting of the compound multiplied by a constant ξ that depends on the crystallography of the growth interface. For close packed crystallographic planes ξ is between .5

and 1. Compounds with small δ (less than one), and hence small entropies of melting are likely to solidify dendritically like most metals. Compounds with δ approximately two are likely to grow with a faceted interface, like a few metals and semiconductors. Thus compounds with δ much greater than one are not good choices for metal models.

The use of these metal model materials came about because of a need to directly observe the solidification process within a system. Metals are opaque which only allows observation of the metal's surface during the solidification process. The growth interface structure must be observed on a post facto basis, by a rapid quench, then sectioning and observing the frozen interface. In a metal model material, the dendrite structure and surrounding fluid can be observed optically (e.g. interferometry, Schlieren, double exposure holography and particle tracking) in real time. In addition, because of their low melting points most metal model materials are easier to handle than molten metals [6].

The metal model material used in this experiment was NH_4Cl - H_2O which solidifies dendritically similar to many important metal alloys . The concentration used was 28 wt% NH_4Cl - H_2O, which is the room temperature (24 °C) saturation point of the solution.

The NH_4Cl - H_2O Eutectic

Eutectics. When two constituents A and B are not completely soluble in each other they sometimes form a eutectic. The addition of one to the other reduces the melting point of the mixture leading to the typical vee (V) appearance of the eutectic phase diagram. The point at the bottom of the V where the liquidus curves meet is the minimum melting point composition, called the eutectic point (Figure II-6). Compositions between the solid solubility limit of

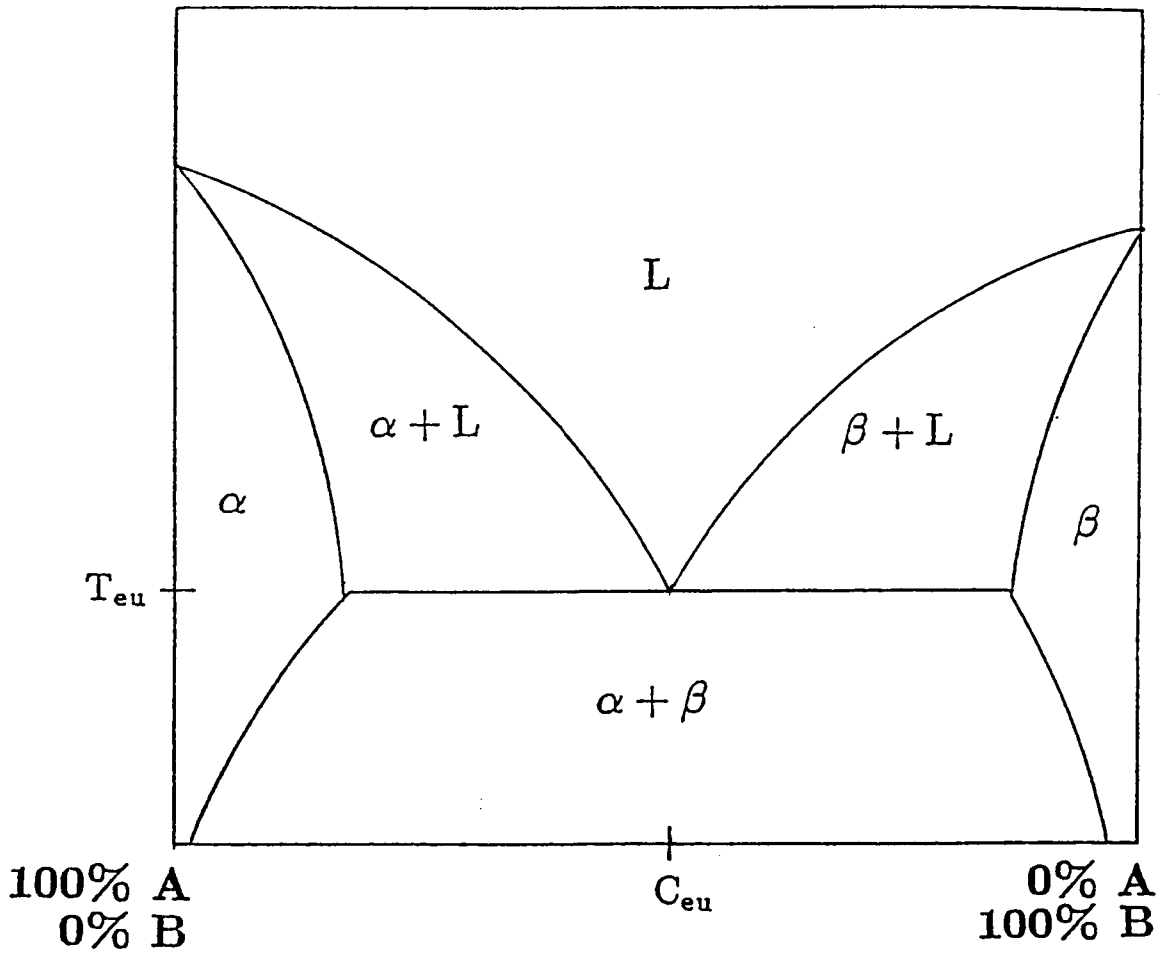


Figure II-6. Typical eutectic phase diagram.

the A rich, α phase, and the solid solubility limit of the B rich, β phase, forms a structure composed of the eutectic, with the composition of the eutectic point, and either the pro-eutectic α or β phases. For compositions to the left of the eutectic point (hypoeutectic), α phase forms in the temperature range between the melting point of pure A and the eutectic temperature. When the temperature is lowered below the eutectic temperature the remaining liquid is converted to eutectic. The resulting solid consists of the proeutectic α phase and the eutectic phase. If the composition is to the right of the eutectic (hypereutectic) then the resulting solid will consist of the proeutectic β phase and the eutectic phase. If the composition is at the eutectic point all of the solid will become eutectic with the minimum melting point of all compositions (Figure II-6). The NH_4Cl - H_2O system is a typical eutectic system with H_2O as one terminal phase and NH_4Cl as the other (Figure II-7).

A solid of the eutectic composition is composed of the α and β phases. The type of microstructure that forms is dependent on the relative proportion of the α and β phases and on the crystallography of the two phases [7]. The dependence on crystallography is not yet fully understood. If the proportion of α and β phases is about the same, the solid usually consists of alternating layers of the α and β phases. If one phase predominates in the mixture of the α and β phases, the predominant phase will surround the lesser phase. The shape of this lesser phase determines the type of eutectic structure. If this lesser phase is round the eutectic is called *nodular, globular,* or *spheroidal.* If this phase is in the form of flat platelets the eutectic structure is called *acicular.* Another type of structure where the lesser phase grows dendritically through the matrix of the other phase is called *Chinese script.*

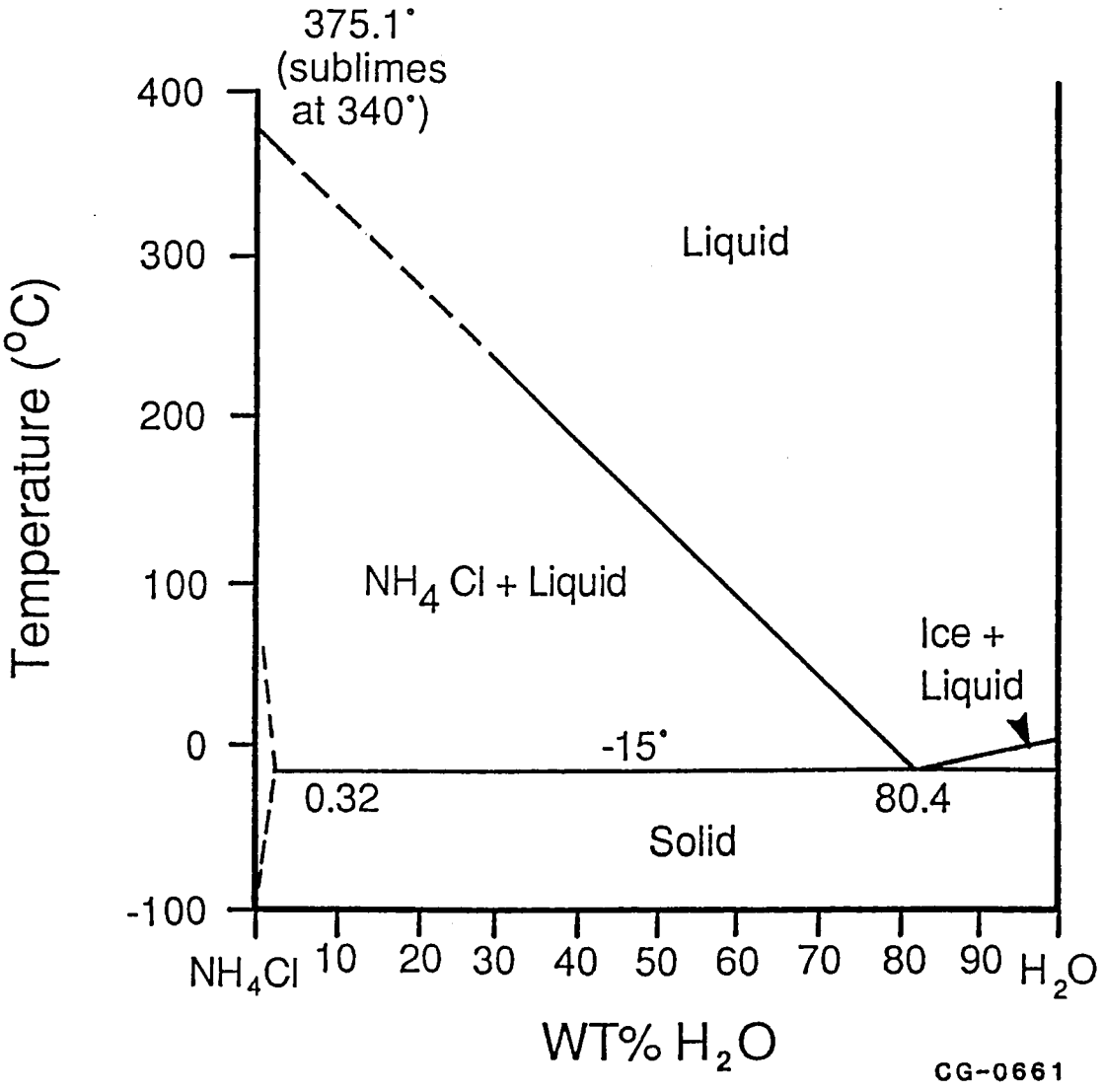


Figure II-7. Ammonium chloride - water phase diagram.

Properties of NH_4Cl-H_2O.

Diffusion coefficient. The diffusion coefficient of NH_4Cl in H_2O as a function of composition is given in Figure II-8. It is generally linear over the 21-28wt% range and can be approximated by $2.3X10^{-5}cm^2/s$. Over larger ranges it is a non-linear function of composition and varies from $1.8X10^{-5}cm^2/s$ to $2.3X10^{-5}cm^2/s$.

Index of refraction. Index of refraction data for NH_4Cl - H_2O as a function of temperature and concentration were obtained by McCay (Johnston) et al [8] using an optical refractometer. That data has been reproduced in Figure II-9 and II-10. The index of refraction is a linear function of temperature which can be described by

$$n_t = 1.38594 - \frac{T}{8034.375} \ . \qquad (1)$$

For a temperature of 22°C, the index of refraction can be described by

$$n_{conc} = 1.33262 + \frac{wt\%}{534.682} \ . \qquad (2)$$

Density. The density of NH_4Cl - H_2O is an almost linear function of NH_4Cl concentration and temperature (Figures II-11 and II-12).

General properties of NH_4Cl. A list of the general properties of NH_4Cl - H_2O is given in Table II-1. The general properties of solid NH_4Cl are given in Table II-2. Ammonium chloride has a density of about 1.5 times that of water and a high index of refraction (1.642) which makes NH_4Cl - H_2O ideal for optical systems that depend on index of refraction changes.

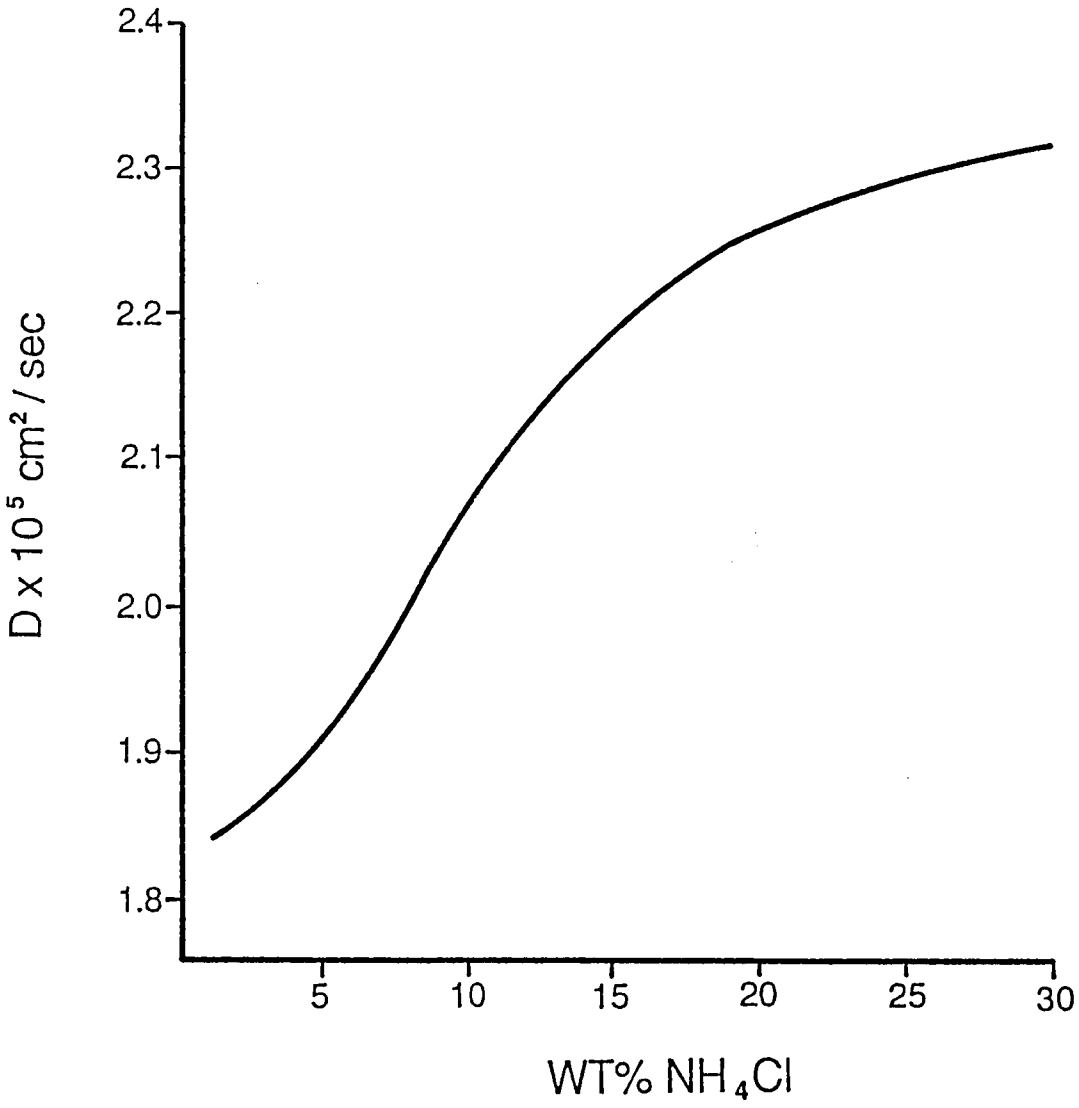


Figure II-8. Diffusion coefficient of NH_4Cl - H_2O as a function of composition.

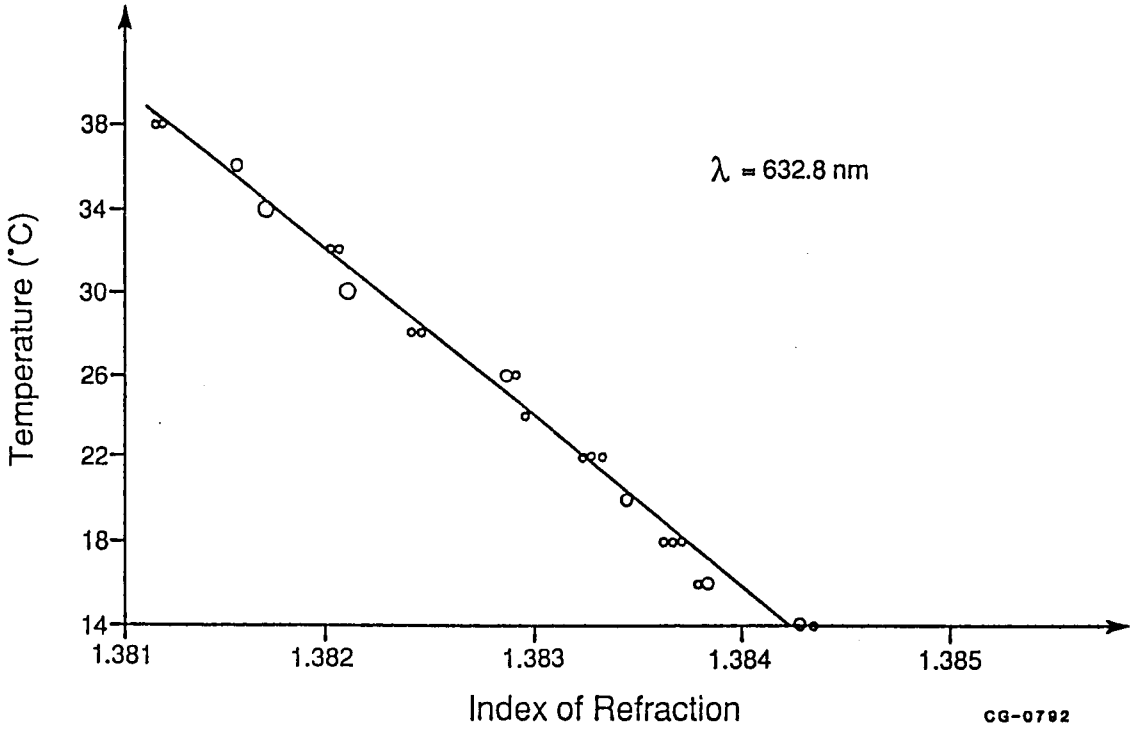


Figure II-9. Index of refraction of NH_4Cl - 72.93 wt% H_2O as a function of temperature (from reference 8).

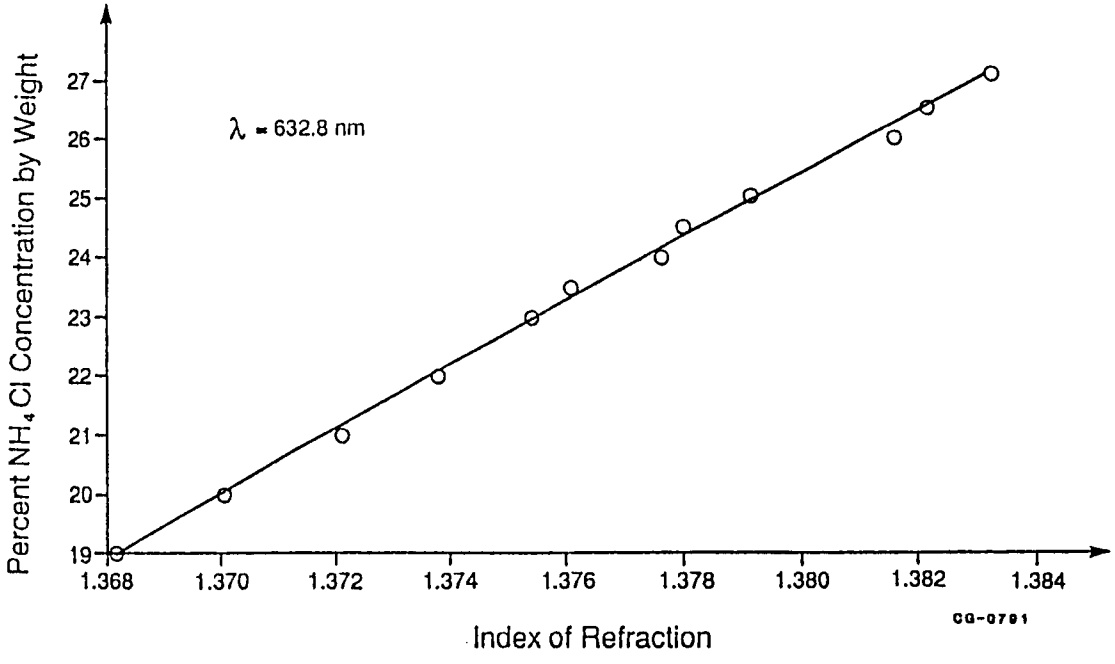


Figure II-10. Index of refraction of NH_4Cl - H_2O at 22°C as a function of composition (from reference 8).

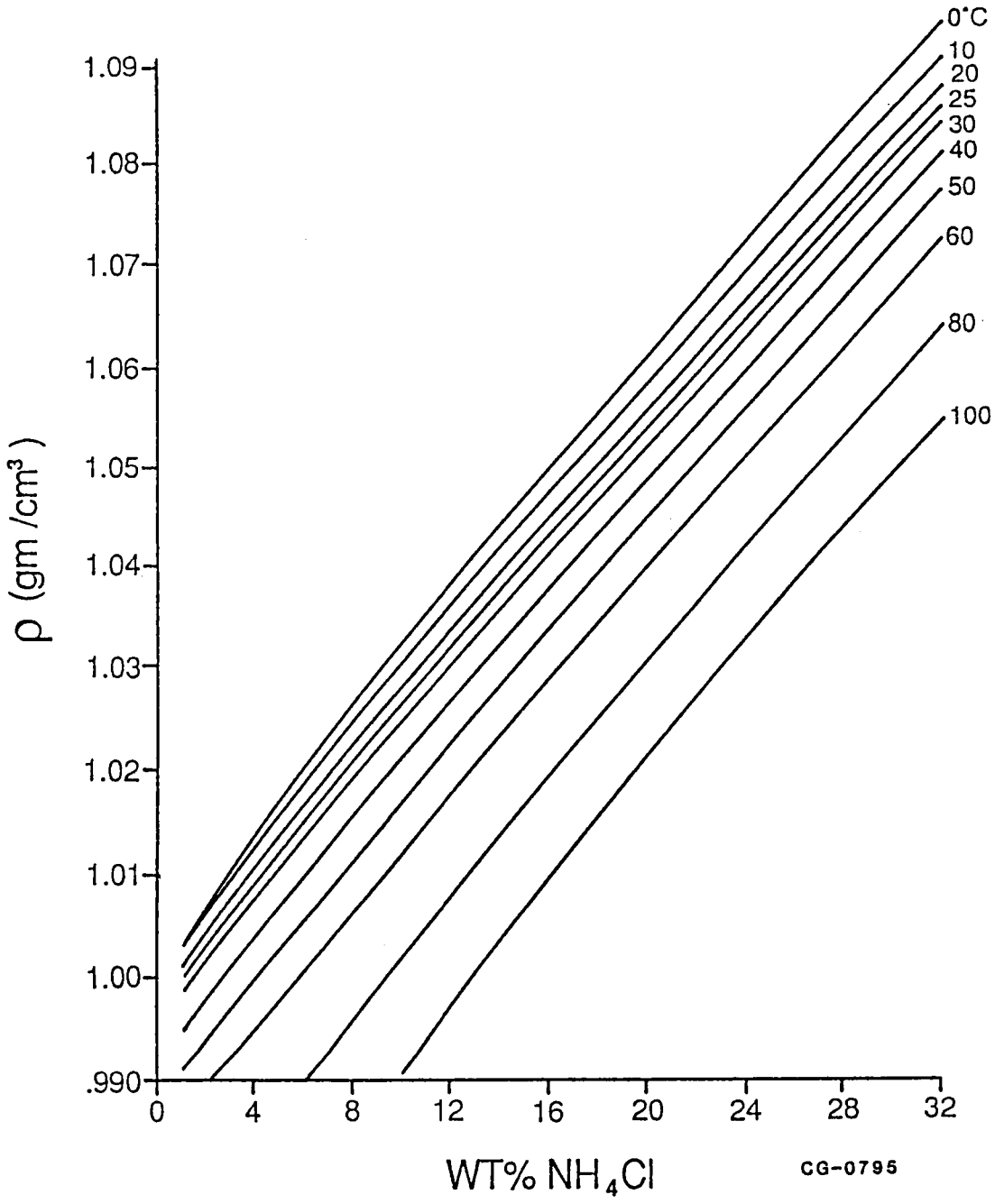


Figure II-11. Density of NH_4Cl - H_2O as a function of composition for selected temperatures.

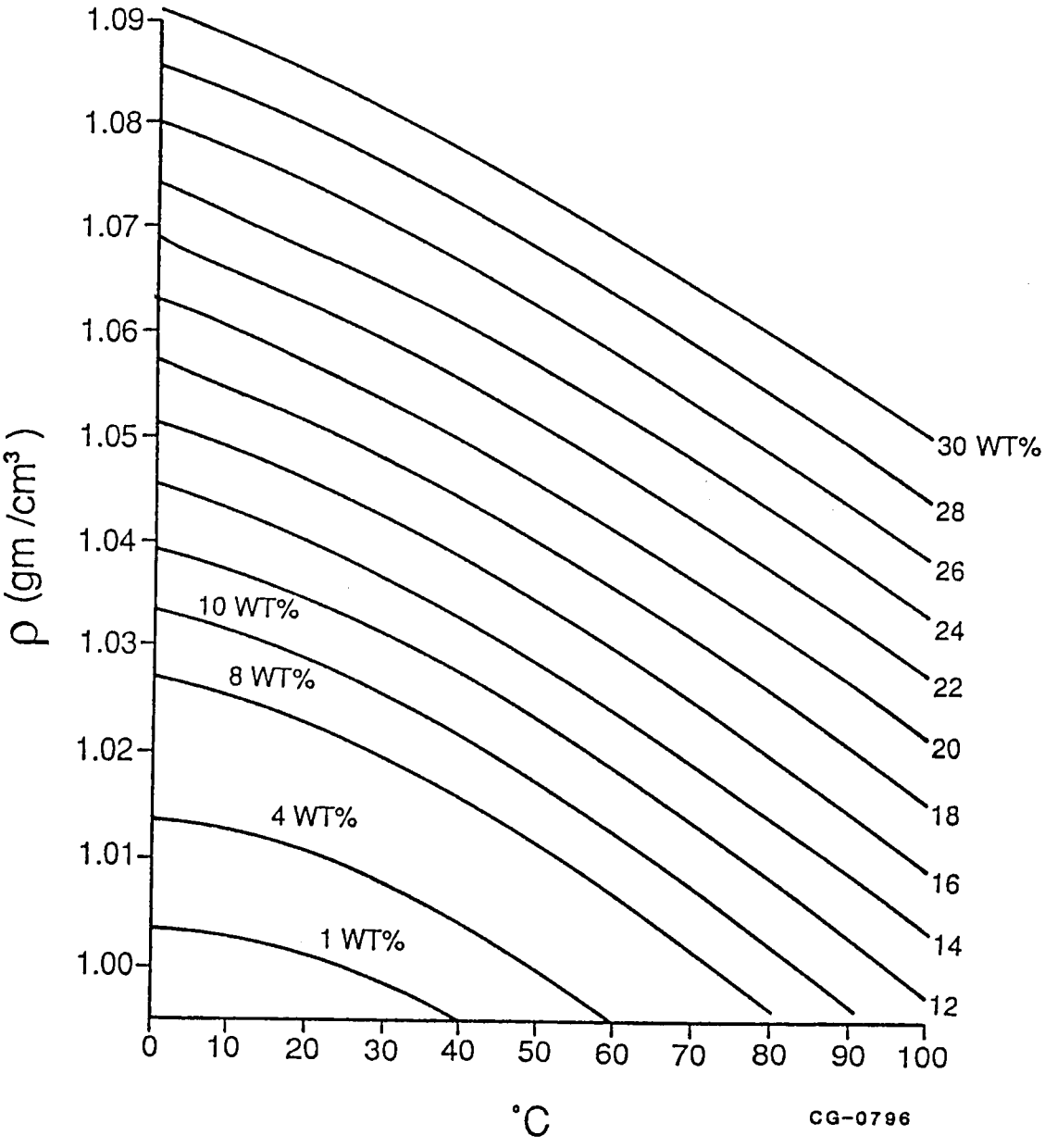


Figure II-12. Density of NH_4Cl - H_2O as a function of temperature for selected compositions.

Table II-1. Properties of 28wt% NH_4Cl - H_2O at 25°C.

Property	Value
Heat of solution	66.04 cal/gm
Specific heat	0.789 cal/gm °C
Partition coefficient	0.0039
Diffusion coefficient (28wt%NH_4Cl)	$2.302 \times 10^{-5} cm^2/sec$
ph	5.0
Density (25°C)	$1.0767\ gm/cm^3$
Viscosity (25°C)	1.058 poise
Index of refraction (22°C)	1.3836
Liquid fraction at eutectic point	89%
Thermal conductivity	1.204×10^{-3}cal/cm sec °C
Thermal diffusivity	$1.5 \times 10^{-3} cm^2/sec$
Pr	6.2
Sc	517
β_t/°C	2.95×10^{-4}
β_s/wt%	-2.81×10^{-3}

Table II-2. Properties of 28wt% NH_4Cl - H_2O.

Property	Value
Lattic constant	3.8756 Å
Crystal structure	$B_2(CsCl)$
Molecular weight	53.5
Elastic constants	
C_{11}	3.90
C_{44}	0.68
C_{12}	0.72
Growth orientation (slow)	[100]
Thermal linear expansion coefficient	62.55×10^6 °C^{-1}
Index of refraction	1.642
Density	1.5256 gm/cm^3
Melting point	Sublimes 340°C

NH_4Cl structure. In a ordered binary crystal structure, the two constituents always occupy the same relative positions. Ammonium chloride has a CsCl type of structure with the chloride ions located in a cubic pattern about an ammonium ion in the center of the cube (Figure II-13). If this structure is maintained throughout, as it is in NH_4Cl, it is said to have long range order. The lattice parameter of the unit cell is 3.8756 Å [9].

Optical Techniques

Visualization of density changes. There are several optical techniques that can be used to study the index of refraction (density), changes within a solidifying metal model system. The simplest of which is the shadowgraph technique. The shadowgraph is created when a collimated beam of light is shined through the sample. The index of refraction changes are seen in the projected shadow of the beam leaving the sample. These changes show up as light or dark regions depending on how the light was refracted in passing through the sample. This method is best for determining large index of refraction changes and is not suitable for visualizing subtle changes or for quantitative work.

Another method that produces a change in intensity in response to index of refraction changes in the sample is the Schlieren technique. In this method, a coherent collimated beam of light is shined through the sample and a convex lens focuses the light to a knife edge. The light that is not blocked by the knife edge is then projected onto a ground glass screen for viewing or photographing from rear. The light that makes it around the knife edge is that which is refracted off the optical axis due to the index of refraction change in the sample. The sensitivity of the Schlieren system is much better than that of the shadowgraph since much of the unchanging light from the sample is filtered out by the knife edge. It is very

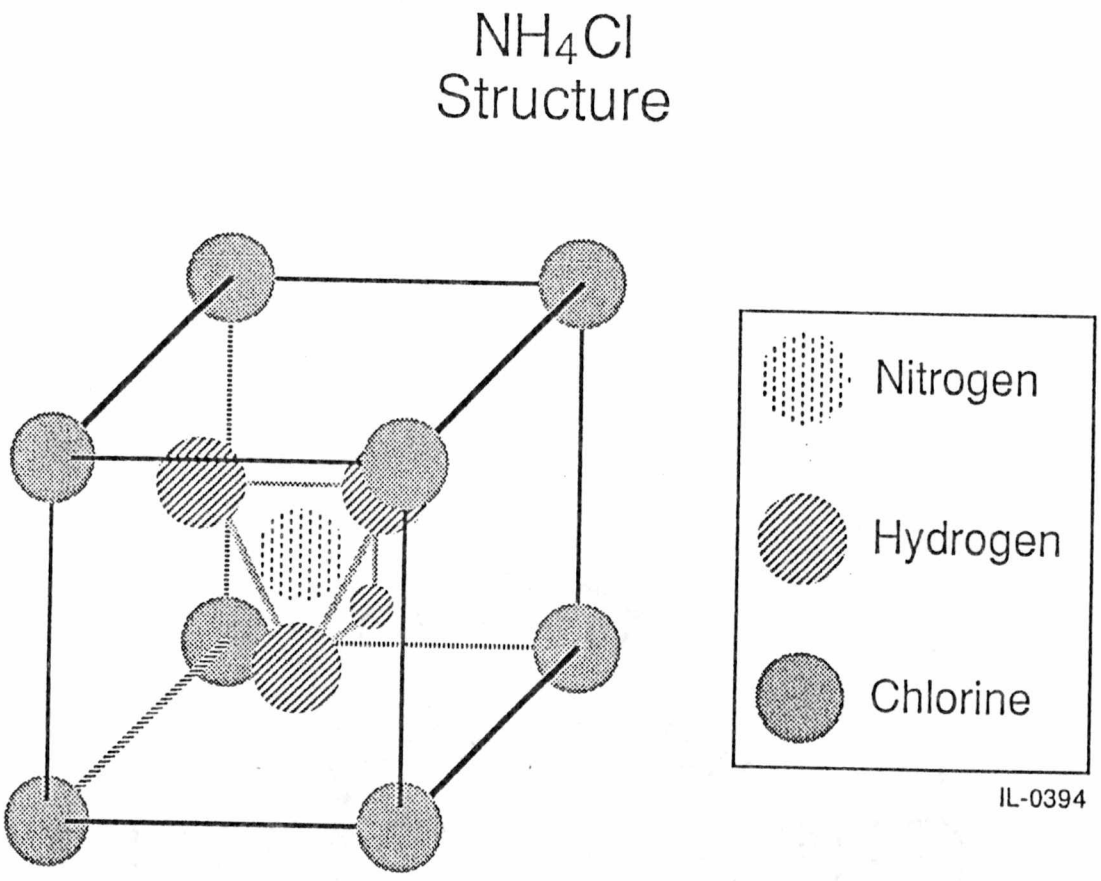


Figure II-13. NH_4Cl crystal structure.

difficult to obtain quantitative data with these methods which yield changes of image intensity is response to index of refraction changes. However, these methods are valuable for determining the distribution of density in the sample.

The confocal optical imaging system makes use of spatial filtering (Figure II-14). The confocal system is a coherent optical computer [10] that is based on the concept of Fourier transforms. It consists of two lenses of equal focal lengths. The sample is located one focal length from the first lens. A collimated beam passes through the sample to this first lens. This lens images the Fourier transform of the sample onto its back focal plane (the Fourier transform plane). The second (inverse transform) lens is located two focal lengths behind the first lens and produces the inverse transform of the Fourier transform located between the two lenses, providing a real image of the object. If an obstructing object is placed at the Fourier transform between the two lenses to block part of the transform then the image located in the back focal plane of the second lens has been spatially filtered (i.e. part of the information from the object has been filtered out). This obstructing object can be any selected size or shape. In the case of a Schlieren confocal optical system it is a knife edge. Other objects can be placed at the Fourier transform plane to enhance the optical systems sensitivity to certain types of density changes. For instance, a dot at the focus of the first lens would filter out the DC portion of the Fourier transform formed by the sample. This arrangement produces a fringe system similar to that of an interferometer. The disadvantages to this method are that the fringes are of varying intensity and are sometimes hard to discern. The fringes can be used to calculate the index of refraction change that caused them. An advantage the technique has over interferometry is a relative insensitivity to vibration.

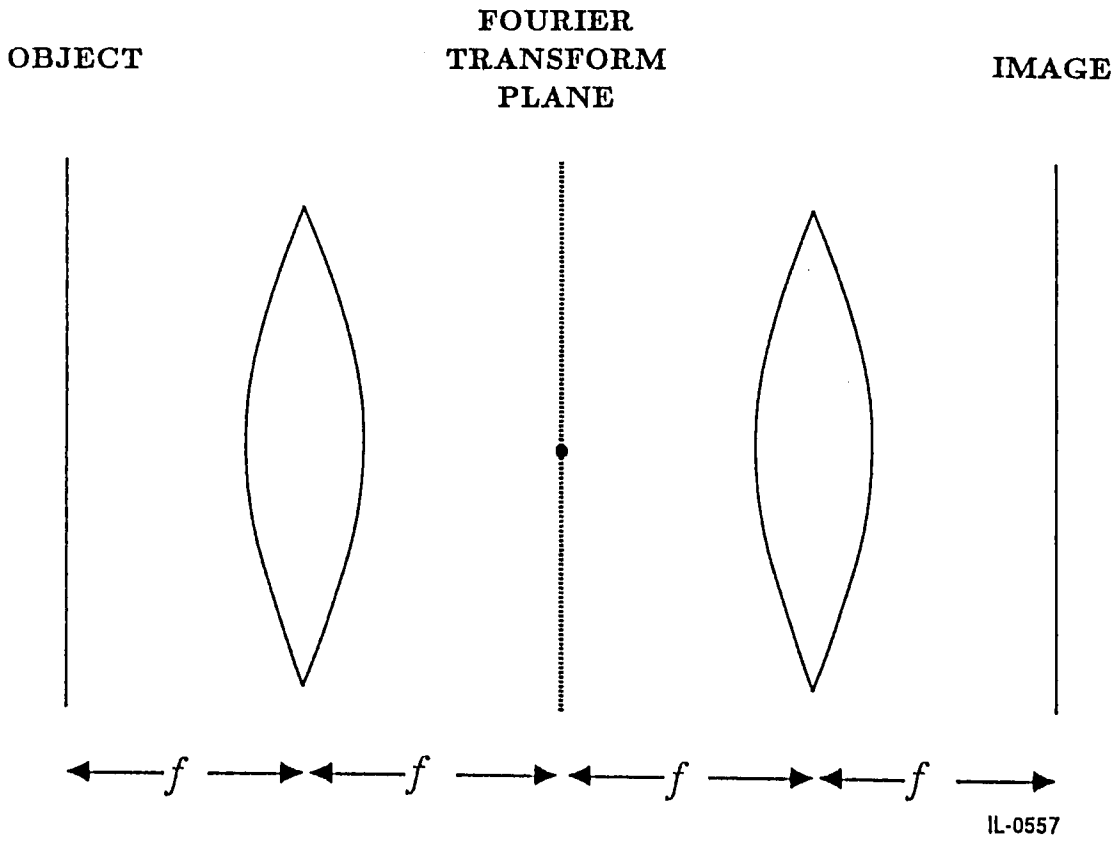


Figure II-14. Confocal optical imaging system.

Another technique is the Mach - Zender interferometer. It is based on the interference of two beams of collimated coherent light. This is achieved by splitting a single coherent collimated beam into two. The sample is located in one beam and the other beam is used as a reference. The two beams are recombined to produce an interference fringe pattern. A change in phase of the light from the sample causes a change in fringe spacing which can be measured and converted to an index of refraction change. This method is very sensitive, requiring a phase shift of only one half of a wavelength to produce a fringe. Because of this, it is very sensitive to vibrations and air currents. This method is more quantitative than those based on intensity since the fringe spacing can be related to the index of refraction.

Another technique that yields interference fringes is double exposure holography. This is done by creating a reference hologram of the sample. This hologram is a phase map of the sample and is used as phase reference on which to base index of refraction changes. Any change in the phase of the sample will be seen as interference fringes, as in the interferometer. The only difference is that the reference hologram can be taken at any time during the solidification process. The interference pattern is a result of the index of refraction changes that occurred since the last reference hologram was made and not the changes that occurred since the beginning of solidification. This method is considerably more complicated than the others since it requires specialized holography equipment as well as the stability required by the interferometer.

Flow visualization. The optical methods described previously can be used to track gross fluid movement but are of little use in determining complex flow geometries. One technique for studying small magnitude convective motions in a closed water based metal model system uses side scattering (Figure II-15) to

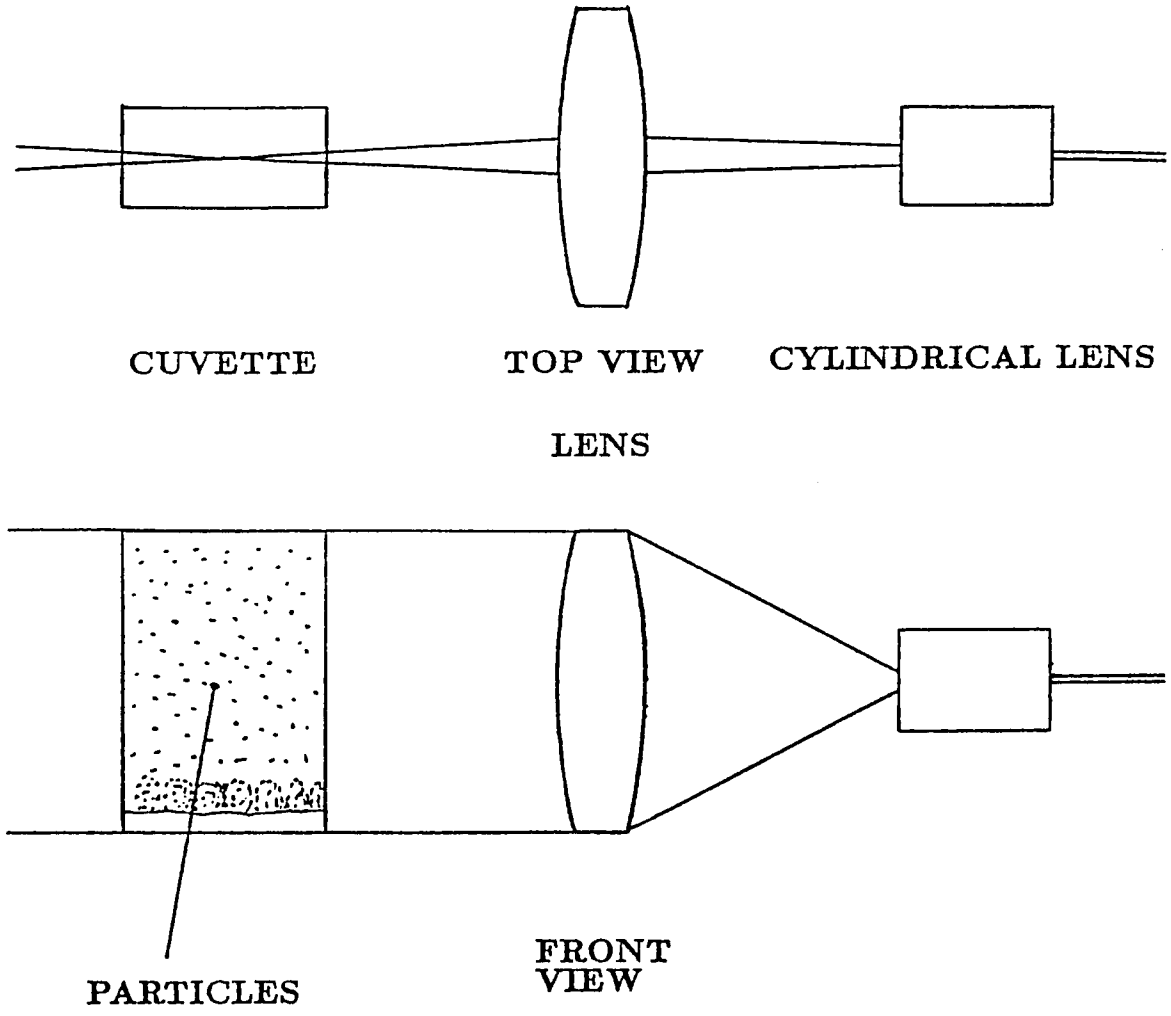


Figure II-15. Particle side scattering system.

illuminate the motion of small tracer particles that are suspended in the liquid portion of the sample. The particles are illuminated by a very intense sheet beam of light at an angle perpendicular to the direction of observation. The particle motion can then either be recorded by a movie camera or photographed using long time exposures. The latter method produces a streak path which can be used to determine the speed and direction of the convective flow.

Fluid Instabilities During Solidification

There are three major types of buoyancy driven fluid instabilities during solidification at one gravity. The first two, thermal and solutal, depend directly on the density gradient. If the density gradient is positive (heavier fluid on top) whether it is caused by a thermal gradient or a solutal gradient, the fluid will become unstable. If the density gradient is negative it is statically stable. The third type of instability is the double-diffusive instability, which depends on the relative magnitudes of the thermal and solutal diffusivities. A thorough review of these instabilities is given in the text by Zierep and Oertel [11]. The following discussions apply to conditions at one gravity with growth upwards.

Thermal instabilities. Thermal instabilities occur when the thermal gradient is negative (warmer fluid on bottom). The stability of this situation can be described by the thermal Rayleigh number [12].

$$R_{at} = \frac{gh^3\beta_t\Delta T}{\nu\kappa} \tag{3}$$

When the density inversion has reached a certain height and magnitude such that the critical Rayleigh number is reached, the fluid will begin to convect. This critical Rayleigh number can thus be used to predict the onset of convection

for different physical parameters that produce the same Rayleigh number (i.e. different temperature gradients and fluid heights).

For a fluid between two horizontal plates the convection takes the form of longitudinal convective rolls with fluid rising between the boundary of one pair of rolls and descending between another pair. For a fluid with a lower horizontal boundary and an upper free surface the flow geometry takes the form of 3-D Benard cells with fluid rising in the center of the hexagonal cell and descending around its periphery [11].

Solutal instabilities. Solutal instabilities occur when the solutal gradient generates a light layer beneath a heavy one. The stability of this situation can be described by a solutal Rayleigh number which is defined similar to the thermal Rayleigh number [12].

$$R_{as} = \frac{g\beta_s h^3 \Delta C}{\nu D} \tag{4}$$

When breakdown occurs (the critical Rayleigh number has been reached), the light fluid at the lower boundary will rise upward until it reaches the upper boundary where it will stay, and the heavy fluid will sink. If there is no longer a source of either the light or heavy fluid such as from a dissolving or precipitating solid, the driving force for the convection will quickly approach zero and a stable configuration will result.

A combined Rayleigh number can be defined that takes into account the solute and temperature gradients.

$$R_a = R_{as} + R_{at} \tag{5}$$

This defines the static stability of combined thermal and solute gradients. If this Rayleigh number is greater than the critical Rayleigh number then convection will occur.

Double diffusive instabilities. In this third type of instability a statically stable (negative density) gradient (light fluid on top) is not sufficient to to guarantee stability. The stability can depend on the relative magnitudes of the thermal and solutal diffusivities. There are two basic types of double diffusive instabilities as defined by Linden [13], both have statically stable density gradients. These are the finger instability and the diffusive instability. In the finger instability the solute gradient is destabilizing but a positive temperature gradient overides the solute gradient and produces a statically stable density gradient (lighter fluid on top). If the thermal diffusivity is large compared to the solute diffusity, the fluid is dynamically unstable. When a fluid element is perturbed upward it will quickly reach thermal equilibrium with the surrounding hotter fluid, but its concentration does not equilibrate as quickly due to the low solute diffusivity and the fluid element remains lighter than its environment. This fluid element will continue to rise. Similarly, if a fluid element is perturbed downward it will lose heat, becoming heavier than the surrounding fluid and continue to sink.

In the diffusive instability the thermal gradient is destabilizing and the solute gradient stabilizing. The stabilizing effect of the solute gradient overrides the destabilizing effect of the temperature gradient forming a statically stable density gradient. Assuming the thermal diffusivity is large compared to the solute diffusivity, a fluid element perturbed downwards gains heat faster than solute. Therefore, it will rise upwards overshooting its initial position, then it will loss heat becoming heavier and it will sink. This time it does not overshoot its initial

position as much. The oscillations will continue to get smaller with each cycle until the fluid element assumes its equilibrium position.

III. APPARATUS

Control System and Related Hardware

The control system consisted of six major elements, a computer, an input-output device, an operational amplifier/power supply assembly, a temperature controlled water bath, and a cuvette assembly (Figures III-1, III-2, III-3 and III-4). The computer recorded and interpreted the temperature data as well as controlled the temperature of the cuvette. It also controlled a shutter and a 35 mm camera by use of solid state relays (SSR). The computer was interfaced with an input/output device which accepted input from two control thermocouples at the top and bottom of the cuvette. The temperature inputs were from .005 inch diameter chromel-alumel (K-type) thermocouples to give fast response time. The temperatures from these thermocouples were used by a control program to calculate the voltage necessary to maintain the proper sample temperature. This voltage was sent from a D/A card to the operational amplifier assembly where the current was amplified sufficiently to drive the thermoelectric (heat pumping) devices (TEDs). Depending on the polarity of the input voltage these thermoelectric devices pump heat in either direction (i.e. heat or cool). They require a maximum power input of 54W (9V at 6A) which was provided by two very high power op amps. These op amps were powered by two 15V-15A DC power supplies. The temperature controlled bath provided a constant temperature water source to the TED heat sinks.

The cuvette assembly provided a means of aligning the cuvette with the thermoelectric heat pumping devices and the optical system. It consists of two water cooled copper heat sinks, four vertical aluminum struts, the TEDs, and the thermocouples. The bottom heat sink is rigidly mounted to the struts at each

CONTROL SYSTEM PARTS LIST

I. COMPUTER - IBM PC-XT with Keithly interface card.

II. INPUT/OUTPUT DEVICE - Keithly model 500-500 data aquisition system with AIM7 thermocouple card and AOM5 analog output card.

III. OP AMP/POWER SUPPLY ASSEMBLY

A. Op amps - two Burr Brown model OPA 512 SM.

B. DC power supplies - two Condor model F15-15.0.

IV. REFRIGERATED CIRCULATING BATH - Endocal model DTE -4DD.

V. CUVETTE ASSEMBLY (Figure III-3).

A. Two copper heat sinks.

B. Four aluminum angles.

C. Two thermoelectric devices - Melcore model CP1.4-71-045L.

D. Two copper plates - sized to fit TEDs.

Figure III-1. Control system parts list.

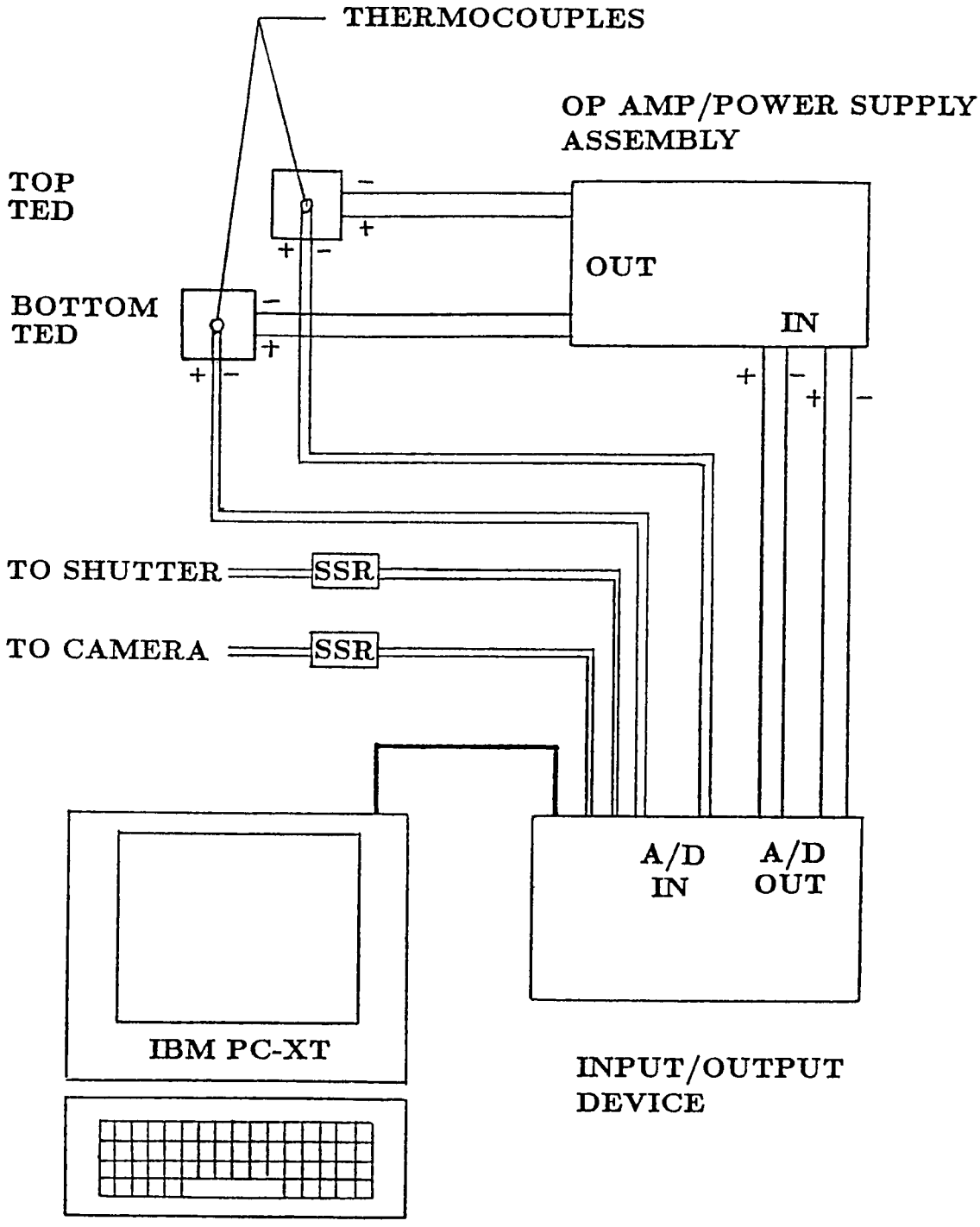


Figure III-2. Control system.

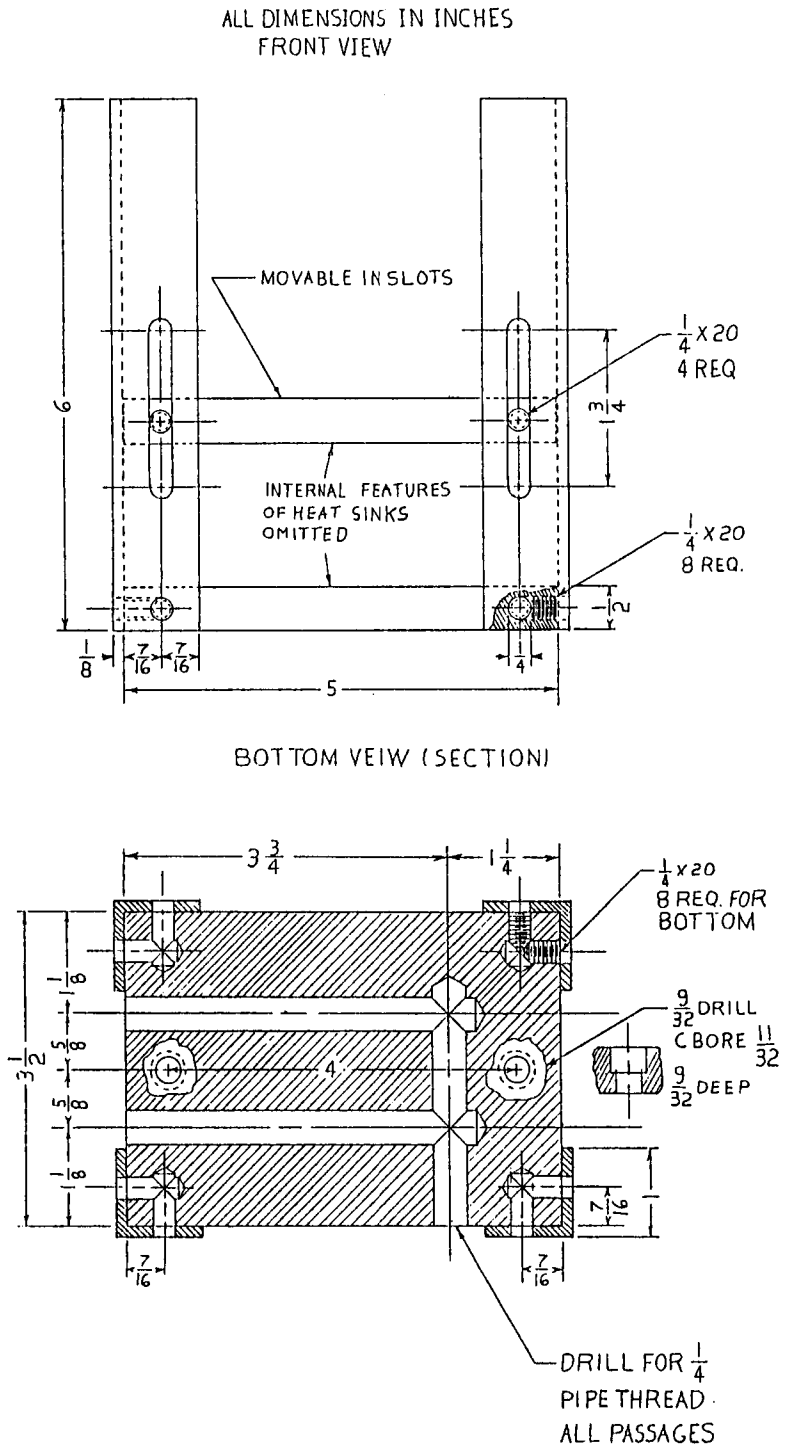


Figure III-3. Scale drawing of cuvette assembly.

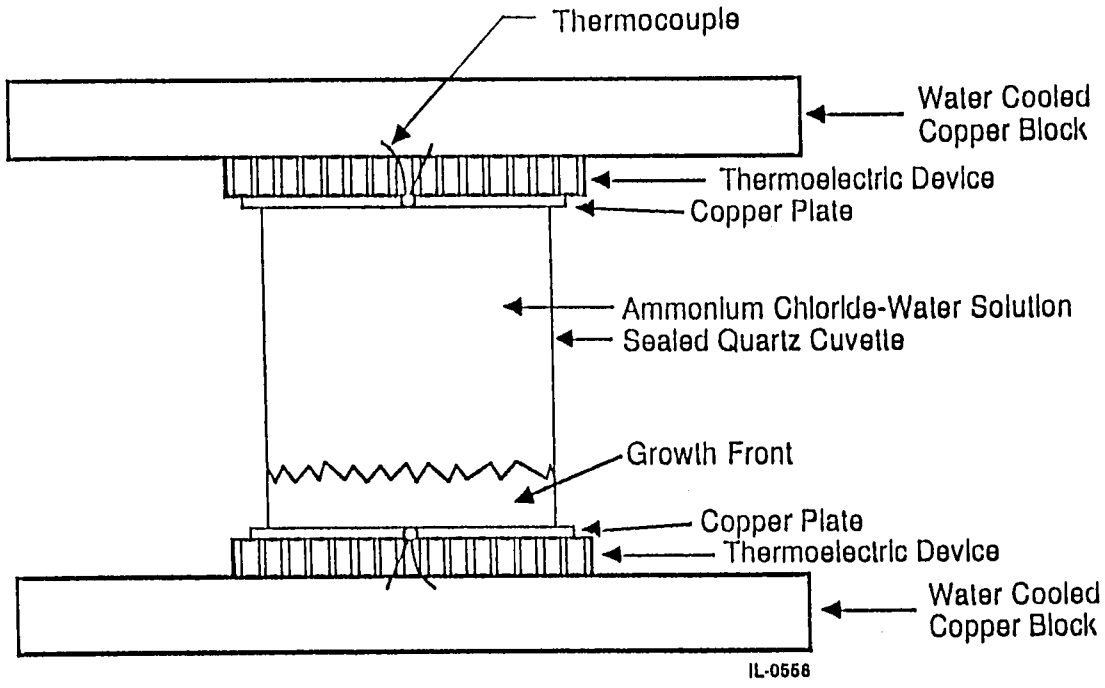


Figure III-4. Schematic of cuvette solidification assembly.

corner and had holes for mounting to a lab jack. The top heat sink is mounted in slots so that it can accommodate different cuvettes (Figure III-3). The Thermoelectric devices were attached to the heat sinks with thermal grease and held in place by the compression of the cuvette in the assembly. This provided good thermal contact with the heat sinks and also allowed easy replacement of the cuvette. A copper plate that had a slot for a thermocouple was placed between the ends of the cuvette and the TEDs. This plate was also attached to the TED with thermal grease (Figure III-4).

Optical System

The optical system had two independent subsystems powered by an etalon stabilized argon ion laser (Figure III-5). The first subsystem was a confocal imaging system with a central dot (high pass) filter, which was used to monitor the solute rich inverted density layer. The second subsystem was a particle side scattering system that used a sheet beam of light to illuminate the motion of small tracer particles. A variable beam splitter divided the laser beam between the two systems. The beam going to the confocal system was about 4% of the main beam; the other 96% went to the side scattering system. The main beam power was about 0.4 watts. Figure III-6 gives the various part numbers.

The first element in the confocal system was a spatial filter and beam expander. The expanded and collimated beam then passed through the sample to a 45 degree angle pellicle beam splitter. The next element was the first of two 400 mm focal length acromat lenses (the transform lens) which was located 400 mm from the sample. The 25 micron dot filter was located 400 mm behind this lens and 400mm behind the dot was the second (inverse transform) lens.

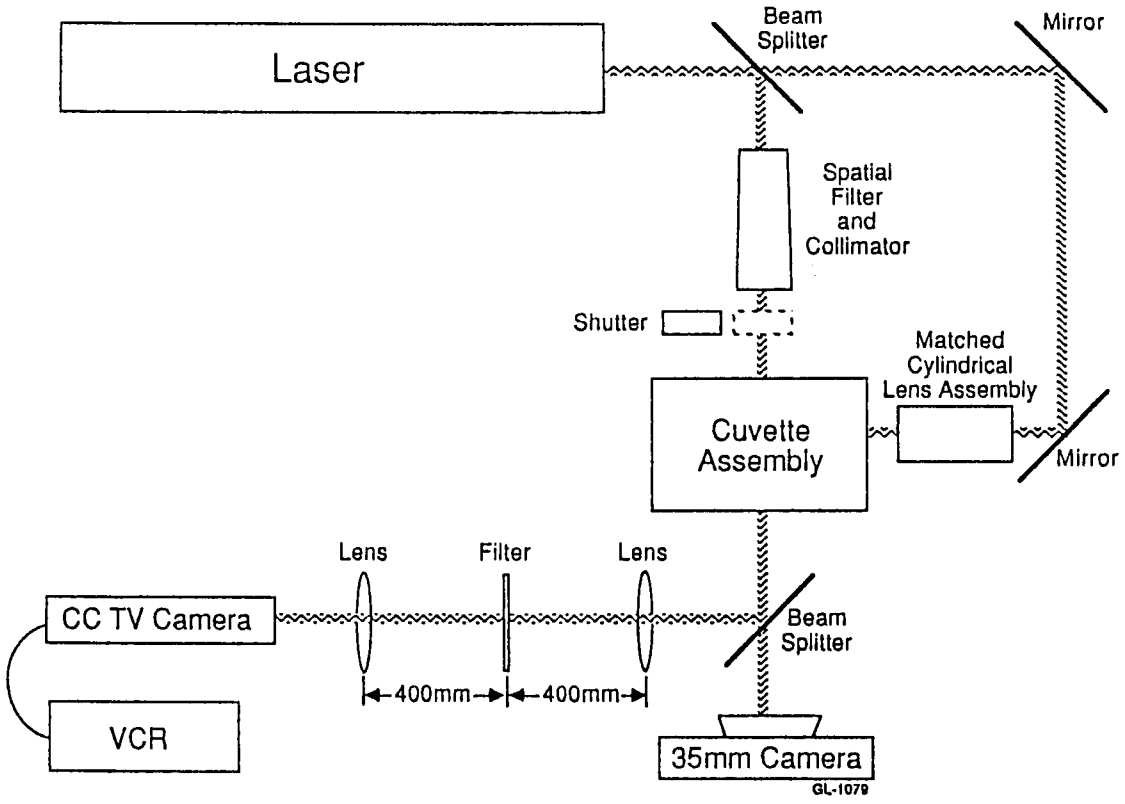


Figure III-5. Schematic of optical system.

OPTICAL SYSTEM PARTS LIST

I. OVERALL SYSTEM

A. Laser - Lexel model 95 Argon Ion

B. Variable beam splitter - Jodon model VBA-200

II. CONFOCAL OPTICAL SYSTEM

A. Beam Expander Assembly

1. Spatial filter and beam expander mount - Moore and Write X-Z translator with adapter rings.
2. Spatial Filter - Spectra Physics model 332 with 6.8 micron filter.
3. Beam Expanding Lens - Spectra Physics model 336.

B. Electric Shutter - Frabricated from 24V-DC solinoid.

C. Cuvette Mounting Assembly

1. Cuvette assembly (Figure III-3).
2. 6 inch lab jack - Newport model 270.
3. X-Y translation stage - Newport model 400.
4. Magnetic instrument base - Newport model 200.

D. Pellicle Beam Splitter Assembly

1. 2 inch pellicle beam splitter and holder - Newport model PBS-2.
2. Post mount - Newport model VPH-3.
3. Base plate - Newport model B-2.
4. Rotation and tilt stage - Newport model 36.
5. Translation stage - Newport model 440.

E. Lens Assembly (two 400mm acromats).

Figure III-6. Optical system parts list.

1. Ring mounts - Newport model AC-2.
2. Post mounts - Newport model VPH-4.

F. Video Camera Assembly

1. Video camera - Hitachi CCTV model HV-17TU.
2. Filter holder - Newport model FH-1.
3. Neutral density filter - Newport model FS-3.
4. Camera support - Newport optical rail model URL-18.
5. 6 inch lab jack - Newport model 270

G. Dot Filter Assembly

1. Dot filter - Microscope slide with 25 micron dot
2. Microscope slide mount - Newport model MM-2A
3. Vertical translator - Oriel model 1478
4. Two single axis translators - Newport model 440

III. PARTICLE TRACKER SYSTEM

A. Mirror Assembly (two mirrors)

1. Mirrors - 2 inch diameter first surface.
2. Mirror mounts - Newport model 625.

B. Cylindrical Lens Assembly

1. Cylindrical Lens Unit - Jodon model unknown.
2. Mount - Newport model 600A-2.
3. Adapter ring - Newport model A-2-1.
4. 6 inch lab jack - Newport model 270.

C. Lens Assembly (109 mm acromat)

Figure III-6. (continued)

1. Ring mount - Newport model AC-2.
2. Post mount - Newport model VPH-4.

D. 35 mm Cammera Assembly

1. 35 mm camera - Nikon model F3-HP.
2. Motor drive - Nikon model MD-4.
3. 250 exposure magazine back - Nikon model MF-4.
4. Data back - Nikon model MF-17.
5. Bellow focusing attachment - Nikon model PB-6.
6. Zoom lens - Nikon series E 70-210mm f/4.
7. DC power supply - Nikon model MA-4.
8. 6 inch lab jack - Newport model 270.

Figure III-6. (continued)

A video camera was 400 mm behind the second lens (Figure III-5). The output from the video camera was recorded by a VHS format video recorder.

The side scattering system consisted of two first surface mirrors, a cylindrical lens unit which produced a fan beam, and a 109 mm focal length acromat lens to collimate and focus the fan beam. The recording system was a 35mm Nikon with a remotely triggered motor drive. The lens system consisted of a focusing belows with a 80 - 200mm Nikor zoom lens. This arrangement allowed room for the beam splitter between the sample and the lens while still providing sufficient magnification of the sample (Figure III-5).

The cuvette assembly was secured to the table with a 6 inch magnetic base which had a 6 inch dual axis translator and a 6 inch lab jack on top. Fiqure III-5 gives the overall optical system layout.

IV. EXPERIMENTAL PROCEDURES

Two solutions were prepared in 4 oz polyethylene bottles. The first contained 28 $\pm$.05wt% NH_4Cl while the second contained 28 $\pm$.05wt% NH_4Cl solution with 0.5 grams of tracer particles. Deionized water with a specific resistance of greater than 18×10^6 ohms was the solvent. Ammonium chloride (reagent grade from Fisher Scientific Company) was the solute. The tracer particles were small hollow butane filled plexiglass spheres that ranged in size from 10-25 microns and density from 1.1 to 1.2 g/cm^3. The particles were small enough to follow the small magnitude convective flows and were almost neutrally buoyant in the 28wt% NH_4Cl solution.

The sample container was a $28 \times 20 \times 12$mm quartz cuvette with two mm thick walls at all surfaces except the top 20×12 mm surface. This top surface was one mm thick with a one mm diameter hole in the center for filling (Figure IV-1). The cuvette was first filled through the small hole in the top of the cuvette with the plain NH_4Cl solution at a temperature of 50°C, which was above the maximum average temperature of the solution during the experiment. Once the cuvette was filled and all the air removed, about one cm^3 of the particle solution was used to replace some of the solution already in the cuvette. This method of using two solutions made it easy to vary the number of particles in the experiment sample by changing the amount of the particle solution added to the cuvette. The cuvette was then sealed with a piece of electrical tape that covered the entire top surface. The tape did not contaminate the solution during short term experiments, provided a non-permanent sealing technique, and also served as a safety valve, in case of over-pressure.

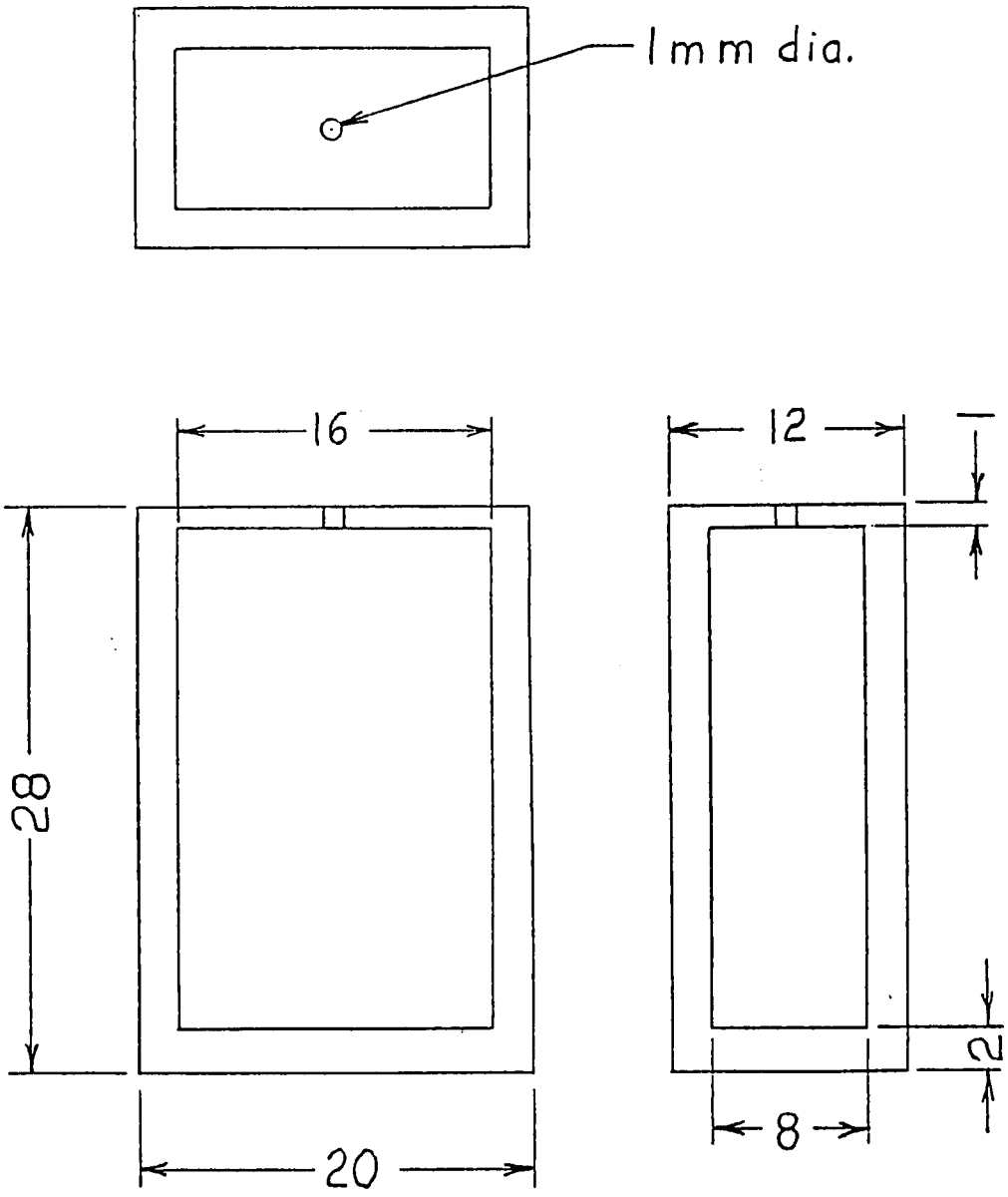


Figure IV-1. Scale drawing of cuvette (all dimensions in mm).

The NH_4Cl solution was solidified at five different cooling rates (CR) of 0.3, 0.5, 1.0, 2.0, and 3.0°C/min and two gradients (G) of 15 and 28°C/cm. The different cooling rates were used to illustrate the growth rate dependence of the convective instability while the gradients illustrated the temperature gradient dependence.

Two types of data were taken during the experiment. The confocal optical system data was video recorded. The particle tracking data was obtained by taking an eight second time exposure photograph of the particles illuminated by the sheet beam. During the time exposure, the confocal system was blocked by a shutter to prevent the collimated beam from entering the 35mm camera (Figure III-5). The blank left on the video tape served as a time indicator. The time exposures were made at 30 second intervals (before breakdown) and 15 seconds intervals (after breakdown), leaving five seconds of confocal data between exposures. The camera and shutter were controlled by the temperature control program which also recorded the time and number of each exposure. The video recorder was turned on immediately prior to the start of the experiment and initiation of cooling was marked by the first shutter closing.

Prior to temperature control system activation the sample was removed from the cuvette assembly, shaken to suspend and mix the tracer particles, and reinstalled in the assembly. Then the cuvette was heated from the top and bottom at 40°C for 10 minutes to melt back and smooth the interface of the mushy-zone. Upon completion of this phase, a positive temperature gradient was imposed on the sample. The bottom temperature was maintained 1°C to 4°C below the saturation temperature of the solution. The top temperature is dictated by the desired temperature gradient, either 15°C/cm or 28°C/cm. Once the temperature gradient was imposed the sample was allowed to equilibrate

for several hours, continuing to thin and smooth the interface. Upon complete stabilization of the interface and temperature gradient, the experiment (cooling) was initiated.

At control system start up, the experiment parameters such as temperature gradient, cooling rate, preheat temperature, preheat hold duration, temperature hold duration, and starting temperatures were entered into the computer. The 35mm camera exposure times were preprogrammed at 30 second intervals; the exposure interval could be changed on demand to 15 seconds (during breakdown) and back to 30 seconds (after breakdown). Once the parameters were entered into the computer, the program was executed and the TED power supplies started. Once the control system was in operation, the planned preheat and temperature holds could be over-ridden if desired. Solidification of the sample was then obtained by lowering the top and bottom TED temperatures simultaneously and at a constant rate as dictated by the control program input parameters. All data concerning the experiment were stored in a data file. These data included the user specified parameters described above as well as the temperature. The temperature data was recorded at a user specified interval usually ranging from 2 to 60 seconds. The main purpose of this data was to evaluate the control system performance and provide a permanent record of the experiment.

V. DATA REDUCTION

The data from the confocal system was concerned with the time dependence of the height and thickness of a dark horizontal band that formed in front of the growth interface during solidification. This band is called the null layer and is caused by a change of direction of the density profile. The confocal optical system data was reduced using a Vicom image processing computer. This was accomplished by digitizing a selected image from the video tape into a 512×512 pixel array. The pixel size was calibrated using gage marks on the cuvette. A hand controlled cursor was then used to count the number of pixels above a datum location at the inside bottom of the cuvette. Measurements of null height (from the bottom of the cuvette to the center of the null) and null thickness were made for the confocal data; Figure V-1 is a sample photograph indicating how the measurements were made.

The particles illuminated by the particle tracker system demonstrated circular flow patterns (Figure V-2) which hereafter will be referred to as vortices. The particle tracker data is concerned with the time dependence of the vortex dimensions and height, as well as the wavelength of the vortical system. These measurements included the height of the vortex center and top from the inside bottom of the cuvette and the horizontal and vertical dimensions of the vortices, which are used to calculate an aspect ratio, the vertical dimension divided by the horizontal dimension of the vortex. The wavelength of the vortices was found by measuring the width of the longest string of continuous vortices and dividing that length by the number of vortices. The data was taken either directly from photographs or from the beam of a photographic enlarger.

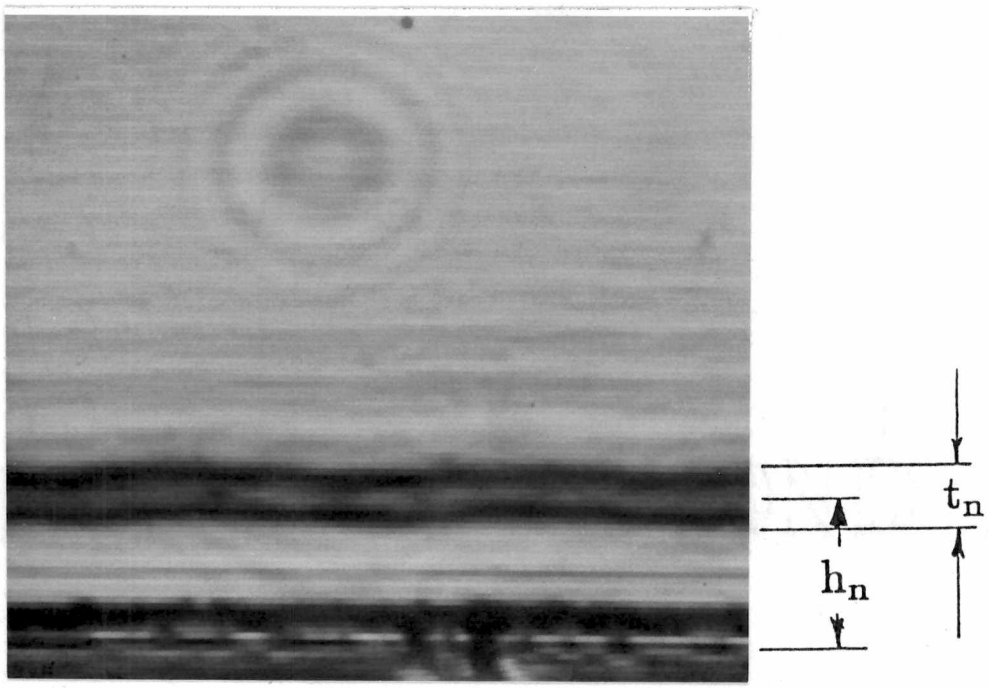


Figure V-1. Sample photograph of confocal optical system data.

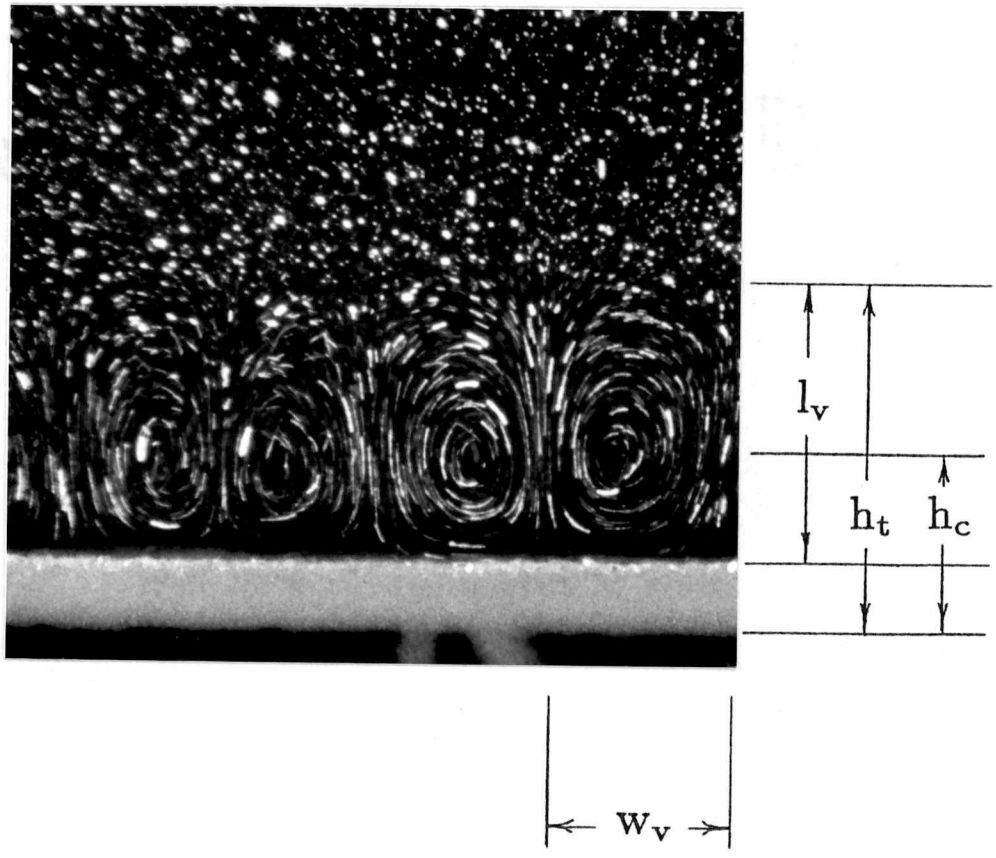


Figure V-2. Sample photograph of particle tracker data.

These measurements are illustrated in the sample photograph shown in Figure V-2. The most uniform and consistent vortices were selected for measurement.

Photographs were made of the confocal data from the video tape immediately prior to and just after the particle track time exposure. The confocal photographs were scaled so that they matched the scale of prints from the particle track time exposure. This was done by matching the gage marks on the cuvette. All prints of the confocal data were then made at this magnification. Having matched scales allowed direct comparison of the density distribution shown by the confocal system with the fluid motion illuminated by the particle tracker system.

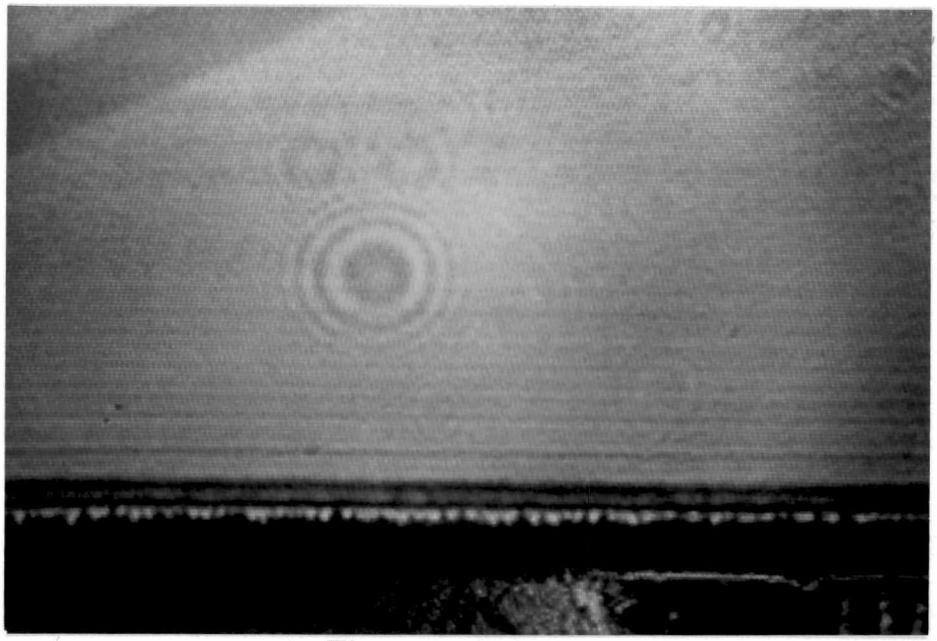
VI. RESULTS AND DISCUSSION

The discussion will be divided into four categories, cooling rate effects, temperature gradient effects, null layer behavior, and vortex geometry. The cooling rate effects section will discuss the dependence of breakdown time and vortex rise rates on fluid heat transfer. The temperature gradient effects section discusses the dependence of breakdown time and vortex rise rate on temperature gradient. The null layer behavior section describes the change in height and thickness of the the null layer before, during and after breakdown. The section also discusses the relationship between the vortex rise rate and the movement of the null layer after breakdown. The vortex geometry section describes the type of convection that was discovered by observing the tracer particles.

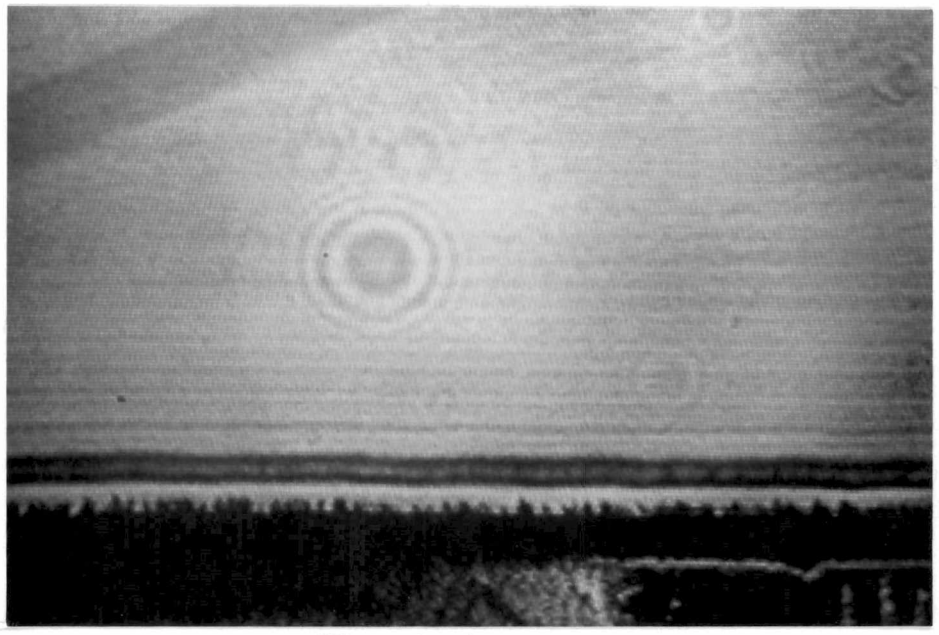
A sequence of photographs illustrating the behavior of the null layer is given in Figures VI-1 and VI-2 for times before, during, and after breakdown. A sequence of photographs illustrating the motion of the tracer particles during and after breakdown is given in Figures VI-3 and VI-4. The behavior of both types of data and the relationship between them is discussed in detail in the following sections.

Cooling Rate Effects

The effects of cooling rate can be seen in both the confocal system (null layer) data and the particle tracker system data. In graphs of null height and thickness versus time (Figures VI-5 to VI-14), breakdown of the inverted layer as shown by null layer undulation is observed to occur sooner for higher cooling rates. In plots of vortex top and center height versus time (Figures VI-15 to VI-18), convection as indicated by the onset of particle motion was observed to occur

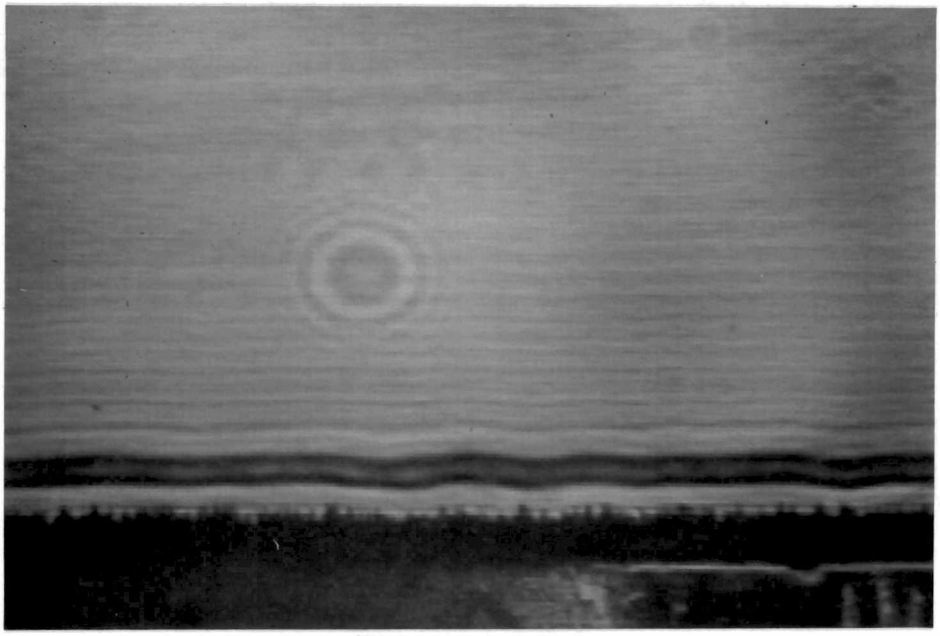


Time: 1 min 30 sec
before breakdown

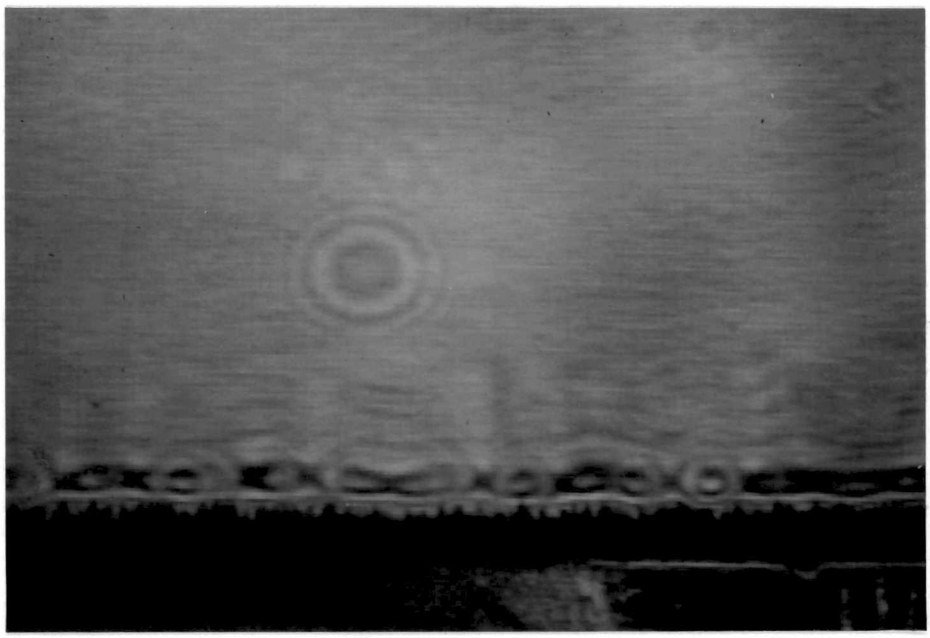


Time: 2 min 10 sec
beginning of breakdown

Figure VI-1. Photograph sequence of confocal system data for 1.0°C/min cooling rate and 15°C/cm temperature gradient and magnification 10.4.

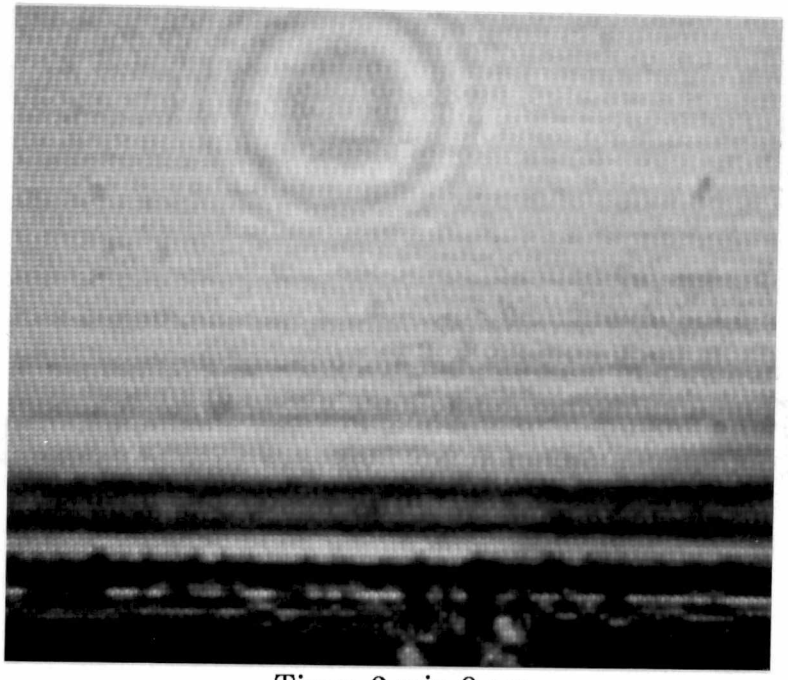


Time: 2 min 30 sec

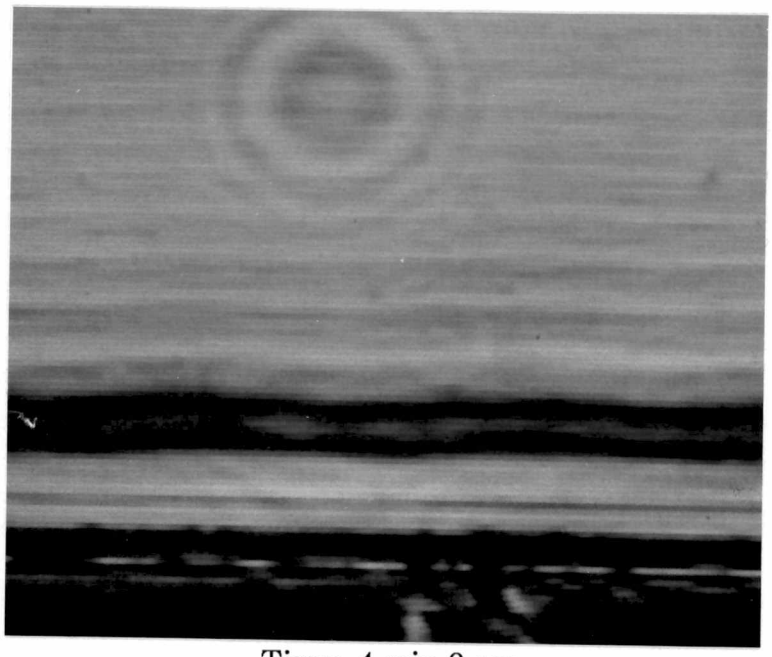


Time: 3 min 0 sec
after breakdown

Figure VI-1 (continued)

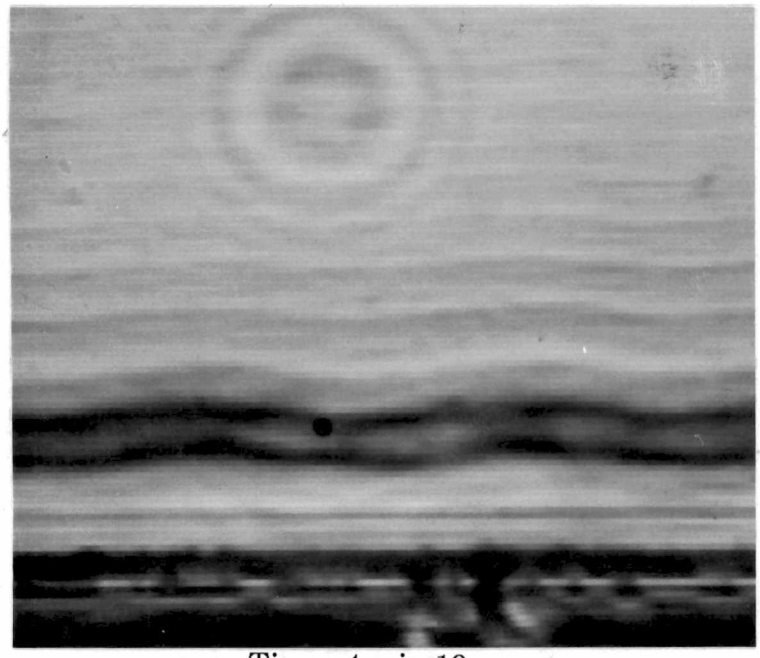


Time: 2 min 0 sec
before breakdown

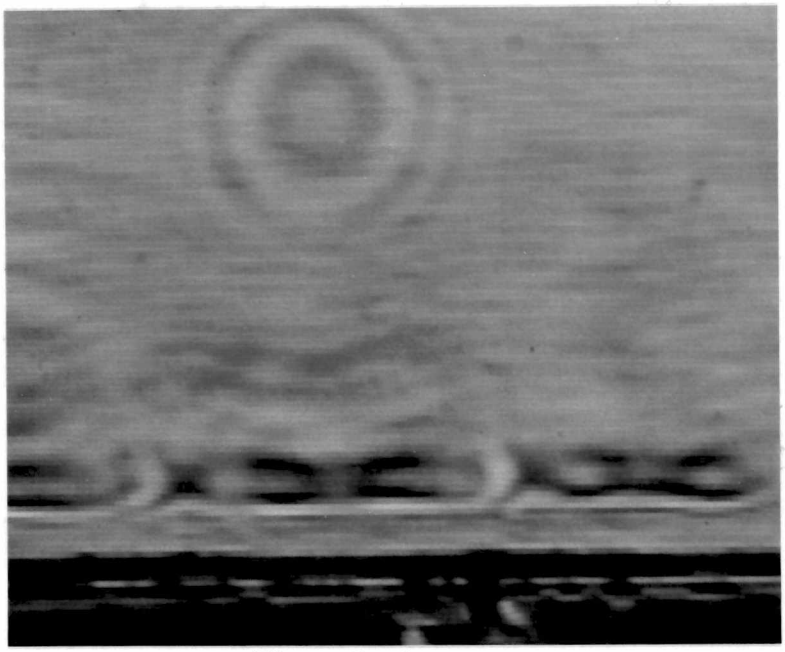


Time: 4 min 0 sec
beginning of breakdown

Figure VI-2. Photograph sequence of confocal system data for 0.5°C/min cooling rate and 15°C/cm temperature gradient and magnification 19.8.

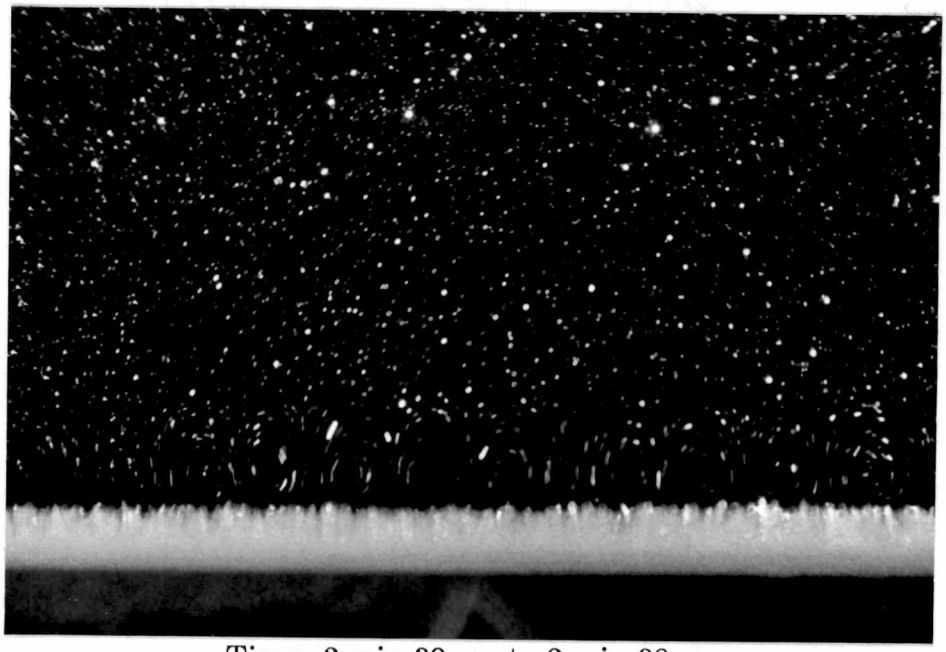


Time: 4 min 10 sec

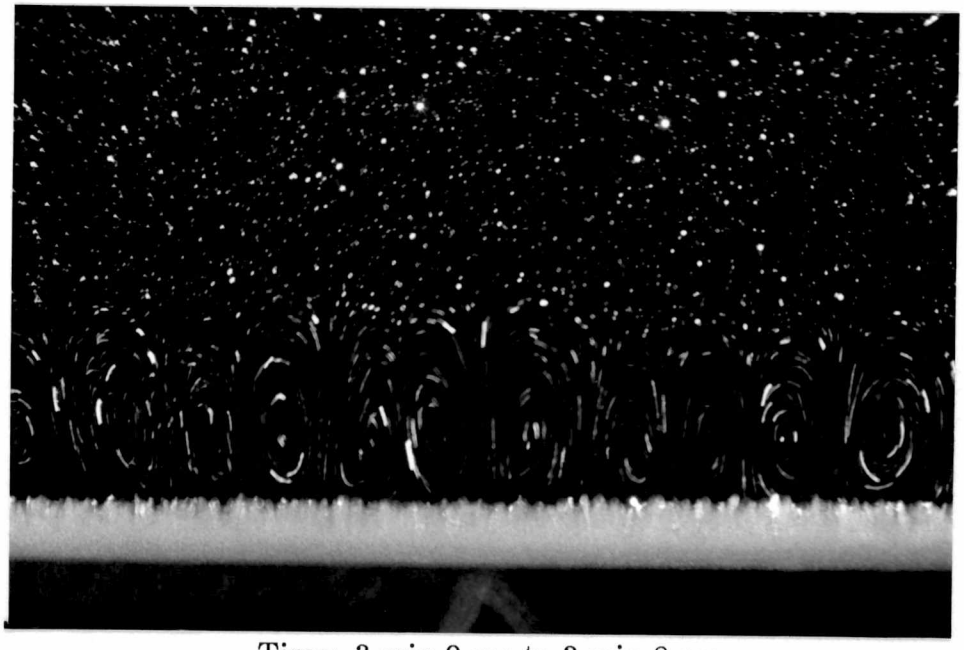


Time: 5 min 0 sec
after breakdown

Figure VI-2 (continued)

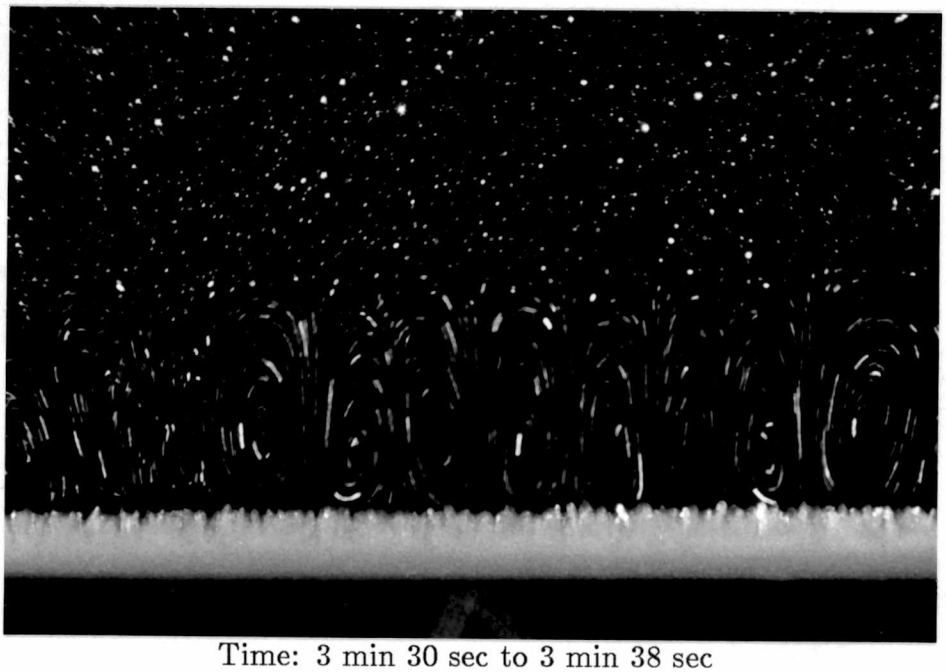


Time: 2 min 30 sec to 2 min 38 sec
beginning of breakdown

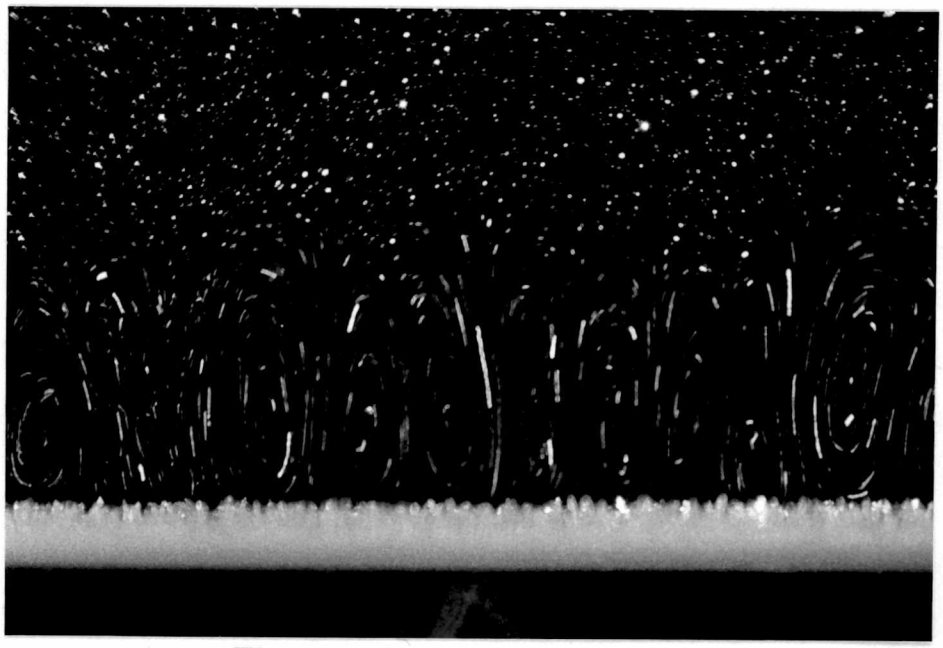


Time: 3 min 0 sec to 3 min 8 sec

Figure VI-3. Photograph sequence of particle tracker data for 1.0°C/min cooling rate and 15°C/cm temperature gradient and magnification 10.4.

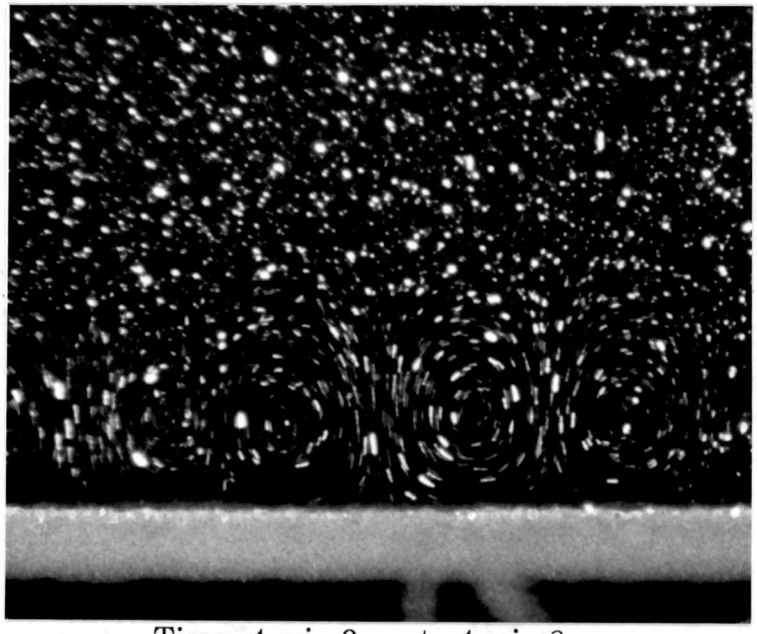


Time: 3 min 30 sec to 3 min 38 sec
after breakdown

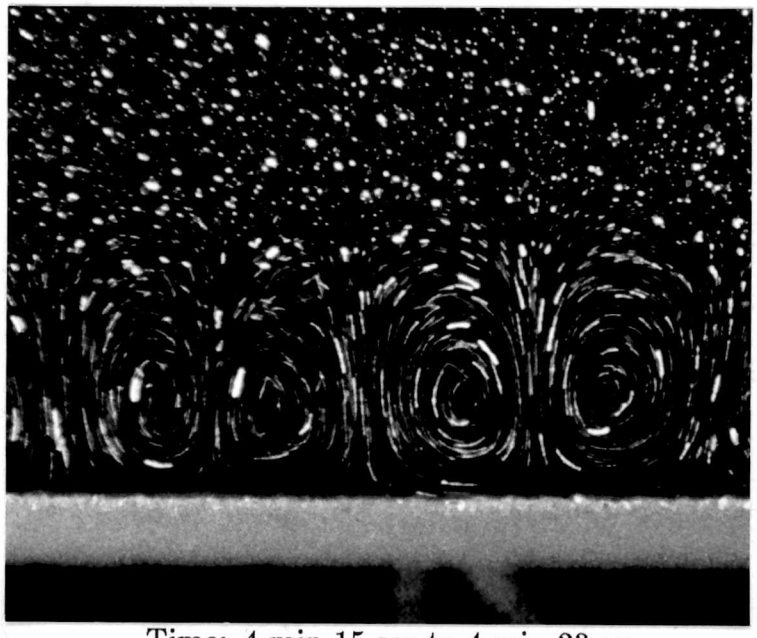


Time: 4 min 0 sec to 4 min 8 sec

Figure VI-3. (continued)

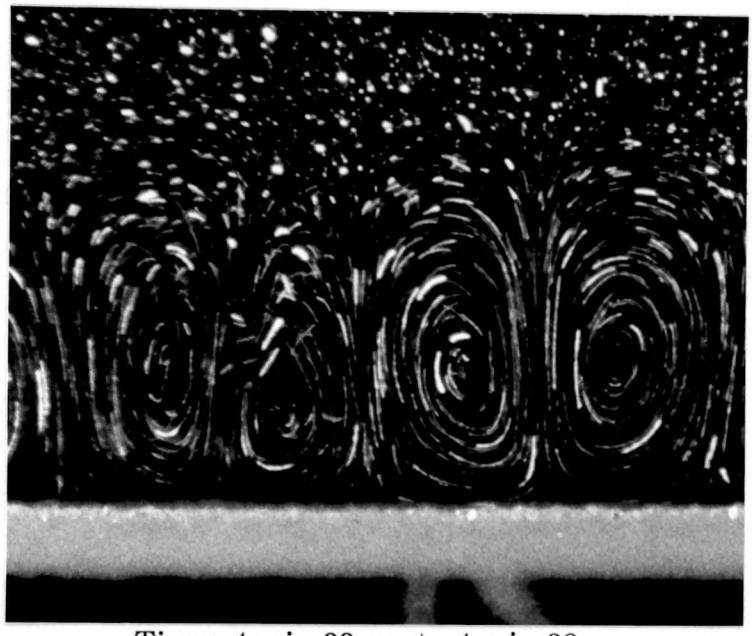


Time: 4 min 0 sec to 4 min 8 sec
beginning of breakdown

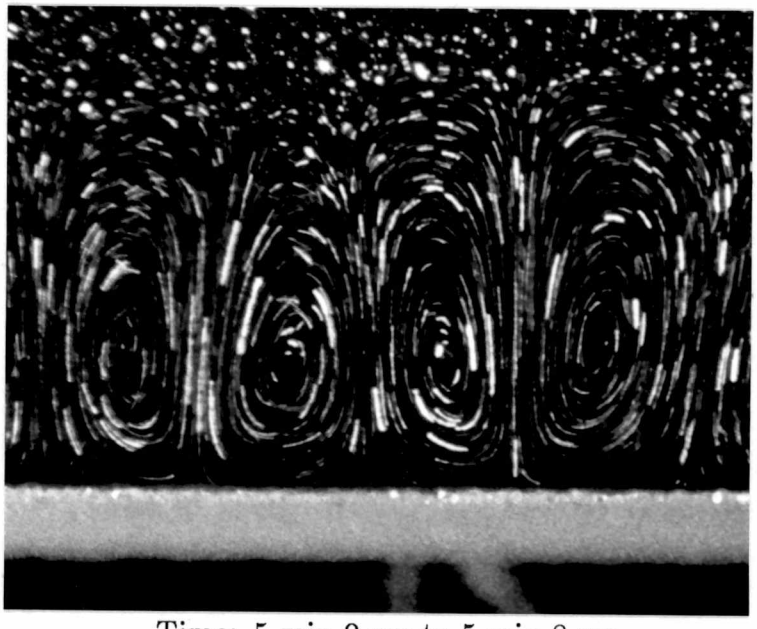


Time: 4 min 15 sec to 4 min 23 sec

Figure VI-4. Photograph sequence of particle tracker data for 0.5°C/min cooling rate and 15°C/cm temperature gradient and magnification 19.8.



Time: 4 min 30 sec to 4 min 38 sec



Time: 5 min 0 sec to 5 min 8 sec

Figure VI-4. (continued)

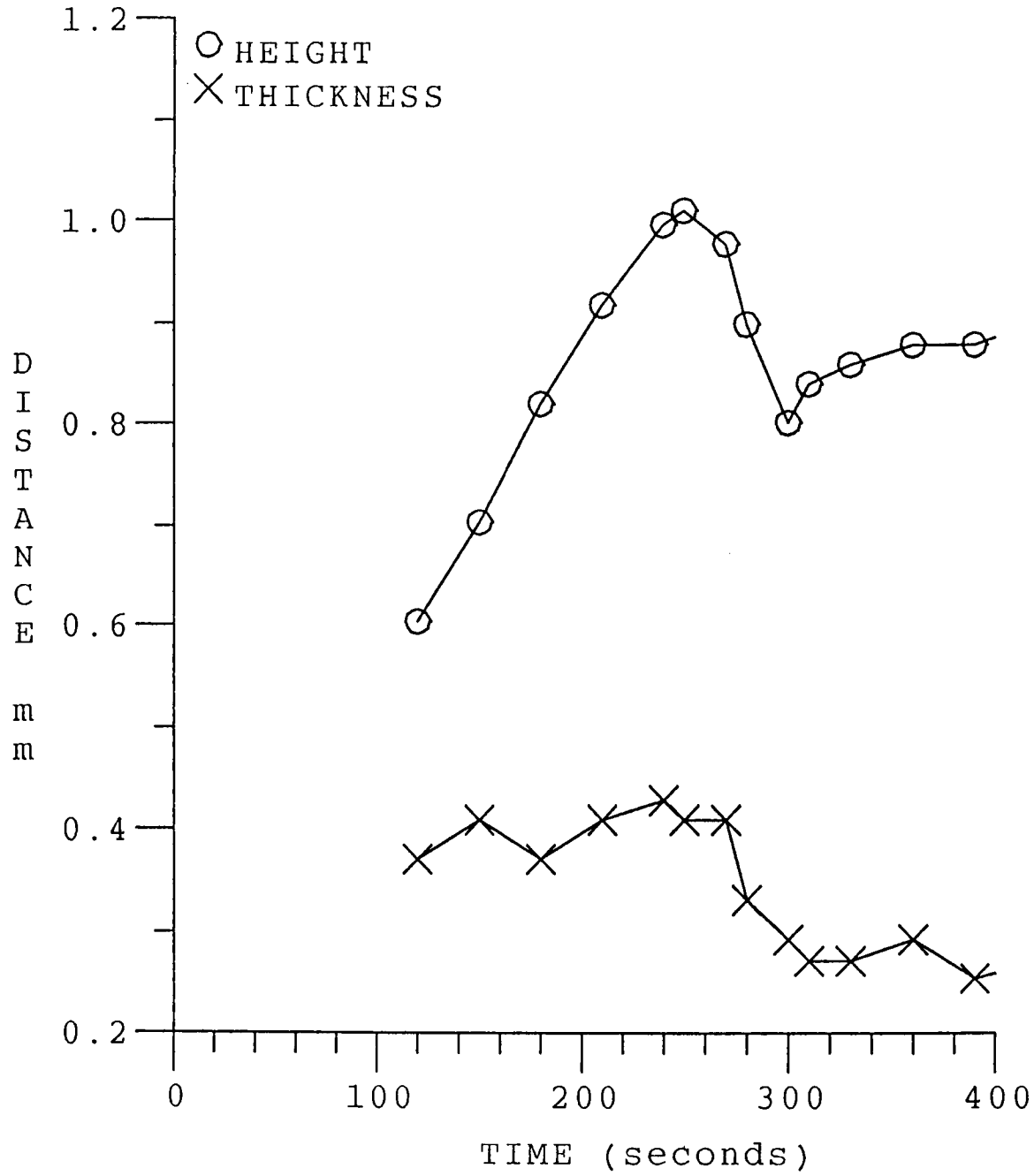


Figure VI-5. Null height (h_n)and thickness (t_n) as a function of time for 0.3°C/min cooling rate and 15°C/cm temperature gradient.

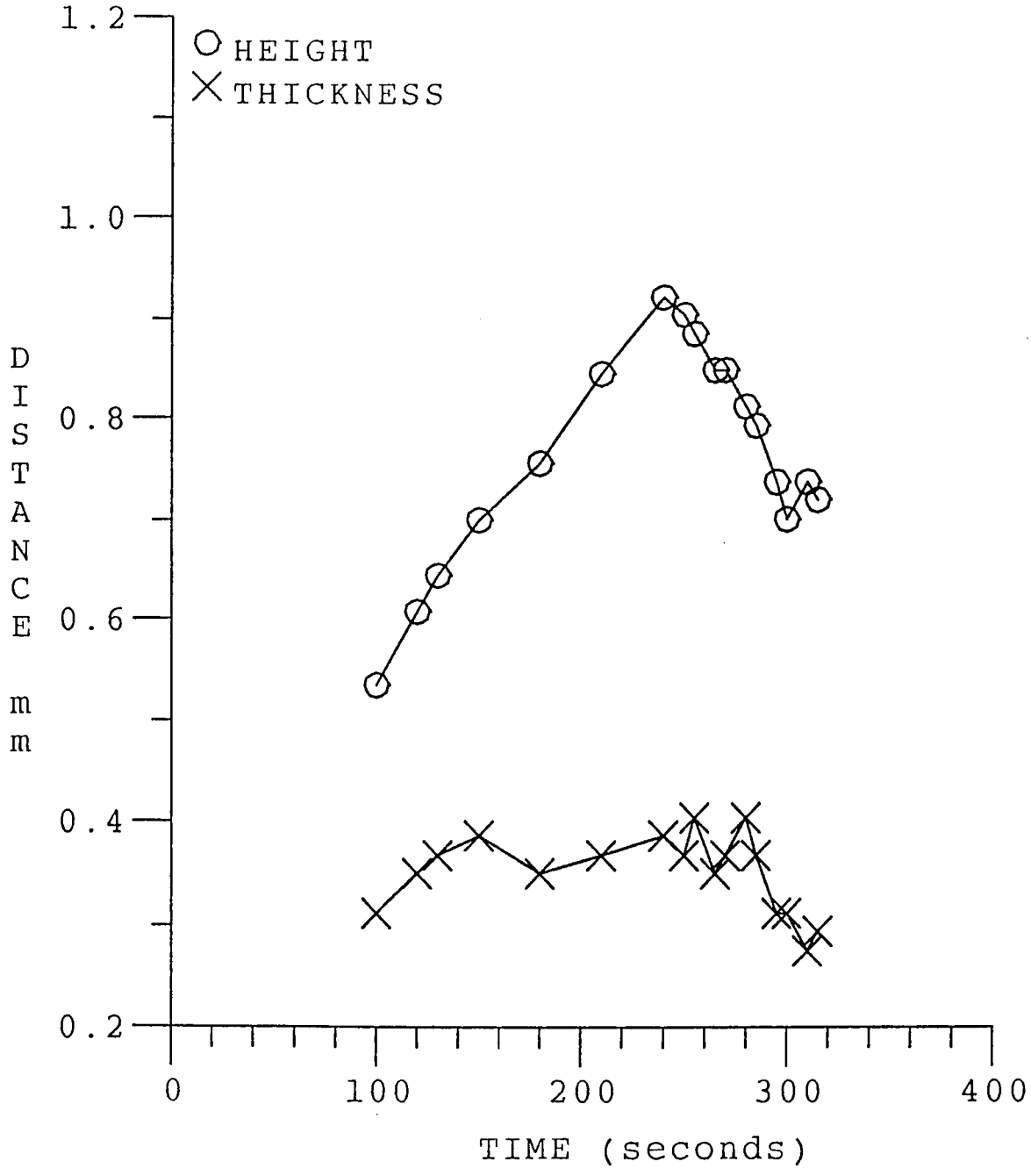


Figure VI-6. Null height (h_n) and thickness (t_n) as a function of time for 0.5°C/min cooling rate and 15°C/cm temperature gradient.

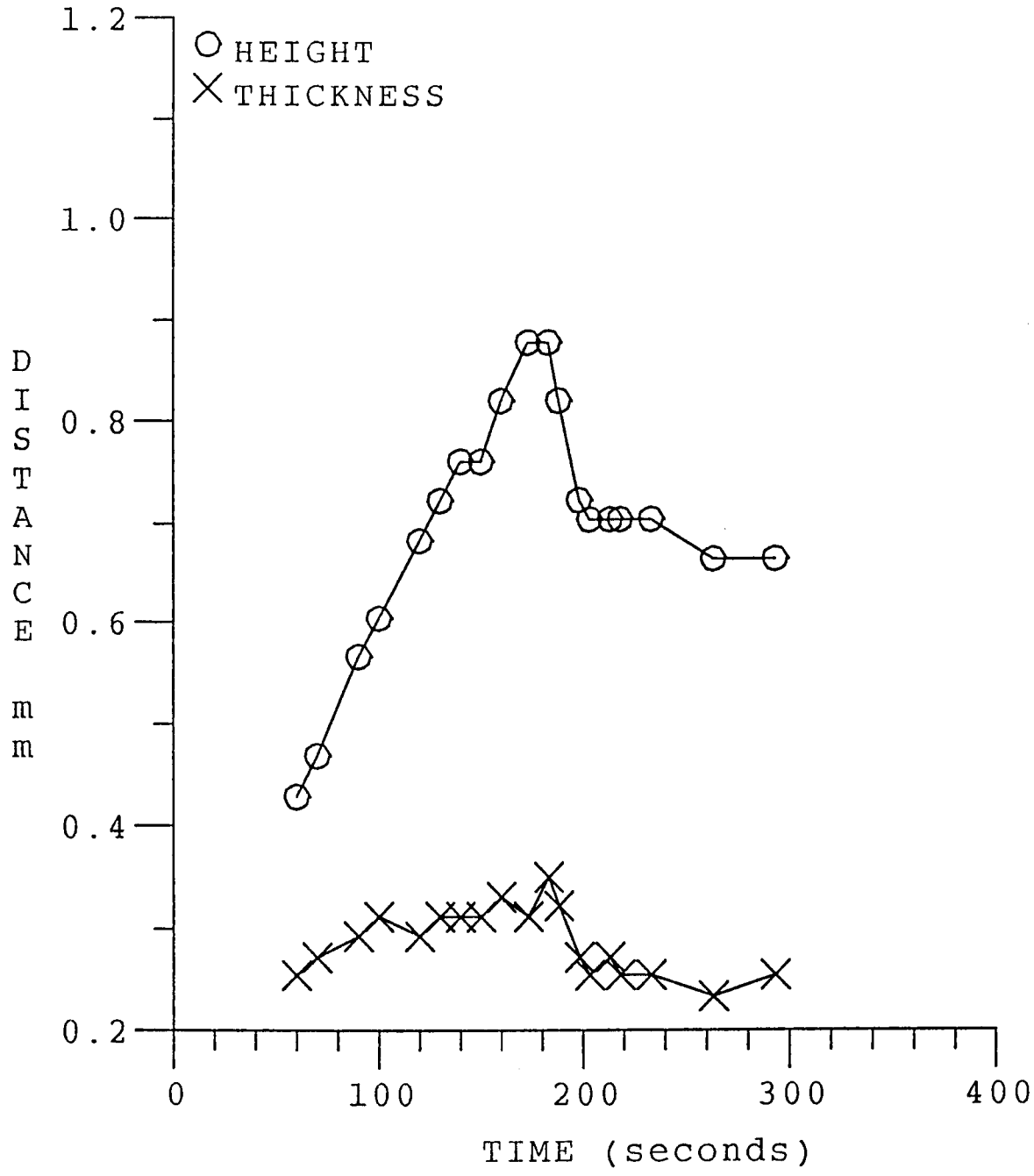


Figure VI-7. Null height (h_n) and thickness (t_n) as a function of time for 1.0°C/min cooling rate and 15°C/cm temperature gradient.

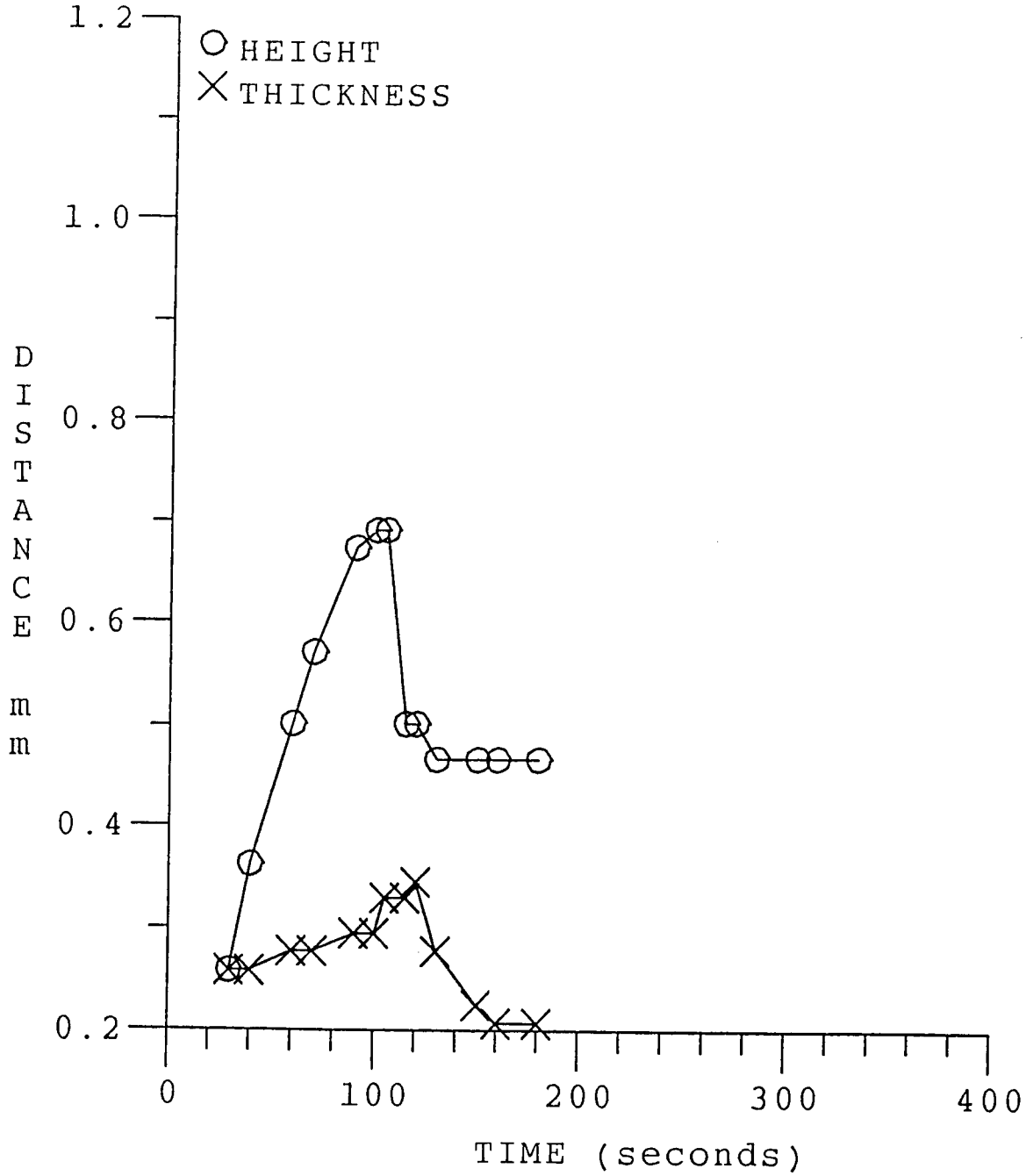


Figure VI-8. Null height (h_n) and thickness (t_n) as a function of time for 2.0°C/min cooling rate and 15°C/cm temperature gradient.

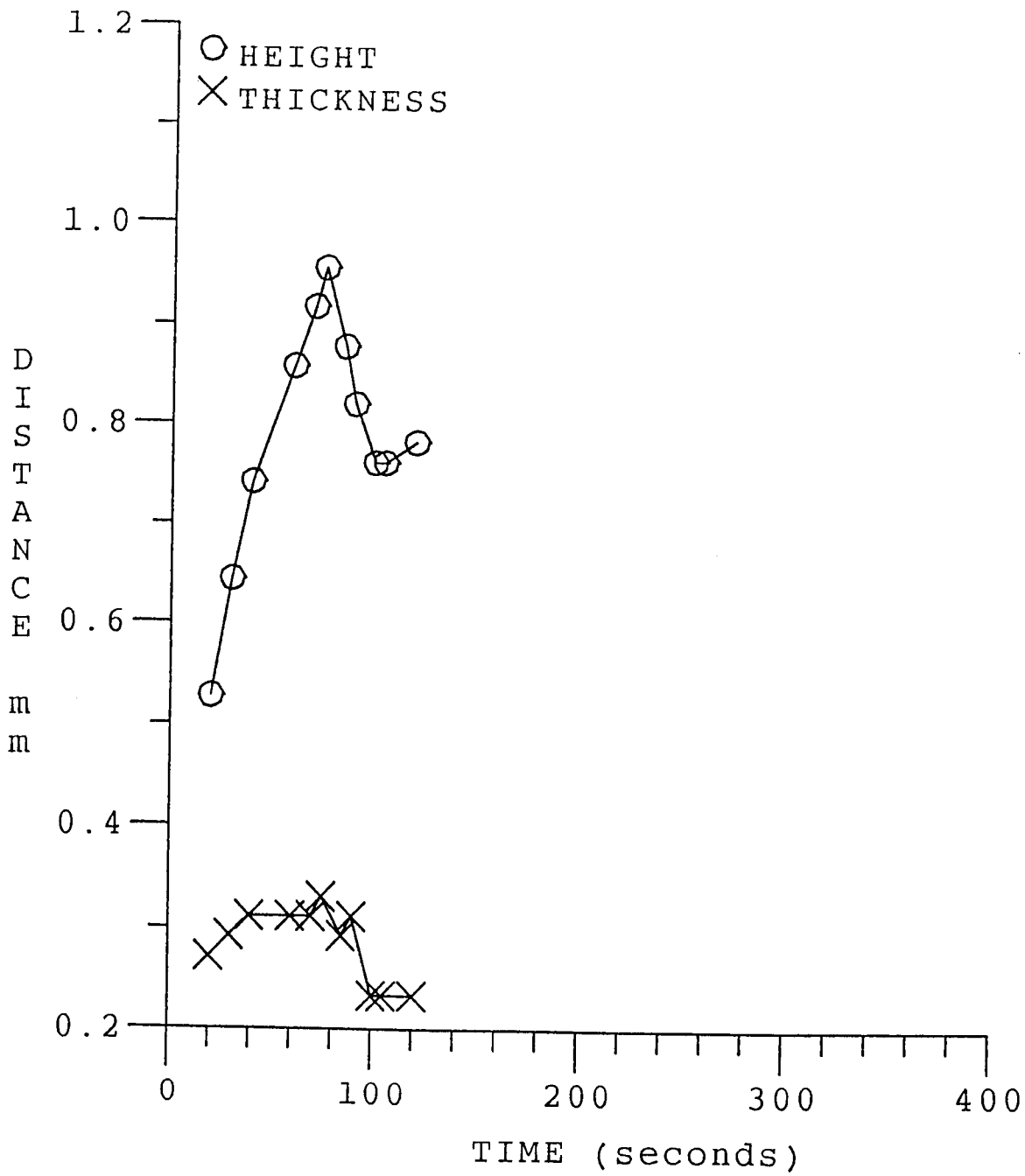


Figure VI-9. Null height (h_n) and thickness (t_n) as a function of time for 3.0°C/min cooling rate and 15°C/cm temperature gradient.

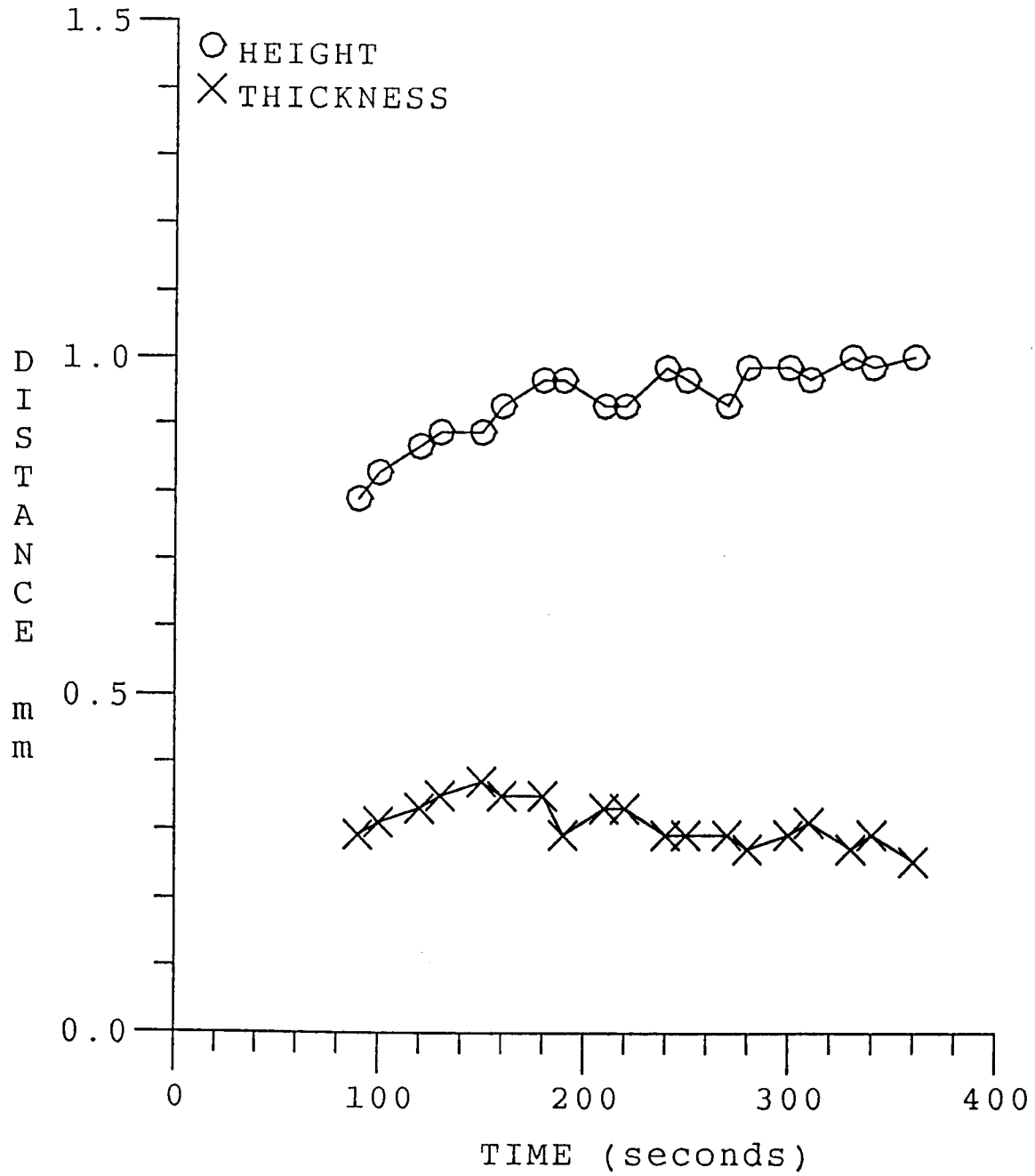


Figure VI-10. Null height (h_n) and thickness (t_n) as a function of time for 0.3°C/min cooling rate and 28°C/cm temperature gradient.

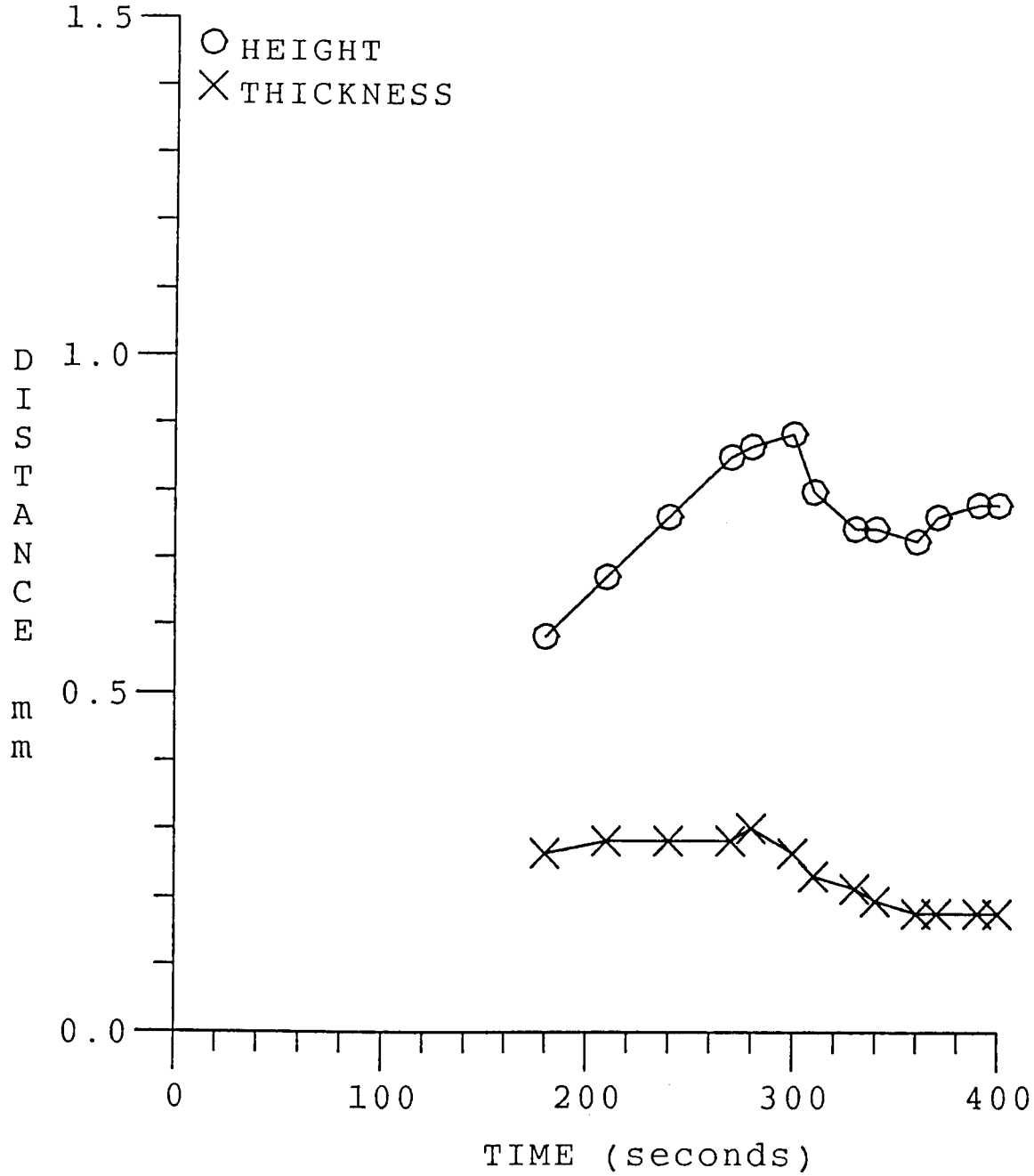


Figure VI-11. Null height (h_n) and thickness (t_n) as a function of time for 0.5°C/min cooling rate and 28°C/cm temperature gradient.

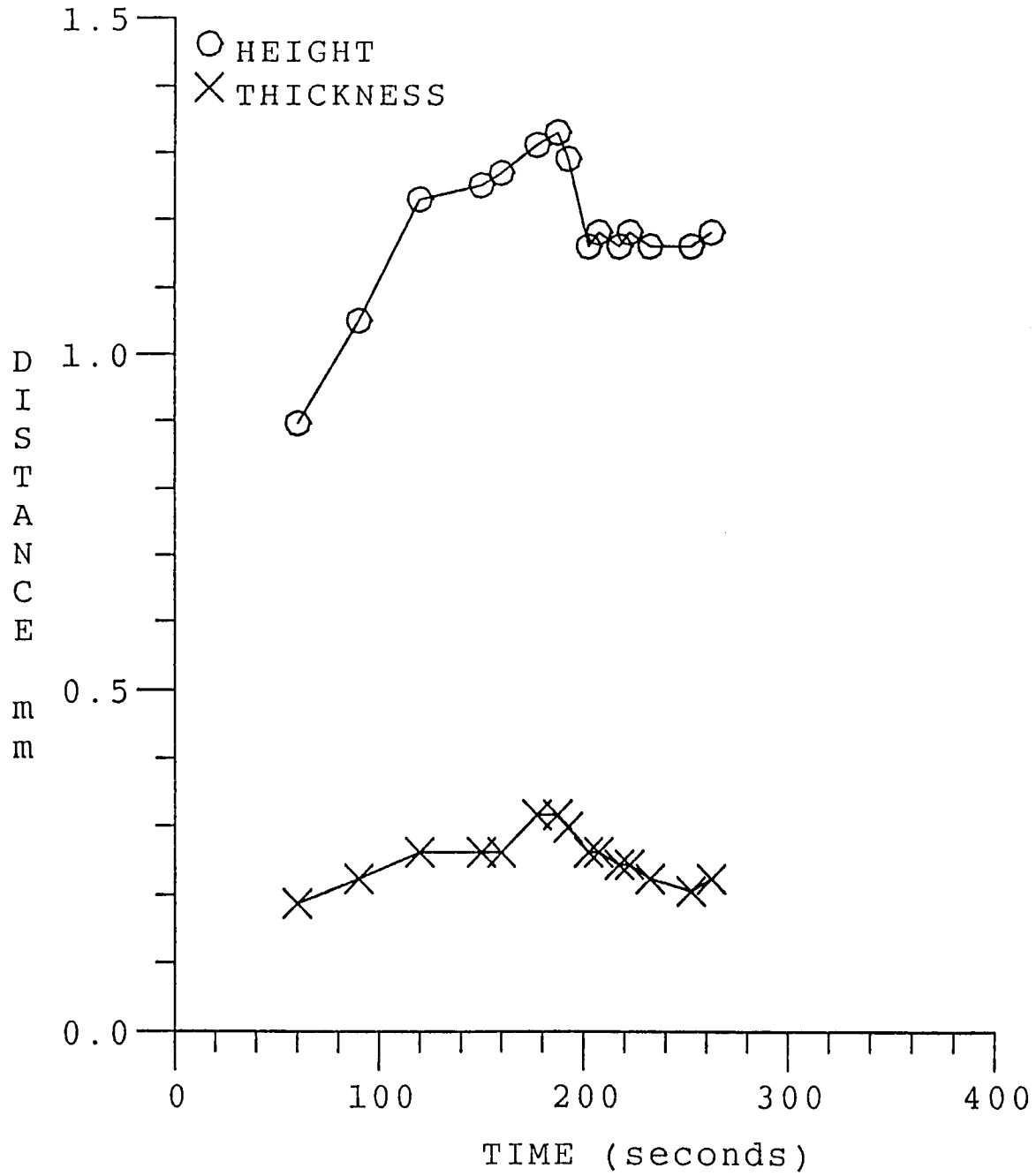


Figure VI-12. Null height (h_n) and thickness (t_n) as a function of time for 1.0°C/min cooling rate and 28°C/cm temperature gradient.

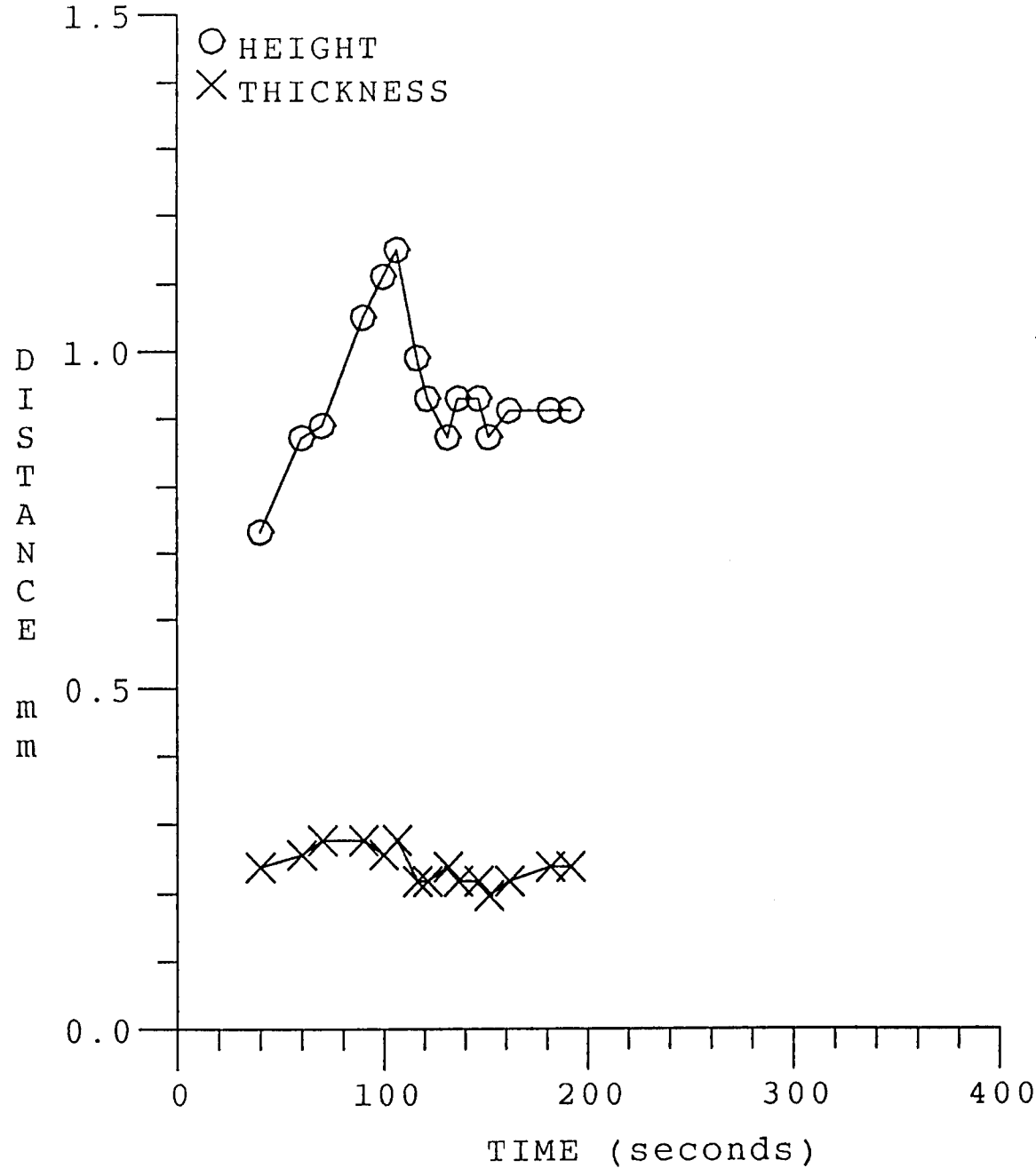


Figure VI-13. Null height (h_n) and thickness (t_n) as a function of time for 2.0°C/min cooling rate and 28°C/cm temperature gradient.

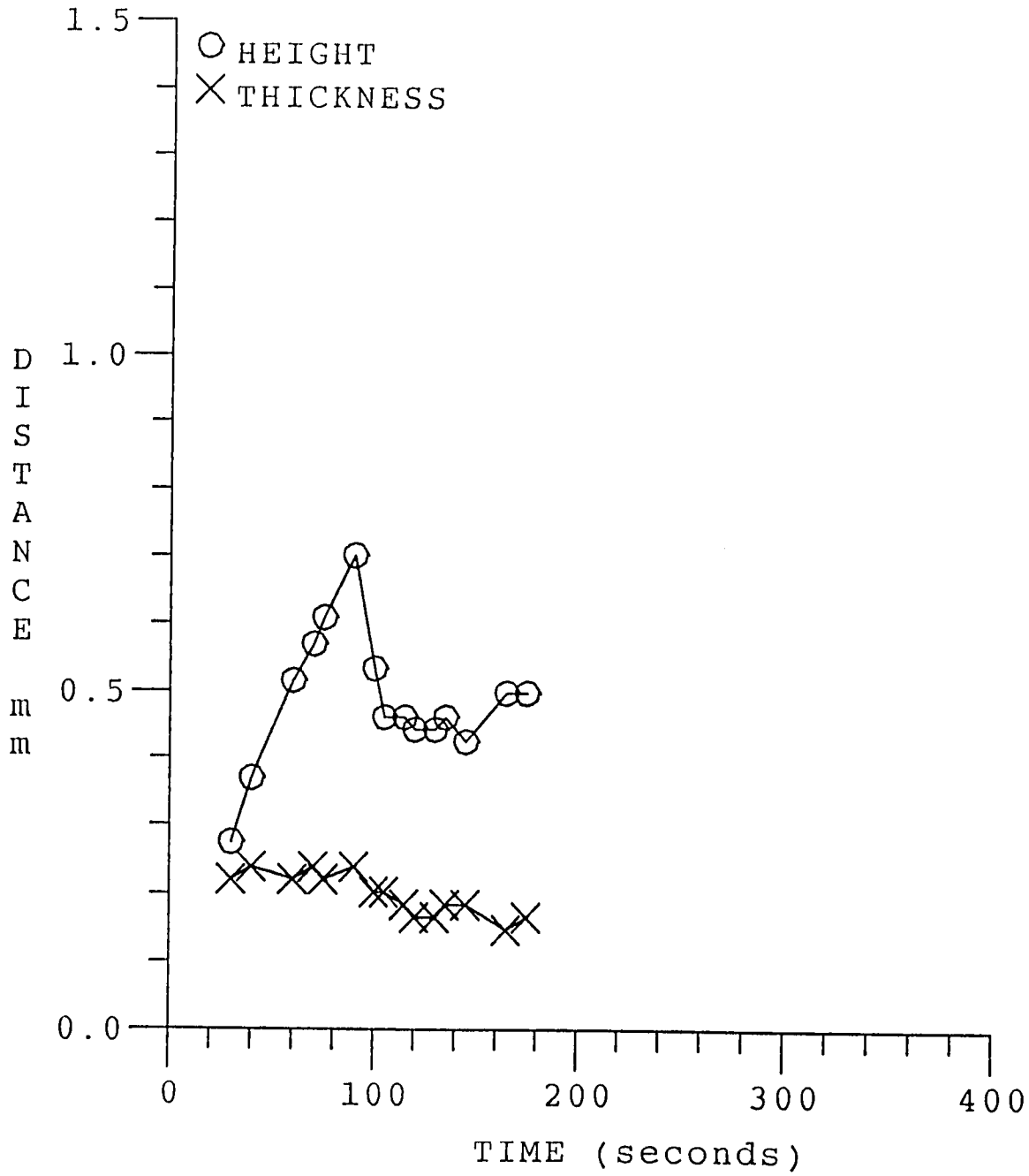


Figure VI-14. Null height (h_n) and thickness (t_n) as a function of time for 3.0°C/min cooling rate and 28°C/cm temperature gradient.

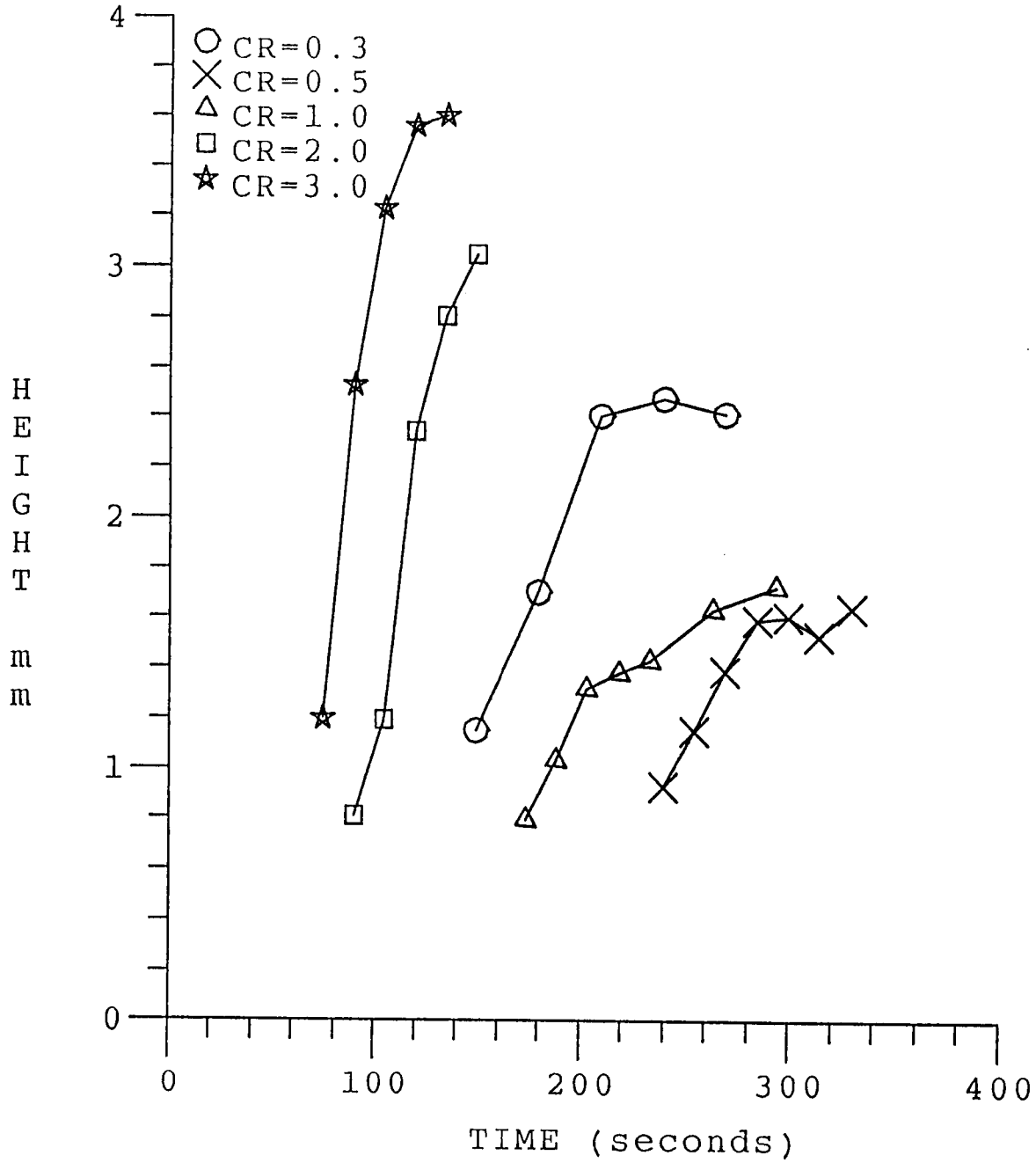


Figure VI-15. Vortex top height (h_t) as a function of time for 15°C/cm temperature gradient and five cooling rates (CR in °C/min).

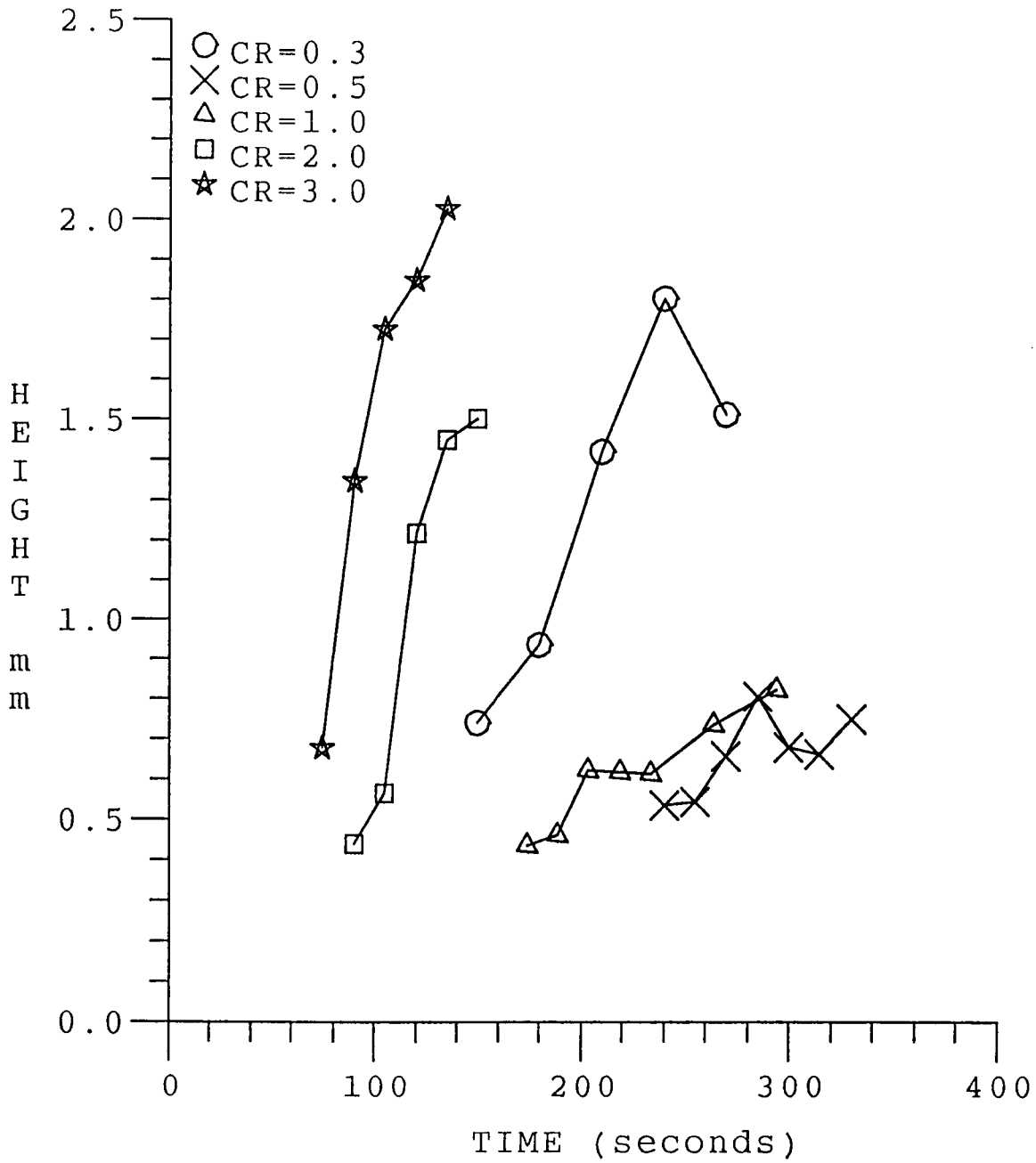


Figure VI-16. Vortex center height (h_c) as a function of time for 15°C/cm temperature gradient and five cooling rates (CR in °C/min).

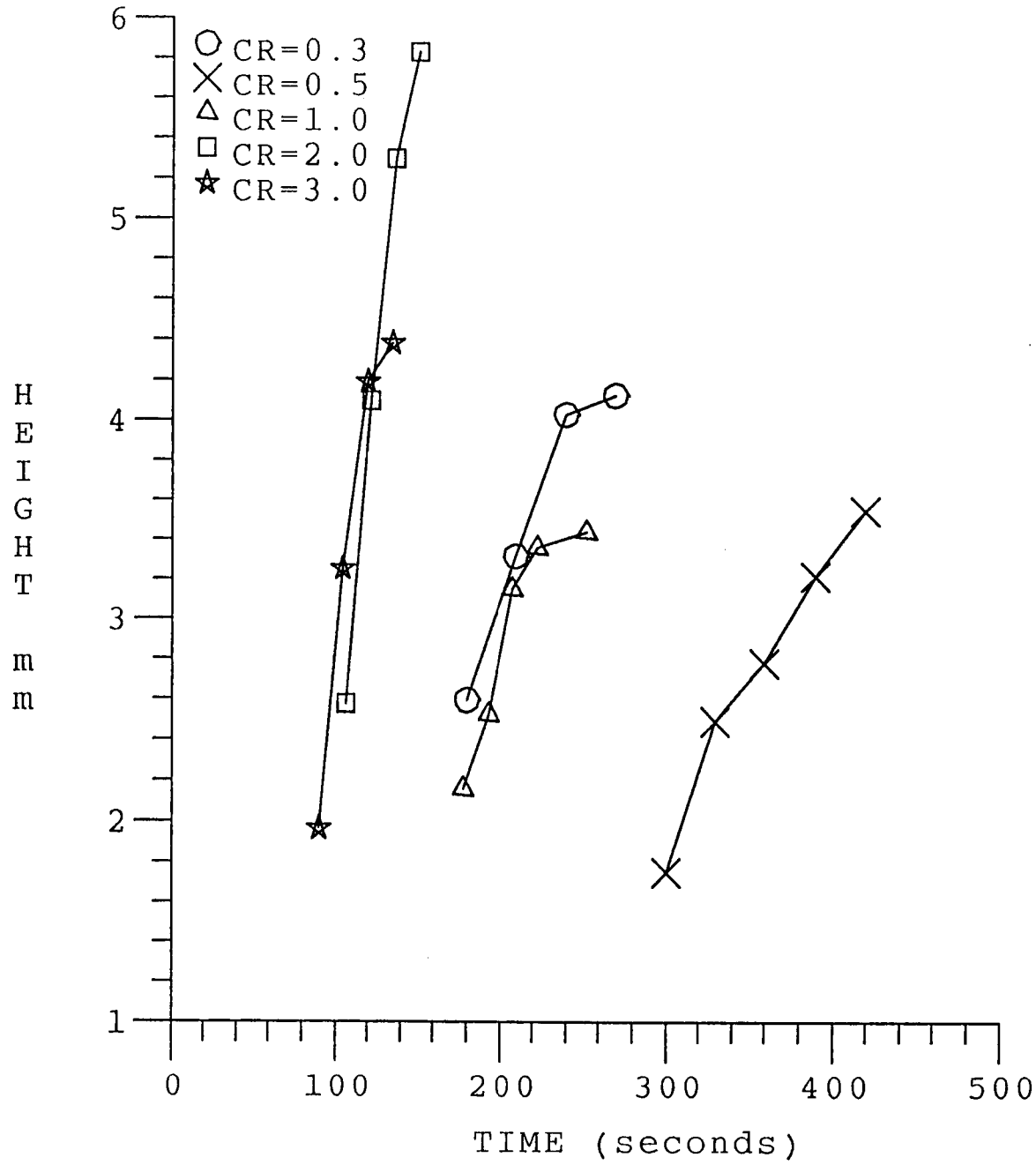


Figure VI-17. Vortex top height (h_t) as a function of time for 28°C/cm temperature gradient and five cooling rates (CR in °C/min).

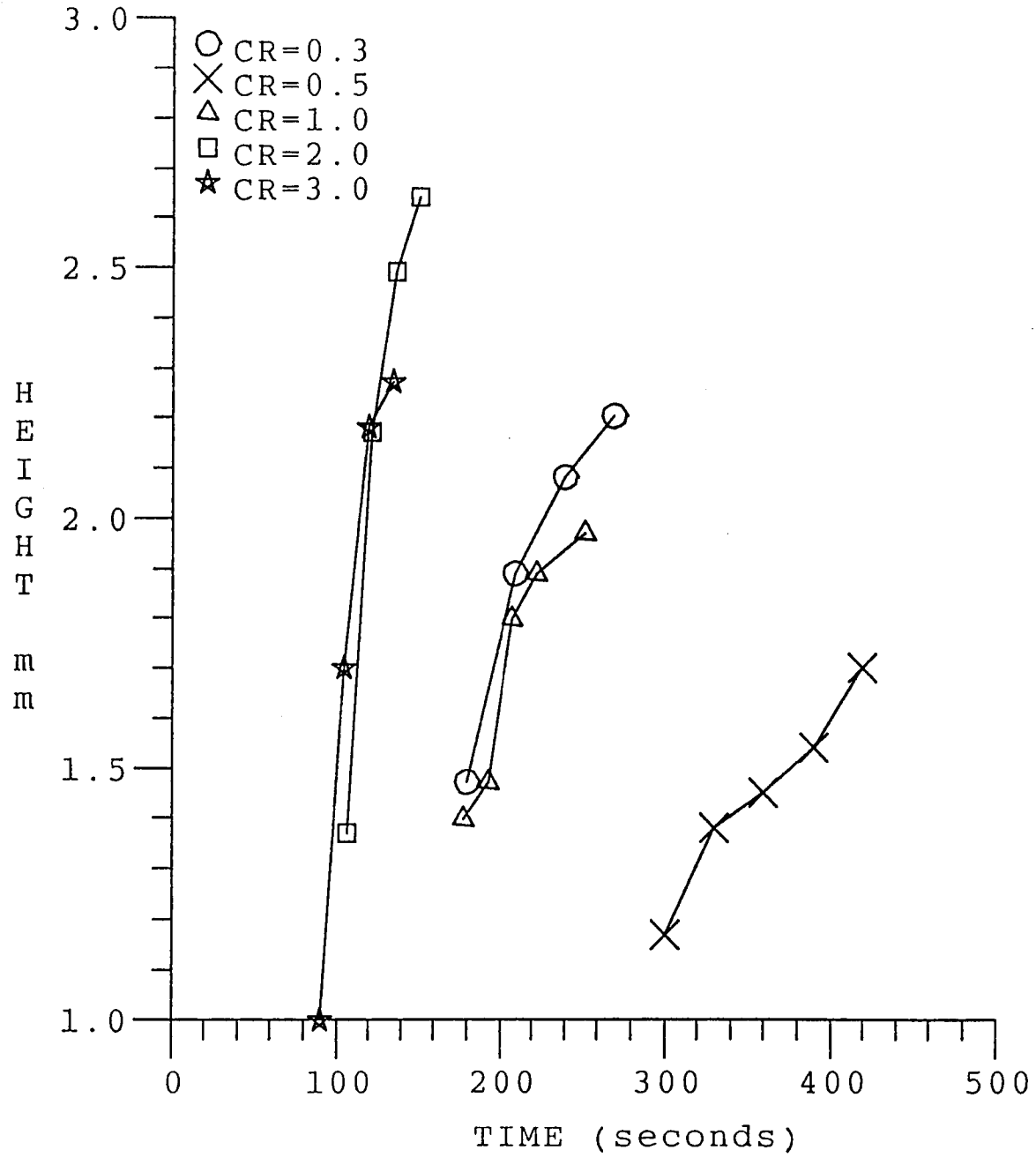


Figure VI-18. Vortex center height (h_c) as a function of time for 28°C/cm temperature gradient and five cooling rates (CR in °C/min).

sooner the higher the cooling rate and corresponded with the null layer data. An exception to this pattern is the cooling rate of 0.3°C/min for both the 15°C/cm and 28°C/cm temperature gradients, which broke down at approximately the same time as the 1.0°C/min cooling rate cases.

In plots of vortex height versus time (Figures VI-15 to VI-18), the vortex rise rates were found to increase with cooling rate (i.e. higher cooling rate higher rise rate). An exception to this was the cooling rate of 0.3°C/min.

The layer breakdown occurred earlier for the higher cooling rates due to the increased solute production associated with the accompanying higher growth rates. The early breakdown in the 0.3°C/min cooling rate case was found to coincide with an increase in critical wavelength (Table VI-1). Literature [14] suggests that the critical Rayleigh number should decrease with increasing critical wavelength, the wavelength being dependent on both temperature gradient and cooling rate.

The plots of vortex top and center height versus time (Figures VI-15 to VI-18) show the dependence of the breakdown time and rise rate on cooling rate. In these plots the vortex rise rates are shown to increase with cooling rate except for the coolings rate of 0.3°C/min for both gradients (15°C/cm and 28°C/cm). The vortex rise rate should increase with cooling rate due to increased solute rejection. The abnormally high rise rate for the 0.3°C/min cooling rates is consistent with the measured critical wavelengths for that rate. The longer wavelength vortices are more efficient at using the potential energy stored in the inverted layer. For instance, if there are two vertical jets associated with one wavelength and four associated with another it would be reasonable to assume that the two jets would rise faster and farther than the four.

Table VI-1. Wavelength of vortices for five cooling rates and two gradients.

CR (°C/min)	G=15 °C/cm λ_w (mm)	G=28 °C/cm λ_w (mm)
0.3	1.852	1.481
0.5	1.153	1.172
1.0	1.289	1.047
2.0	1.266	1.317
3.0	1.395	1.042

This is the case for the cooling rate of 0.3°C/min; the wavelength is longer (fewer jets) which leads to a higher rise rate.

The cooling rate of 2.0°C/min at the 28°C/cm temperature gradient was observed to have a breakdown time and rise rate that was very close to those at the 3.0°C/min cooling rate (closer than expected from the pattern of the other cooling rates). This cooling rate was found to have a higher wavelength than either the 3.0°C/min or 1.0°C/min cooling rates (Table VI-1). The longer wavelength caused the breakdown times to be sooner than expected, as in the 0.3°C/min cooling rate. The cause of the different wavelength is thought to be due to two factors. The first is simply experimental variation which one might expect for such a stability phenomena. The second is due to the shape of the stability curve. The stability curve for the NH_4Cl - H_2O system has not been determined but the curves for other systems indicate that the radius of curvature at the knee of the stability curve is large, which means that the range of critical wave numbers is large [4]. Other experiment runs at the same conditions showed wavelengths that were consistent with the other cooling rates indicating that the longer wavelength for the 2.0°C/min cooling rate at the 28°C/cm temperature gradient was truly an anomalous case. Unfortunately, detailed data for those runs were not available due to failures in data reduction equipment.

The aspect ratio (l_v/w_v) of the vortices should behave similar to the vortex height since the aspect ratio is driven by the vortex vertical dimension. This is born out by Figures VI-19 to VI-20. The differences that do exist are due to the changes of wavelength already discussed and small variations of the vortex width.

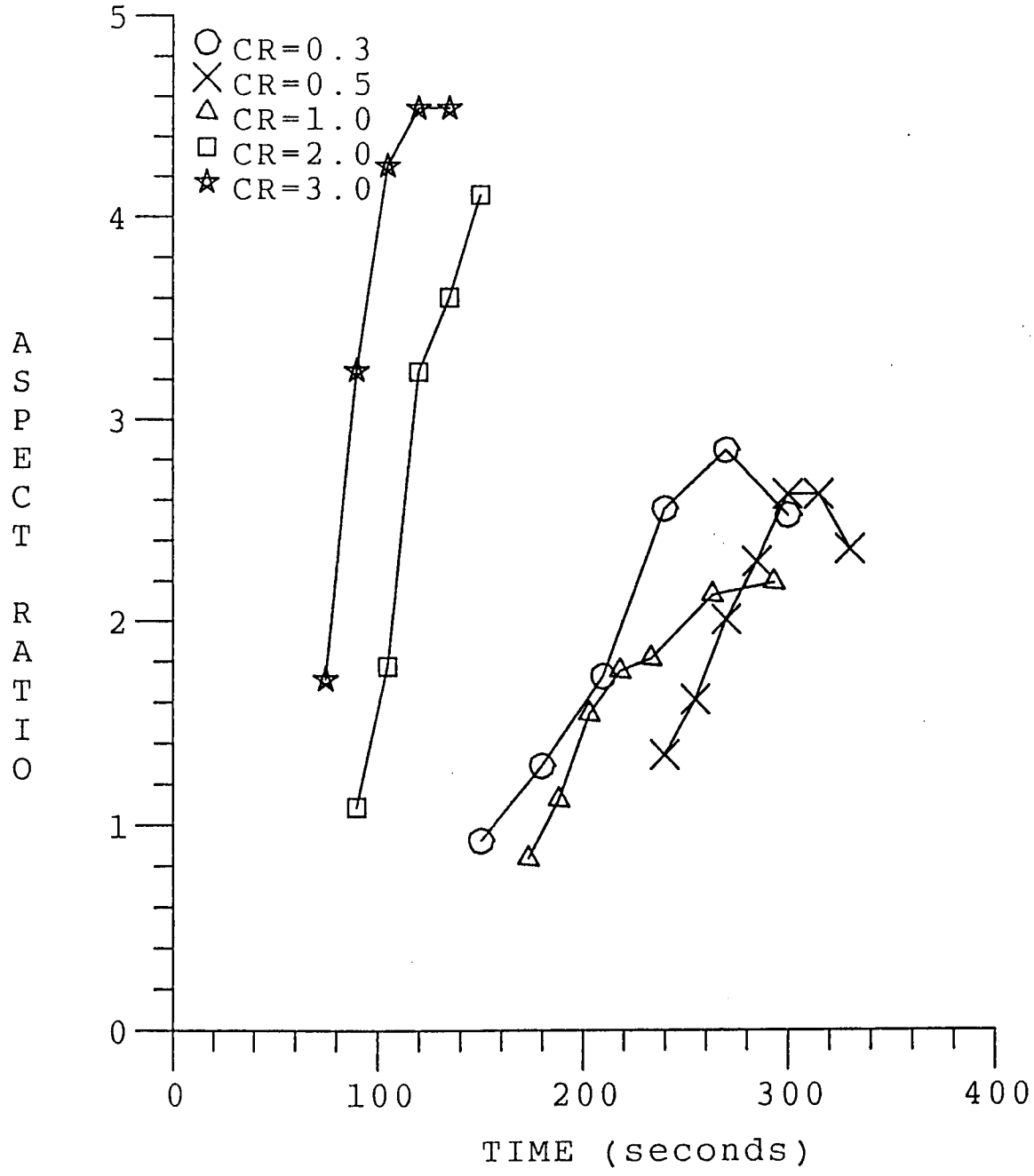


Figure VI-19. Aspect ratio (l_v/w_v) of vortices versus time for five cooling rates at 15°C/cm temperature gradient (CR in °C/min).

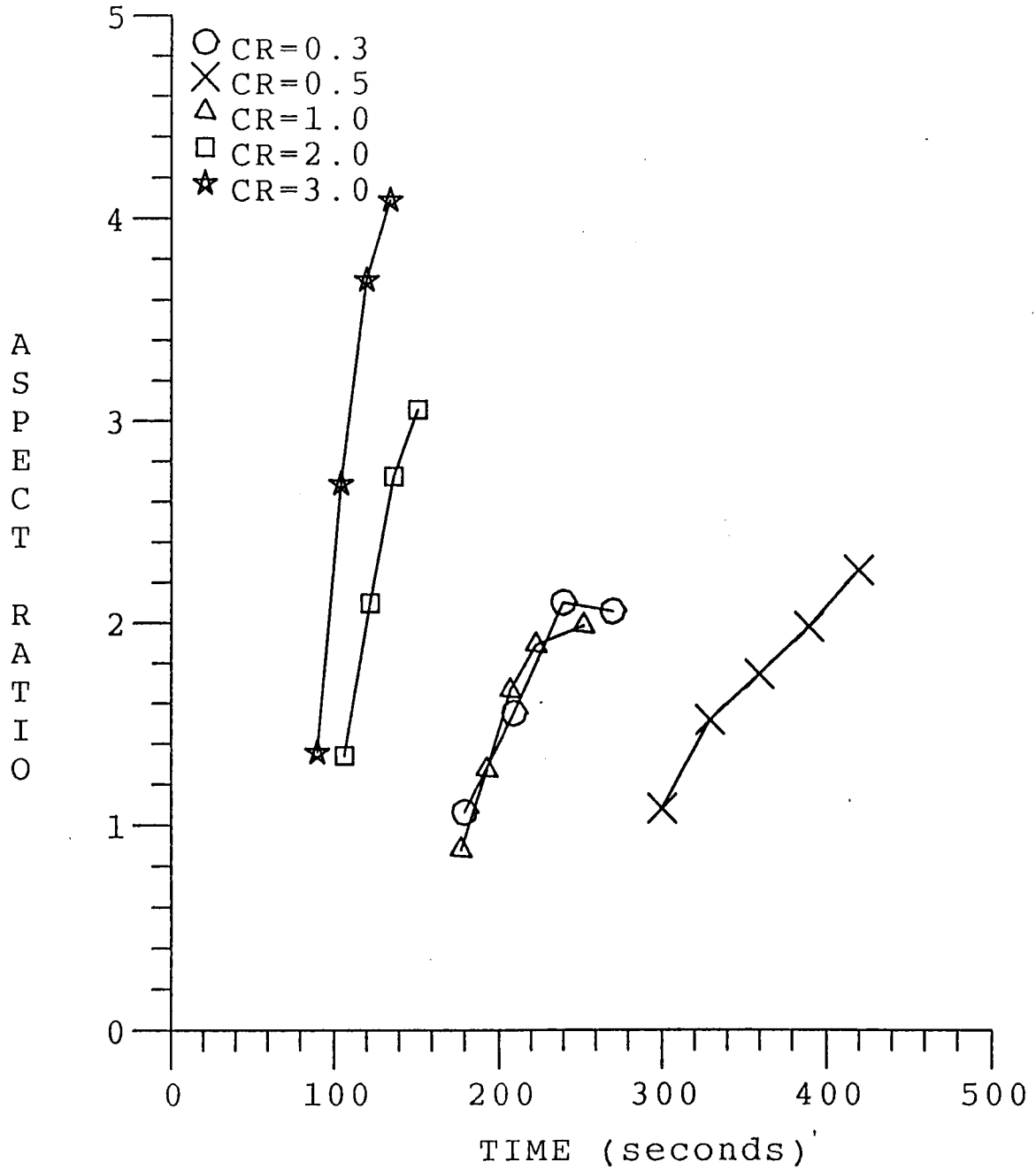


Figure VI-20. Aspect ratio (l_v/w_v) of vortices versus time for five cooling rates at 28°C/cm temperature gradient (CR in °C/min).

Temperature Gradient Effects

The temperature gradient effects concern the differences in breakdown time and rise rate for the two different gradients examined. Plots of vortex height versus time (Figures VI-15 to VI-18), show that the breakdown times for the 15°C/cm gradients were less than for the 28°C/cm gradients. It was also observed that the rise rates for both gradients were approximately the same.

The reason for the later breakdown in the 28°C/cm gradient is the increased stabilizing effect of the higher temperature gradient. Since solutal and thermal Rayleigh numbers are opposite in sign, the critical Rayleigh number is reached earlier in a similar run at the lower 15°C/cm gradient, i.e. it takes longer to reach the same degree of density inversion when the higher gradient is present.

Null Layer Behavior

The null layer appears as a dark horizontal band in the photographs from the confocal optical system. It represents the region of maximum index of refraction which can be shown to be the region of maximum density. The fluid above the null layer is less dense than the null layer due to the positive temperature gradient and the fluid below the null layer is less dense than the null layer due to the solute gradient. The null layer was observed to achieve maximum height at breakdown and then drop steadily until it reached a constant height some time after breakdown (Figures VI-5 to VI-14). The thickness of the layer was observed to stay nearly constant or increase slightly until breakdown, after which it decreased, approaching a constant some time after breakdown (Figures VI-5 to VI-14). The rise rate of the vortices was observed to decrease when the null layer height fell to its constant value and a change in vortex rise rate was observed whenever the null layer sink rate changed (Figure VI-21).

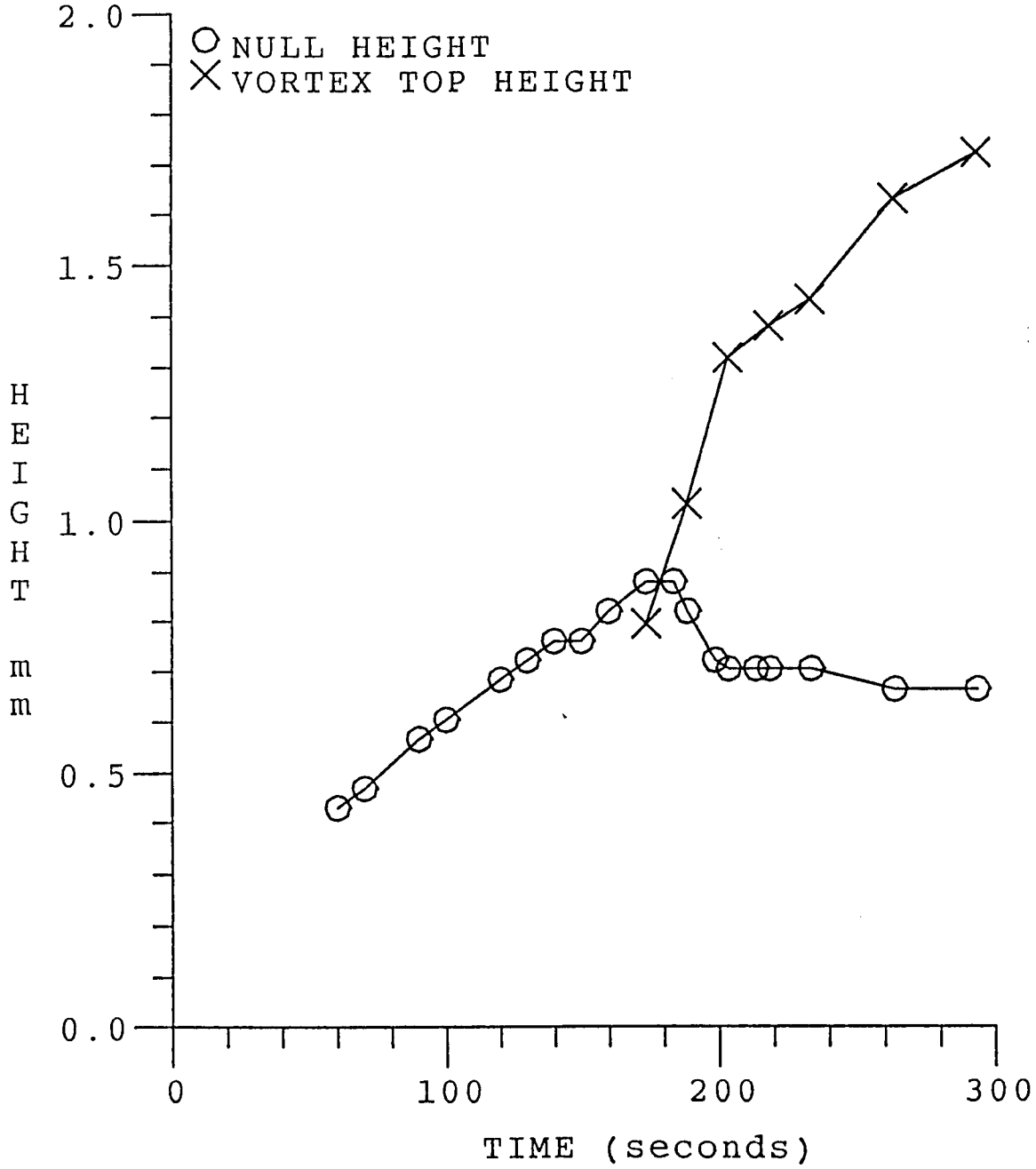


Figure VI-21. Comparison of null height and vortex top height versus time for 1.0°C/min cooling rate and 15°C/cm temperature gradient.

The height (location) of the null layer initially increased due to solute build-up in the mushy zone. When the inverted layer became unstable, the low density fluid rose into the bulk region; the high density null fell since the inverted layer was thined by escaping fluid. Eventually, when enough fluid escaped from beneath the null layer, an equilibrium where the rate of solute production is balanced by the rate of solute escaping into the bulk region was reached. The null layer height then remained constant. The rise rate of the vortices began to decrease when the null layer sank to its constant height. The potential energy stored in the layer was kinetically dissipated during this high rise rate stage of the run. When the potential energy was completely dissipated, the null layer reached its equilibrium height and the resulting lower rise rate became totally dependent on the solute being rejected by the growing interface.

The thickness of the null layer was observed to decrease to a constant value some time after breakdown. The density profile before layer breakdown is shown in Figure VI-22. The null thickness is dictated by the slopes of the approaching density gradients. The null is the region of highest index of refraction where the density is also a maximum. If the density gradients associated with temperature above the null and solute below the null increase then the nose of the density curve becomes sharper and the null layer thinner. The null layer moves down at breakdown but it is distorted by the resulting convective motion. It moves down as explained above and is thinned due to fluid motion which changes the concentration slopes. Figure VI-22 gives a possible density profile after convection begins, which is based on fringe spacing in the null region. A detailed flow model would be required to obtain a more accurate density profile.

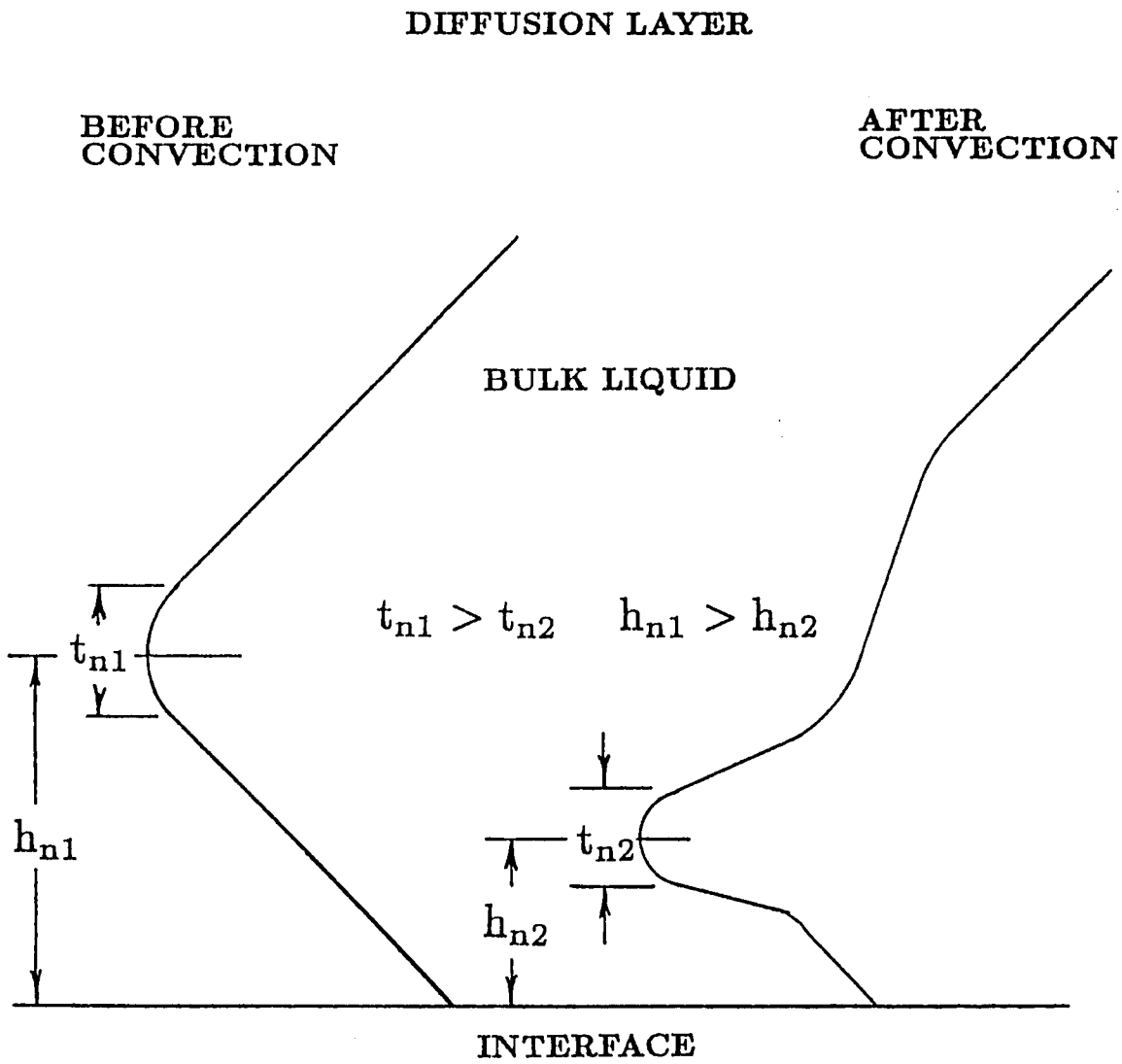


Figure VI-22. Schematic of density profile before and after breakdown in the diffusion layer.

Vortex Geometry and Relation to the Null Layer

From the front views of the particle tracker photographs, the observed vortical motion was judged to be either of the horizontal roll type or of the Benard cell type. To determine which type of convection was present, the cuvette was rotated 90 degrees. After each time exposure of the particle tracker, the cuvette was moved perpendicular to the sheet beam by using an X-Y translator. This made it possible to view different locations along the cells. If the convection is in the form of horizontal rolls the particle tracker photographs would not change with position. If the convection is in the form of Benard cells some of the photographs would look the same as in the front view (i.e. the ones where the sheet beam passes through the center of a row of cells). With the cuvette rotated 90 degrees, the particles behaved the same as they did in the front view, with approximately the same wavelength, indicating that the convection was a 3-D Benard cell with fluid rising in the center and falling around the periphery of the cell (Figures VI-23 to VI-24).

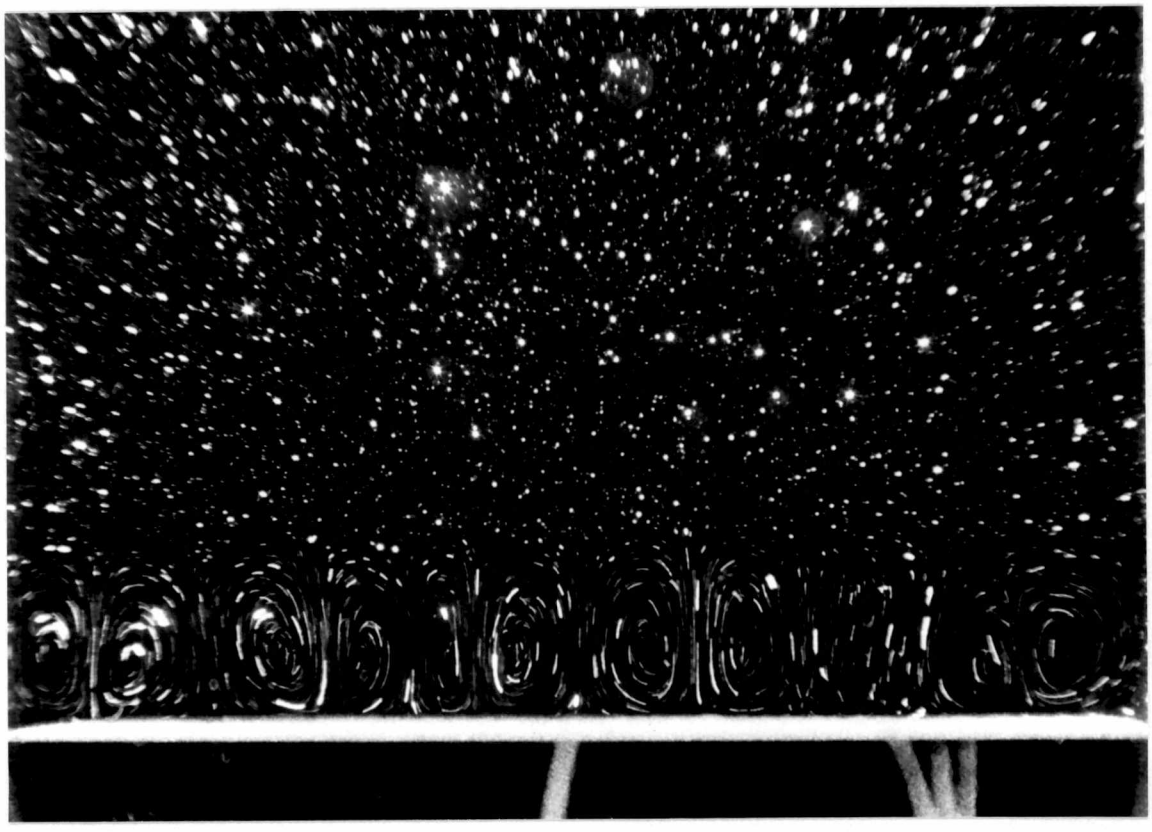


Figure VI-23. Front view of convection at 1.0°C/min and 15°C/cm temperature gradient.

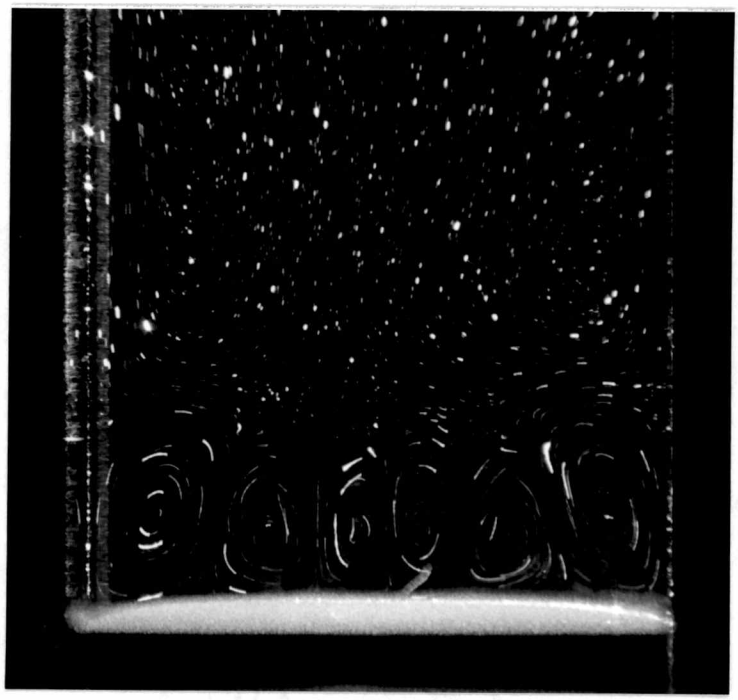


Figure VI-24. Side view of convection illustrating three dimensional structure at 1.0°C/min cooling rate and 15°C/cm temperature gradient.

VII. SUMMARY AND CONCLUSIONS

The most fundamental observation concerning breakdown of the inverted layer is that the low density fluid participates in vortical motion rather than salt fingering as double-diffusive arguments would suggest. The particle tracker data (Figures VI-3 to VI-4) clearly show that the fluid does not continue to rise but participates in a vortical flow pattern. This would suggest that the material does not thermally equilibrate as it rises into the hotter fluid regions. This is consistent for a high Prandtl number fluid such as ammonium chloride and water.

It was observed that the inverted layer broke down due to the static instability caused by the density inversion relative to the null layer. It was also observed (Figures VI-23 to VI-24) that the resulting convection was in the form of Benard cells. This indicated that the instability was of the Rayleigh-Benard type which can be characterized by a combined critical Rayleigh number. The vortex rise rates for the 28°C/cm gradient were approximately the same as those of the 15°C/cm gradient (Figures VI-15 to VI-18). This indicates that the thermal conductivity is too small to have a significant effect on the buoyancy of the solute rich fluid. If the thermal conductivity was more significant it would be expected that the rise rates would be higher in the higher temperature gradient since the resulting increased heat transfer rate would enhance the buoyancy effect.

Measurement of the critical height at which the null layer becomes unstable allows calculation of a combined critical Rayleigh number which is a function of the initial mushy-zone height (the initial mushy-zone height being the height of the interface before cooling was initiated). The dependence of the critical Rayleigh number on the initial mushy-zone height can be seen in Figure VII-1 from McCay et al [12]. This critical Rayleigh number should be applicable for

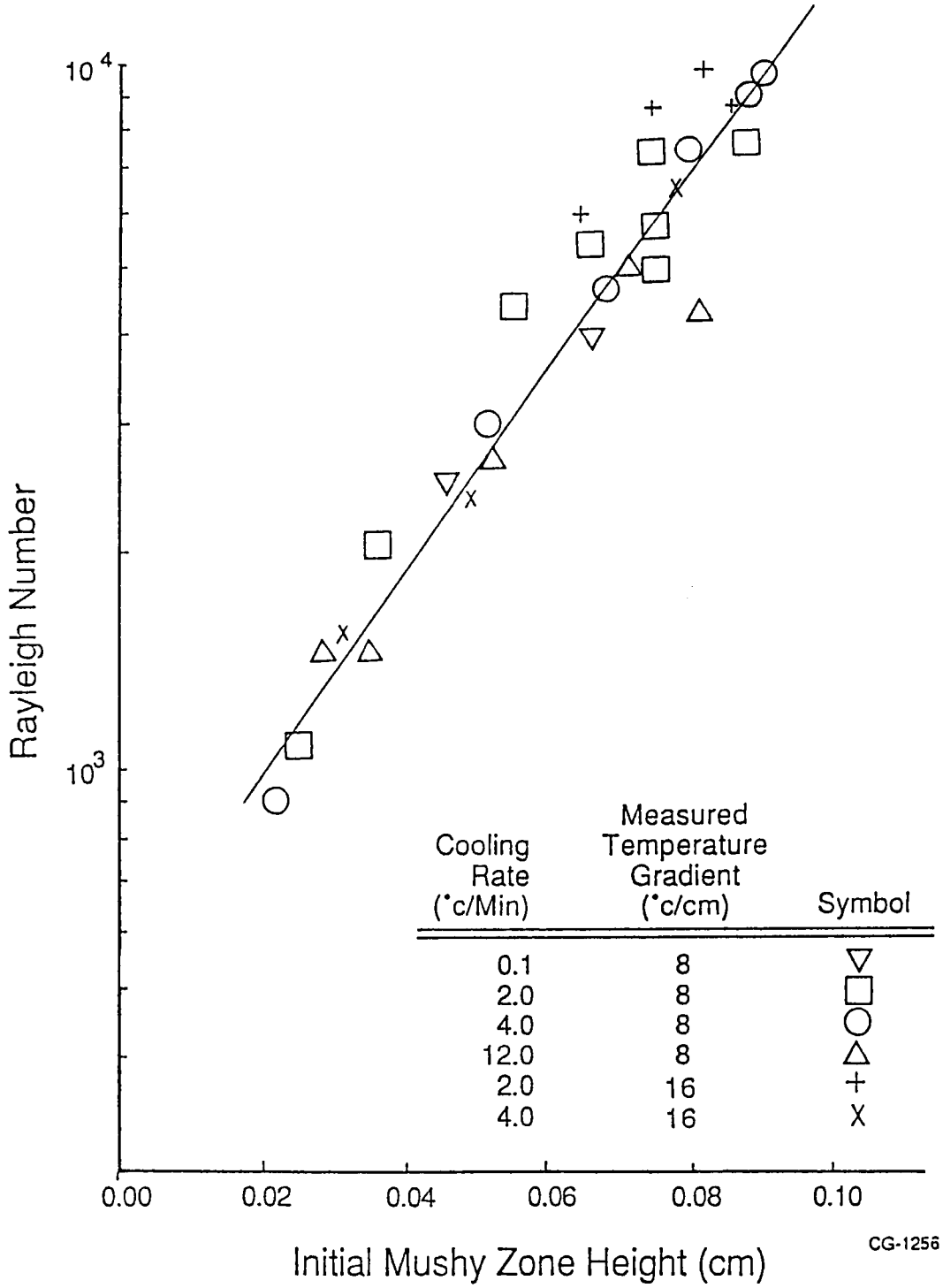


Figure VII-1. Critical Rayleigh number variation with initial mushy zone height (from reference 12).

predicting breakdown in actual metal systems. This would provide a guideline for suppressing convection in these systems by controlling the cooling rate and temperature gradient. The lack of double diffusive effects within the metal model system may limit the absolute extrapolation to metallic systems with regard to convective patterns but it is possible that breakdown phenomena will hold. The critical Rayleigh number determined in this study does compare favorably with the theoretically determined value determined by Coriell [14].

BIBLIOGRAPHY

BIBLIOGRAPHY

[1] S.M. Copley and A.F. Giamei, "The Origin of Freckles in Unidirectionally Solidified Castings," *Metallurgical Transactions*, Vol. 1, pp. 2193–2204, 1970.

[2] A.K. Sample and A. Hellawell, "The Mechanisms of Formation and Prevention of Channel Segregation during Alloy Solidification," *Metallurgical Transactions*, Vol. 15A, pp. 2163–2173, 1984.

[3] M.H. Johnston and R.B. Owen, "Optical Observations of Unidirectional Solidification in Microgravity," *Metallurgical Transactions*, Vol. 14A, pp. 2163–2167, 1983.

[4] M.E. Glicksman, S.R. Coriell, and G.B. McFadden, "Interaction of Flows with the Crystal - Melt Interface," *Annual Review Fluid Mechanics*, Vol. 18, pp. 307–335, 1986.

[5] M.C. Flemings, *Solidification Processing* (McGraw-Hill, San Franciso 1974).

[6] K.A. Jackson and J.D. Hunt, "Transparent Compounds that Freeze Like Metals," *Acta Metallurgica*, Vol. 3, pp. 1212–1215, 1965.

[7] F.N. Rhines, *Phase Diagrams in Metallurgy* (McGraw-Hill, New York, 1956).

[8] M.H. Johnston, R.B. Owen, and R. E. Shurney, "Optical Observations of Unidirectional Solidification in Microgravity," *NASA Technical Paper 2110*, Vol. 14A, pp. 2163–2167, 1983.

[9] B.D. Cullity, *Elements of X-Ray Diffraction*, 2nd ed. (Addison-Wesley, Reading, Massachusetts, 1978).

[10] E. Hecht and A. Zajac, *Optics* (Addison-Wesley, Reading, Massachusetts, 1979).

[11] J. Zierep and H. Oertel Jr., eds., *Convective Transport and Instability Phenomena* (G. Braum, Karlsruhe, 1982).

[12] T.D. McCay, M.H. McCay, S.A Lowry, and L.M. Smith, "Convective Instabilities during Directional Solidification," to be published in *Journal of Thermophysics and Heat Transfer*, April 1989.

[13] P.F. Linden, "Diffusive Instabilities and Porous Media," in Ref [11], pp. 171–199.

[14] F. Chen and C.F. Chen, "Onset of Convection in a Horizontal Porous Layer Underlying a Fluid Layer," *Journal of Heat Transfer*, Vol. 110, pp. 403–409, 1988.

[15] G.B McFadden, R.G. Rehm, S.R. Coriell, W. Chuck, and K.A. Morrish, "Thermosolutal Convection during Directional Solidification," *Metallurgical Transactions*, Vol. 15A, pp. 2125–2137, 1984.

VITA

Perry A. Gray was born in Herndon, Virginia, on April 17, 1962. In 1971 he moved to Mount Dora, Florida. He attended high school at Florida Central Academy from 1974 to 1980 in Mount Plymouth and graduated in 1980. He attended Lake-Sumter Community College from 1980 to 1983 after which he attended the University of Florida and received a Bachelor of Science degree in Aerospace Engineering in 1986. After graduating from the University of Florida, he attended the University of Tennessee Space Institute (UTSI) on a graduate research assistantship where he majored in Engineering Science and Mechanics. He received the Master of Science degree from UTSI in May 1989.